

HIDDEN DARK SECTORS:
JET SUBSTRUCTURE AND EFFECTIVE FIELD THEORIES

by

JOEL SORCHEVICH DOSS

A DISSERTATION

Presented to the Department of Physics
and the Division of Graduate Studies of the University of Oregon
in partial fulfillment of the requirements
for the degree of
Doctor of Philosophy

June 2022

DISSERTATION APPROVAL PAGE

Student: Joel Sorchevich Doss

Title: Hidden Dark Sectors – Jet Substructure and Effective Field Theories

This dissertation has been accepted and approved in partial fulfillment of the requirements for the Doctor of Philosophy degree in the Department of Physics by:

Graham Kribs	Chair
Timothy Cohen	Advisor
David Strom	Core Member
Nicolas Addington	Institutional Representative

and

Krista Chronister	Vice Provost of Graduate Studies
-------------------	----------------------------------

Original approval signatures are on file with the University of Oregon Division of Graduate Studies.

Degree awarded June 2022

© 2022 Joel Sorchevich Doss
This work is licensed under a Creative Commons
[Attribution-NonCommercial-NoDerivatives 4.0 International License](https://creativecommons.org/licenses/by-nc-nd/4.0/).



DISSERTATION ABSTRACT

Joel Sorcevich Doss

Doctor of Philosophy

Department of Physics

June 2022

Title: Hidden Dark Sectors – Jet Substructure and Effective Field Theories

The search for physics beyond the Standard Model is a daunting task. As parameter spaces for compelling models shrink, there is motivation for more radical concepts. However, there is a need for understanding the structure of novel signal regions. We describe two analyses on extensions to the Standard Model wherein the dynamics of new particles are isolated.

We first examine collider predictions for a dark sector with QCD-like properties. Pair production of dark quarks can result in a wide variety of signatures. A challenging signal results when production induces a parton shower with a high multiplicity of collimated dark hadrons, which subsequently decays to Standard Model hadrons. The final states contain jets whose substructure encodes their non-QCD origin. This is a subtle signature of strongly coupled beyond the Standard Model dynamics whose analyses must incorporate systematic errors from model approximations. We estimate theoretical uncertainties for a substructure observable designed to be sensitive to the gauge structure of the underlying object, the two-point energy correlator $e_2^{(\beta)}$. We explore the separability against the QCD background as model parameters are varied. Estimates are provided that quantify one's ability to distinguish these dark sector jets from the overwhelming QCD background.

Next, we look at Effective Field Theory (EFT) extensions of the Standard Model. EFTs are systematically improvable expansions suppressed by a new physics scale M . For EFT predictions in parameter spaces where $M < \sqrt{\hat{s}}$, concerns of self-consistency emerge, which can manifest as a violation of perturbative partial-wave unitarity. However, when searching for EFT effects at a hadron collider with center-of-mass energy \sqrt{s} using an inclusive strategy, we typically do not have access to the event-by-event value of $\sqrt{\hat{s}}$. This motivates the need for a formalism that incorporates parton distribution functions into the perturbative partial-wave unitarity analysis. Our approach opens up a potentially valid region of the EFT parameter space where $M \ll \sqrt{s}$. The perturbative unitarity bounds are sensitive to the details of a given search, an effect we investigate by varying kinematic cuts.

This dissertation consists of previously published co-authored material.

CURRICULUM VITAE

NAME OF AUTHOR: Joel Sorchevich Doss

GRADUATE AND UNDERGRADUATE SCHOOLS ATTENDED:

University of Oregon, Eugene, Oregon, USA
The University of Texas at Austin, Austin, Texas, USA

DEGREES AWARDED:

Doctor of Philosophy in Physics, 2022, University of Oregon
Bachelor of Science in Physics, 2016, The University of Texas at Austin
Bachelor of Science in Astronomy, 2016, The University of Texas at Austin

AREAS OF SPECIAL INTEREST:

Beyond Standard Model Physics, Effective Field Theories, Dark Matter,
Collider Physics, Strongly Coupled Dynamics

PROFESSIONAL EXPERIENCE:

Graduate Research Assistant, University of Oregon, 2017-2022
Graduate Teaching Assistant, University of Oregon, 2017-2022
Undergraduate Researcher, The University of Texas at Austin, 2014-2016
Physics Tutor, Sanger Learning Center, 2014-2016

GRANTS, AWARDS AND HONORS:

First Year Graduate Fellowship, University of Oregon, 2016
Physics Honors Thesis, The University of Texas at Austin, 2016
Dean's Honored Graduates, The University of Texas at Austin, 2016
Endowed Presidential Scholarship, The University of Texas at Austin, 2015
Dean's Scholars Program, The University of Texas at Austin, 2012-2016

PUBLICATIONS:

- T. Cohen, J. Doss, and X. Lu, “Unitarity Bounds on Effective Field Theories at the LHC,” *JHEP* 04 (2022) 155, [arXiv:2111.09895 \[hep-ph\]](#).
- T. Cohen, J. Doss, and M. Freytsis, “Jet Substructure from Dark Sector Showers,” *JHEP* 09 (2020) 118, [arXiv:2004.00631 \[hep-ph\]](#).
- J. Feng, M. Baumann, B. Hall, J. Doss, L. Spencer, and R. Matzner, “PoMiN: A Post-Minkowskian N-Body Solver,” *Astrophys. J.* 859 (2018) no. 2, 130, [arXiv:1805.00813 \[gr-qc\]](#).

ACKNOWLEDGEMENTS

I first want to thank my parents, Christopher Doss and Deborah Sorchevich, for their endless support and boundless love. To my mother, I am eternally grateful for understanding me, my philosophical perspectives on life, and my sense of worth. To my father, I am forever indebted to you for demonstrating what unconditional love truly means.

Thank you to my advisor, Tim Cohen, for your immeasurable guidance and encouragement. Thank you for helping me understand what it means to be a physicist, both academically and personally.

Thank you to the Institute for Fundamental Science for supporting me throughout my graduate career, especially the High Energy Theory Group. To the faculty, Spencer Chang, Tim Cohen, Paul Csonka, Nilendra Deshpande, Graham Kribs, Dave Soper, and Tien-Tien Yu, thank you for providing a deeply enriching academic environment. To the past and present postdoctoral researchers, Gilly Elor, Marat Freytsis, Xiaochuan Lu, Bryan Ostdiek, and Anna-Maria Taki, thank you for your wealth of knowledge and time. To the past graduate students, Gabriel Barello and Tom Tong, thank you for welcoming me into your cohort. To the current graduate students, Layne Bradshaw, Tom Bouley, Haidar Esseili, Thomas Schwemberger, and Aria Radick, thank you for the countless hours of joy.

Thank you to Anne McGinley for being the most helpful person in the department. Thank you to Stephanie Majewski for your bottomless kindness and superhuman ability to assist every graduate student. Thank you to Laura Jeanty and David Strom for humbling me to the complexities of high energy experimentalism.

Thank you to my fellow University of Oregon physics graduate students, especially Matthew Brown, Trevor Brunnenmeyer, Uriel Hernandez, Rachael Klaiss, Wenqian Sun, and Ethan Turner, for your friendship, camaraderie, and dedication to cultivating a better department. Thank you to all of the wonderful graduate students in other departments for your tireless labor, especially my Union friends, Ricardo Friaz, Ellen Kress, Kiana Na, Ellen Olsen, Samantha Shepherd, and Emily Sutton. Universities work because we do.

Thank you to Can Kilic and Greg Sitz at The University of Texas at Austin for emboldening me to succeed beyond my own expectations.

Thank you to all my friends and family who have supported me in life, Layne Bradshaw, Allison Brawley, Trevor Brunnenmeyer, Emma Chittick, Andy Dao, Johan Bonilla, Ricardo Friaz, Hollis Gehrett, Robin Goins, Taylor Hoyt, River Hudgins, Alejandro Ortiz, Aria Radick, Crystal Riley, Samantha Shepherd, Sierra Vernon, Alexis Vesey, Katrina Vesey, Mark Vesey, and Amy Woodhull. I could not have done this without you.

Thank you to Alexandria Costantino for her friendship as we navigated the postgraduate process.

Thank you to my closest friends, Evan Ott, Melody Valadez Ott, Miquela Stein, and Robert Wilson, for always believing in me, even when I did not.

Finally, thank you to my dearest friend, Victoria Levy. Thank you for showing me what true friendship means. I love you eternally. Thank you for being with me as I found myself. I am here because of you.

For my grandfather, Jordan Lazar Sorchev, who always encouraged me to ask why.

And for any child who has ever looked up at the stars and questioned everything about the Universe, especially their own identity. You are never alone.

This dissertation is the product of unionized labor as part of the Graduate Teaching Fellows Federation, AFT Local 3544.

TABLE OF CONTENTS

Chapter	Page
I. INTRODUCTION	1
1.1. Jet Substructure in Dark Sectors	2
1.2. Unitarity Bounds on Effective Field Theories	6
II. JET SUBSTRUCTURE IN DARK SECTORS	9
2.1. Substructure Observables with Error Envelopes	10
2.1.1. Analytics Using Traditional Resummation Techniques	12
2.1.2. Numerics From PYTHIA	15
2.1.3. Error Envelopes	18
2.1.4. Applying the Predictions	22
2.2. Distinguishing Dark Substructure from QCD	23
2.2.1. $\tilde{\Lambda}$ Dependence	24
2.2.2. \tilde{N}_C Dependence	26
2.2.3. \tilde{n}_F Dependence	29
2.2.4. \tilde{m}_q Dependence	32
2.3. Quantifying Hadronization Uncertainties	34
2.4. Discovering Dark Substructure	36
III. UNITARITY BOUNDS ON EFFECTIVE FIELD THEORIES	41
3.1. Strategies for Assessing EFT Validity	41
3.2. Benchmark Process and Toy Models	44

Chapter	Page
3.2.1. t -Channel Model	46
3.2.2. s -Channel Model	48
3.2.3. On the $1/M$ Versus $1/\Lambda$ EFT Expansions	50
3.3. Partial-Wave Unitarity Bounds	53
3.3.1. Partonic Initial State	54
3.3.2. Hadronic Initial State	58
3.3.3. Unitarity and EFT Truncation	61
3.4. Interpreting Unitarity Violation	67
3.4.1. Partonic Initial State Cross Sections	68
3.4.2. Evidence for EFT Validity	71
3.4.2.1. t -channel Results	72
3.4.2.2. s -channel Results	76
3.5. Impact of Kinematic Cuts	78
IV. CONCLUSIONS	82
4.1. Jet Substructure in Dark Sectors	82
4.2. Unitarity Bounds on Effective Field Theories	84
APPENDICES	
A. ANALYTIC DETAILS OF THE RESUMMATION CALCULATION	88
B. UNITARITY BOUNDS FOR SMALLER FINAL STATE MASS	98
REFERENCES CITED	100

LIST OF FIGURES

Figure		Page
1.	Illustration of the enveloping procedure utilized to estimate theory systematic errors as applied to QCD, for $p_T = 1$ TeV jets. The analytic and numerical predictions for the e_2 distributions are shown assuming various levels of approximation as detailed in the legend [left panel]. These predictions are used to create error sub-envelopes [middle panel] that are then combined to result in the final envelope [right panel]. The green sub-envelope captures the difference between the LL and MLL analytic predictions. The red sub-envelope captures the difference between the MLL analytic prediction and the parton level numerical result from PYTHIA. The blue sub-envelope captures the difference between the parton and hadron level prediction from PYTHIA. These envelopes are added in quadrature to compute the total envelope [right panel]. Note that when computing envelopes for the dark sector, we include three numerical predictions when the final states are dark partons, dark hadrons, or visible hadrons. The angular dependence parameter is set to $\beta = 2$ for illustration.	19
2.	Dependence on the angular dependence parameter β in QCD for $p_T = 1$ TeV jets. We show the predictions derived using the MLL analytic calculation, along with the parton and hadron level numerical results from PYTHIA. Larger (smaller) angular dependence emphasizes the contribution from pairs of partons with larger (smaller) angular distance. The analytic calculations begin to break down for angular dependence values $\beta < 0.5$, which is reflected here in the fact that the $\beta = 0.2$ curve does not appropriately terminate at the kinematic endpoint.	21
3.	The behavior of e_2 as the dark confinement scale $\tilde{\Lambda}$ is varied, for $p_T = 1$ TeV jets. See the legend for values of $\tilde{\Lambda}$; all other values are given in Table 1. We show the normalized e_2 distributions [top], where the central value of the envelope is marked with the black lines, while the shaded region denotes the envelope. The peak shifts to larger values of e_2 as $\tilde{\Lambda}$ is increased. The cumulant distributions Σ as a function of x_{cut} are also provided [bottom], where again the lines denote the central values and the shaded bands are the integrated envelopes, see Eq. (2.9). We show both results for two choices of the angular dependence: $\beta = 2$ [left] and $\beta = 0.5$ [right].	25

4. Discrimination of dark sector against QCD for various choices of the confinement scale $\tilde{\Lambda}$ for $p_T = 1$ TeV jets, using the MLL analytic calculation. Note that the impact of errors is ignored here, see Sec. 2.1.4 for details. We show ROC curves in the background rejection $1 - \epsilon_B$ versus signal efficiency ϵ_S plane [left]. We show the curve of discriminatory significance $\epsilon_S/\sqrt{\epsilon_B}$ against signal efficiency ϵ_S [middle]. Fixing the background rejection at 90%, we then show the relative change in discriminatory power as a function of $\tilde{\Lambda}$. The angular dependence parameter is $\beta = 2$ for all panels. 26

5. The behavior of e_2 as the dark sector gauge group $SU(\tilde{N}_C)$ is varied, for $p_T = 1$ TeV jets. See the legend for values of \tilde{N}_C ; all other values are given in Table 1. We show the normalized e_2 distributions [top], where the central value of the envelope is marked with the black lines, while the shaded region denotes the envelope. The peak moves to slightly lower values of e_2 as \tilde{N}_C is increased. The cumulant distributions Σ as a function of x_{cut} are also provided [bottom], where again the lines denote the central values and the shaded bands are the integrated envelopes, see Eq. (2.9). We show both results for two choices of the angular dependence: $\beta = 2$ [left] and $\beta = 0.5$ [right]. 27

6. Discrimination of dark sector against QCD for various choices of the number of colors in the dark sector \tilde{N}_C for $p_T = 1$ TeV jets, using the MLL analytic calculation. Note that the impact of errors is ignored here, see Sec. 2.1.4 for details. We show ROC curves in the background rejection $1 - \epsilon_B$ versus signal efficiency ϵ_S plane [left]. We show the curve of discriminatory significance $\epsilon_S/\sqrt{\epsilon_B}$ against signal efficiency ϵ_S [middle]. Fixing the background rejection at 90%, we then show the relative change in discriminatory power as a function of \tilde{N}_C . The angular dependence parameter is $\beta = 2$ for all panels. 28

7. The behavior of e_2 as the number of dark quark flavors \tilde{n}_F is varied, for $p_T = 1$ TeV jets. See the legend for values of \tilde{n}_F ; all other values are given in Table 1. We show the normalized e_2 distributions [top], where the central value of the envelope is marked with the black lines, while the shaded region denotes the envelope. The peak moves to higher values of e_2 as \tilde{N}_C is increased. The cumulant distributions Σ as a function of x_{cut} are also provided [bottom], where again the lines denote the central values and the shaded bands are the integrated envelopes, see Eq. (2.9). We show both results for two choices of the angular dependence: $\beta = 2$ [left] and $\beta = 0.5$ [right]. 30

8. Discrimination of dark sector against QCD for various choices of the number of dark quark flavors \tilde{n}_F for $p_T = 1$ TeV jets, using the MLL analytic calculation. Note that the impact of errors is ignored here, see Sec. 2.1.4 for details. We show ROC curves in the background rejection $1 - \epsilon_B$ versus signal efficiency ϵ_S plane [left]. We show the curve of discriminatory significance $\epsilon_S/\sqrt{\epsilon_B}$ against signal efficiency ϵ_S [middle]. Fixing the background rejection at 90%, we then show the relative change in discriminatory power as a function of \tilde{n}_F . The angular dependence parameter is $\beta = 2$ for all panels. 31
9. The behavior of e_2 for the dark sector as the degenerate dark quark mass \tilde{m}_q is varied, for $p_T = 1$ TeV jets. The value of \tilde{m}_q is varied according to the legend, while all other values are given in Table 1. The associated dark hadron masses are $2\tilde{m}_q$. Only a numerical study using PYTHIA is presented. We provide a cubic fit to these distributions to guide the eye. Larger dark quark masses move the peak to higher values due to the resulting cutoff imposed on collinear divergences for emissions from massive quarks. We show the results for two choices of the angular dependence: $\beta = 2$ [left] and $\beta = 0.5$ [right]. 33
10. Total theory uncertainties on the e_2 distributions for $p_T = 1$ TeV jets for a dark sector whose model parameters are set to the benchmark values given in Table 1 due to both perturbative and hadronization effects. Perturbative uncertainties are largest around the peak region, dominating at larger e_2 values. Hadronization uncertainties contribute most noticeably starting from the peak and extend down to smaller values of e_2 . Results are presented for two choices of the angular dependence: $\beta = 2$ [left] and $\beta = 0.5$ [right]. 35
11. The background reduction factor (see Eq. (2.15)) required to observe new physics over the QCD background for $p_T = 1$ TeV jets. We show the value required if there are no additional cuts made on jet substructure (assuming $\delta_S = 0$) [left]. Then we provide the results as a function of $\tilde{\Lambda}$ taking $\beta = 2$ [middle] and $\beta = 0.5$ [right]. The resulting reduction in the needed ϵ as a result of the substructure cut is presented as a multiplicative factor below the middle and right plots. We vary the luminosity and provide results with and without errors, see the legend for details. 40
12. Pair production $\phi_q\phi_q^\dagger \rightarrow \phi\phi^\dagger$ through the t -channel exchange of a heavy complex scalar Φ . The EFT description can be obtained by expanding and truncating the t -channel propagator, yielding a series of local operators. 47
13. Pair production $\phi_q\phi_q^\dagger \rightarrow \phi\phi^\dagger$ through the s -channel exchange of a heavy singlet scalar S . The EFT description can be obtained by expanding and truncating the s -channel propagator, yielding a series of local operators. 49

14. A series of EFT operators with more powers of fields generated by insertions of the self trilinear coupling in the s -channel model. Dashed lines denote the heavy scalar mediator S ; solid lines denote light particles, either scalar quarks or the BSM singlet scalars ϕ 51
15. $\Omega_{t,\text{UV}}$ computed using the t -channel UV model as a function of the center-of-mass energy E_{cm} for parton and hadron initial states. This shows that the UV theory is free of perturbative unitarity violation, when the couplings are taken to be $\lambda_{q\phi} = |\mu_{q\phi}|^2/M^2 = 8\pi$ 63
16. $\Omega_{t,\text{EFT}}$ computed using the EFT expansion of the t -channel model as a function of the center-of-mass energy E_{cm} , for low choices of the truncation dimension $\Delta = 6 + 2k$. For the Partonic Initial State case [left], when $\Delta > 0$, $\Omega_{t,\text{EFT}}$ grows at large E_{cm} and approaches infinity as $E_{\text{cm}} \rightarrow \infty$. This tells us there will be a perturbative unitarity cutoff for a critical value of E_{cm} . In the Hadronic Initial State case [right], the growth of $\Omega_{t,\text{EFT}}$ is significantly delayed as compared to the partonic case. 64
17. The perturbative unitarity cutoff on E_{cm} as a function of the EFT truncation dimension Δ for the t -channel model, derived using Eq. (3.45). In the Partonic Initial State case [left], the perturbative unitarity cutoffs are more severe than for the Hadronic Initial State case [right], although the PDF effects do not fully remove the bounds. 64
18. The shaded region shows the parameter space where the EFT is invalid for the t -channel model in the plane of the EFT truncation dimension Δ versus the BSM scale M with $\lambda_{q\phi} = 8\pi$. In the Partonic (Hadronic) Initial State case, we take $\sqrt{\hat{s}}$ (\sqrt{s}) = 14 TeV. The inclusion of PDF effects opens up a region of potentially viable parameter space. 65
19. $\Omega_{s,\text{UV}}$ computed using the s -channel UV model as a function of the center-of-mass energy E_{cm} . This shows that the UV theory is free of perturbative unitarity violation, when the couplings are taken to be $\lambda_q = \mu_q\mu_\phi/M^2 = 2$ 66
20. The shaded region shows the parameter space in the plane of the EFT truncation dimension Δ versus the BSM scale M with $\lambda_q = 2$, where the EFT is deemed invalid using the criterion in Eq. (3.45) for the s -channel model. In the Partonic (Hadronic) Initial State case, we take $\sqrt{\hat{s}}$ (\sqrt{s}) = 14 TeV. The inclusion of PDF effects opens up a region of potentially viable parameter space. 66

21. The absolute value of the relative error (see Eq. (3.55)) computed for the t -channel model as a function of the EFT truncation dimension Δ . For the “Partonic Initial State” case [left], we present curves for $M < \sqrt{\hat{s}} = 14$ TeV, which show that the error grows monotonically as Δ is increased. In the “Hadronic Initial State” case [right], we present curves for $M < \sqrt{s} = 14$ TeV, which show that the EFT approximation improves for small values of Δ , but then the error begins to grow for $\Delta > \Delta_{\text{crit}}$ 73
22. The relative error (see Eq. (3.55)) as computed for the t -channel model in the “Hadronic Initial State” case for $M < \sqrt{s} = 14$ TeV. 73
23. The ratio $\sigma_{t,\text{EFT}}^{[k]}/\sigma_{t,\text{UV}}$ for the first few $\Delta = 6 + 2k$ as a function of M . For the “Partonic Initial State” case [left], the series converges for $M > \sqrt{\hat{s}}$ and diverges for $M < \sqrt{\hat{s}}$. For the “Hadronic Initial State” case [right], the series converges for $M > \sqrt{s}$ and appears to be converging when $M \lesssim \sqrt{s}$ (although it actually diverges for $\Delta > \Delta_{\text{crit}}$). 74
24. The size of the r^{th} term $|\sigma_{t,\text{EFT}}^{(r)}/\sigma_{t,\text{UV}}|$ as a function of r . In the “Partonic Initial State” case [left], we have $M < \sqrt{\hat{s}} = 14$ TeV; the term grows monotonically with r . In the “Hadronic Initial State” case [right], we have $M < \sqrt{s} = 14$ TeV; the term tends to decrease with r for small r (for $M \gtrsim 5$ TeV), and then begins to increase for large r 75
25. A comparison of the perturbative unitarity results against the t -channel cross section predictions for two choices of the UV parameters: $\lambda_{q\phi} = 8\pi$ [left] and $\lambda_{q\phi} = 2$ [right]. The shaded regions are the perturbative unitarity bounds. The contours show constant power counting uncertainty. This provides evidence that valid EFTs exist in the region excluded by the naive partonic perturbative unitarity bound. 76
26. The relative error (see Eq. (3.55)) as computed for the s -channel model in the “Hadronic Initial State” case for $M < \sqrt{s} = 14$ TeV and $m_\phi = 1$ TeV. 77
27. The relative error (see Eq. (3.55)) as computed for the s -channel model in the “Hadronic Initial State” case where $\Gamma \rightarrow 0$ for $M < \sqrt{s} = 14$ TeV and $m_\phi = 1$ TeV. For $\Delta < \Delta_{\text{crit}}$, the EFT prediction appears to be converging to the wrong value. 77
28. A comparison of the perturbative unitarity results against the s -channel cross section predictions for two choices of the UV parameters: $\lambda_q = 2$ [left] and $\lambda_q = 2/(4\pi)$ [right]. The shaded regions are the perturbative unitarity bounds. The contours show constant power counting uncertainty. This provides evidence that valid EFTs exist in the region excluded by the naive partonic perturbative unitarity bound. 78

29. Perturbative unitarity bounds in the Δ versus M plane for various choices of a minimum energy cut E_{\min} [left] and of a maximum energy cut E_{\max} [right] for the t -channel model with $\lambda_{q\phi} = 8\pi$. The region that is incompatible with hadronic perturbative partial-wave unitarity is to the left of the curves. 80
- B.1. A comparison of the perturbative unitarity results against the t -channel cross section predictions for two choices of the UV parameters: $\lambda_{q\phi} = 8\pi$ [left] and $\lambda_{q\phi} = 2$ [right] in the case that the final state particles have a mass of 10 GeV. The shaded regions are the perturbative unitarity bounds, while the contours show power counting error. 98
- B.2. A comparison of the perturbative unitarity results against the s -channel cross section predictions for two choices of the UV parameters: $\lambda_q = 2$ [left] and $\lambda_q = 2/(4\pi)$ [right] in the case that the final state particles have a mass of 10 GeV. The shaded regions are the perturbative unitarity bounds, while the contours show power counting error. 99
- B.3. Perturbative unitarity bounds in the Δ versus M plane for various choices of a minimum energy cut E_{\min} [left] and of a maximum energy cut E_{\max} [right] for the t -channel model with $\lambda_{q\phi} = 8\pi$ in the case that the final state particles have a mass of 10 GeV. The region that is incompatible with hadronic perturbative partial-wave unitarity is to the left of the curves. 99

LIST OF TABLES

Table	Page
1. List of variables within the PYTHIA 8.240 Hidden Valley module, along with the default choices made for the study performed here. All of these variables should be prepended with “HiddenValley:” when being called within PYTHIA. Note that <code>spin_qv</code> (<code>alphaFSR</code>) are derived from <code>spinFv</code> (<code>Lambda</code>), which is why they are marked with “—” in the table. Decay tables for the dark mesons must additionally be specified.	17

CHAPTER I

INTRODUCTION

The physics program at the Large Hadron Collider (LHC) has reached a very mature stage. Run II is now completed, and ATLAS and CMS each have $\sim 150 \text{ fb}^{-1}$ of 13 TeV data to explore. This data has already taught us a variety of lessons regarding the Standard Model and beyond, but detection of new physics has thus far remained elusive. Given the strong theory motivations provided by, e.g. supersymmetry and/or WIMP dark matter, most signal regions have been developed to target perturbative extensions of the Standard Model, which yield relatively clean, easily interpretable observables. This is made sharp by the notion of Simplified Models [1, 2, 3], which typically introduce one or two new physics states whose dynamics and interactions can be fully captured via a few additional terms that one adds to the Standard Model Lagrangian. However, not all Standard Model extensions have collider signatures that can be captured in the weakly-coupled Simplified Model framework. A good understanding of the novel signal regions associated with more out-of-the-box ideas is crucial to achieving full coverage when searching for new physics potentially being produced at the LHC.

Searches for new physics at the LHC largely fall into two categories: (1) hunting for the signatures of the direct production of new particle(s) and (2) looking for the indirect imprint of new heavy physics on the final state distributions of Standard Model particles. In order to parameterize the space of possible new physics effects, it is typical to utilize the theoretical frameworks of (1) Simplified Models and (2) Effective Field Theory (EFT) extensions of the Standard Model (perhaps including other light states, e.g. a dark matter candidate). These theory platforms provide a principled way to design signal regions, in that they allow us to optimize sensitivity to

Beyond the Standard Model (BSM) physics. The theory also gives an interpretation of either a null result or, all the better, a discovery of something new. Therefore, it is of paramount importance that we ensure that our signal model frameworks are robust. While this is typically straightforward for (perturbative) Simplified Models, it can be significantly more subtle when it comes to EFTs.

This dissertation comprises two analyses of extensions to the Standard Model. We first investigate to what extent a particular class of models, namely hidden sectors with a new confining gauge group, can be parameterized if there are no collider stable BSM final states. By assuming the dynamics of the hidden sector is similar to QCD, we develop a novel procedure for quantifying the uncertainty of measuring the substructure of parton showers. We then explore the discovery potential of looking for BSM signatures that mimic QCD signatures utilizing substructure.

Next, we present a revised formalism for EFT interpretations of experiments performed in hadron colliders. Rather than searching for signatures directly, the EFT framework provides a more model agnostic approach for parameterizing BSM physics compared to Simplified Models. However, as we demonstrate, utilizing EFTs for hadron level processes requires incorporating Parton Distribution Functions (PDFs) into the formalism. Our work establishes a methodology for applying EFT techniques in a hadronic environment while underscoring the nuances of the energy scaling in EFT expansions.

1.1 Jet Substructure in Dark Sectors

In Ch. II, we explore the idea that the dark matter could be a stable remnant of some new strong dynamics that resides in a hidden sector [4, 5, 6, 7, 8, 9, 10, 11, 12, 13, 14, 15, 16, 17, 18, 19, 20, 21, 22, 23, 24, 25, 26, 27, 28]. It is then reasonable to

assume the presence of some non-gravitational connection to the visible sector, such that the hidden sector was in thermal contact with the Standard Model at some point in the early Universe. This could result from a renormalizable interaction involving the Higgs, Neutrino, and/or Hypercharge Portals [29, 30, 31] or could be due to the exchange of some new mediator. Depending on the properties of the portal, it could be possible to access the hidden sector at the LHC. Furthermore, the dark strong dynamics could obfuscate the resultant signatures, as has been demonstrated concretely through many examples, e.g. lepton jets [32, 33, 34, 35, 36, 37], emerging jets [38, 39, 40], semi-visible jets [41, 42, 43, 44], and soft bombs [6, 14].

All of these examples share a common characteristic: a hard collision can generate a dark sector parton that subsequently undergoes a dark sector parton shower. This often yields a high multiplicity of soft final state particles, smearing out the kinematics of the underlying partons and making it difficult to distinguish the associated signal against large backgrounds. There is a further practical complication due to the fact that these signatures rely on the presence of dark strong dynamics — the theoretical predictions are not nearly as well understood as in the Simplified Model case. As a result, searches for this class of models are usually designed to be very inclusive, avoiding over reliance on details of the modeling. The resulting trade-off between signal significance and systematic error mitigation motivates the work presented here: our goal is to understand the systematic uncertainties associated with making predictions that rely on dark sector strong dynamics. An appreciation of which aspects of the observable can be reliably considered is crucial for the optimization of resulting search strategies.

Specifically, we focus on scenarios where the dark hadrons that result from a dark sector shower promptly decay back to Standard Model hadrons. Our goal is to explore

the properties of the resulting jets' substructure, and to quantify the uncertainty inherent to making such predictions. Since substructure is sensitive to a variety of IR effects, such as the dark hadron mass spectrum and hadronization model, our work provides an observable-driven window into the systematic issues associated with making predictions for these strongly coupled dark sector scenarios.

As the use of jet substructure has become routine (see Refs. [45, 46, 47, 48, 49, 50, 51, 52, 53] for some reviews), many observables have been proposed to distinguish quark and gluons, or to tag boosted objects, and applications to dark sector showers have also been previously explored [43]. Detailed comparisons of parton and hadron level predictions for substructure observables have been performed in the context of the Standard Model, e.g. see the Les Houches 2017 report [54]. Of particular interest here are variables that were designed to be sensitive to the showering history of a jet, since our goal is to find ways to distinguish QCD jets from those that resulted from showering within a dark sector. We are also interested in taking advantage of advancements in analytic calculations that rely on resummation techniques to capture the showering contribution to substructure. To this end, our benchmark observable will be the energy correlation function $e_2^{(\beta)}$ [55], where β controls the sensitivity to wide-angle radiation; see Eq. (2.1) below for details. We choose to focus on $e_2^{(\beta)}$ since this family of observables is primarily sensitive to the gauge charge of the associated parton in the underlying hard process, which could be our only handle for uncovering dark shower signatures.¹

¹A number of observables has been considered for the problem for quark/gluon discrimination that are expected to provide superior discrimination to $e_2^{(\beta)}$. These include both intrinsically IRC unsafe variables like track multiplicity or N_{95} [56], and also more complicated IRC safe observables that try to exploit correlations between multiple particles to approximate the behavior of these multiplicity variables [57, 58, 59]. The distributions of these observables are dominated by non-perturbative corrections, as discussed in more detail in Sec. 2.1.1. For QCD, this information can be extracted from suitably chosen control regions, while in the case of a new hidden sector, our only recourse is to appeal to phenomenological models whose systematics are challenging to quantify.

There is potential concern when predicting the efficiency of jet-substructure assisted searches. The discriminating power of nearly all substructure observables only becomes calculable if large logarithms that can appear in perturbation theory are resummed to all orders. If this calculation is performed using a Monte Carlo generator such as PYTHIA, only the leading logarithms (LL, defined in Sec. 2.1) are correctly captured, resulting in large expected theory uncertainties, which cannot be quantified by running the generator alone.² For QCD studies, such concerns are partially ameliorated by the fact that the parameters of generators are tuned to real data, allowing them to often match the real world better than their formal accuracy would suggest. When looking for physics beyond the Standard Model that we have not yet observed, we have no such recourse. To better address this state of affairs, we take advantage of theoretical technology developed to resum the soft and collinear QCD logarithms that contribute to $e_2^{(\beta)}$ at leading and next-to-leading logarithmic order along with modern numerical implementations within PYTHIA. Sensibly enveloping across the spread of associated predictions will allow us to quantify the systematic error band that is the main result of this work. These error bands can then be utilized to consistently include substructure information into LHC searches for dark sector physics.

This implies that the ability to extract meaningful limits using such observables is significantly reduced, and so we will not consider them at this time.

²Automating parton showers beyond leading log and leading color is extremely challenging. Some progress towards formalizing the problem was made in Ref. [60], followed by a numerical approach to address aspects of subleading color in Ref. [61]. For recent progress in automating aspects of next-to-leading-logarithm accurate parton showers, see Refs. [62, 63, 64], with a recent candidate full proposal in Ref. [65].

1.2 Unitarity Bounds on Effective Field Theories

As we turn to EFTs in Ch. III, we investigate the role of EFT validity at hadron colliders. The reason that EFT validity is an interesting question stems from the starting assumption of the EFT approach: it is necessarily a low energy approximation of a BSM theory that is associated with a dimensionful scale M (the mass of a heavy BSM state in simple UV completions). It is often the case that a search for EFT effects at the LHC yields a limit on this scale $M \geq M_{\text{limit}}$ with $M_{\text{limit}} < \sqrt{s}$ [66, 67, 68, 69, 70, 71, 72, 73], where \sqrt{s} is the center-of-mass energy of the collisions. When confronted with such a result, one should worry that the EFT approach is inconsistent (see e.g. [74, 75, 76, 77]). In this work, we will investigate this question by assessing the impact of the proton’s structure on one of the necessary conditions for EFT validity, namely that its scattering amplitudes satisfy perturbative partial-wave unitarity.³ We will provide a formalism for convolving matrix elements with PDFs, and will investigate the consequences of including PDFs on the region of EFT parameter space with $M < \sqrt{s}$.

In order to better understand why PDFs are important, it is useful to recall that an EFT is an expansion that is organized using a “power counting” parameter $\sim 1/M$; see Sec. 3.2.3 for a more detailed discussion. Dimensional analysis implies that (tree-level) EFT observables yield a power series in E/M , where E is a characteristic scale of the collision. If $E = \sqrt{s}$ (e.g. as it would for an e^+e^- collider) and $M \lesssim \sqrt{s}$, the series would diverge. We interpret this theoretical inconsistency as telling us that the EFT in this region of parameter space does not provide a useful description for interpreting the results of the experimental search.

³We emphasize that when this condition is not satisfied, what actually breaks down is the perturbative calculation itself, since we expect that the theory is fundamentally unitary. The bounds derived here should be interpreted as a necessary condition for the EFT to potentially have a perturbative UV completion.

At a hadron collider, the relevant scale is $E = \sqrt{\hat{s}}$, the *partonic* center-of-mass energy, which varies from collision to collision as determined by the PDFs. When designing a signal region, one is typically interested in keeping statistical fluctuations under control, which requires choosing cuts that accept events with a non-trivial range of $\sqrt{\hat{s}}$ values. For the ensemble of events isolated by these cuts, the relevant scale on average is $E = \sqrt{\hat{s}_{\text{ave}}}$, which can be much smaller than \sqrt{s} due to the PDF suppression of high-energy partons. This is why it requires a detailed investigation of a given search to determine if accounting for PDFs could salvage the EFT parameter space where $M \ll \sqrt{s}$, such that a meaningful bound can be extracted.

We emphasize that the necessity to convolve the parton-level amplitudes with the PDFs is a consequence of the following statements:

- The validity of an EFT depends on the experiment being performed (for our purposes here, specific to a single search region). The same EFT could be valid for one experiment, but not another, as they may use different cuts (or be at colliders with different collision energies).
- The only physical scattering matrix elements at a hadron collider have hadrons in the initial state (not partons).
- If the cuts used to design an experimental search region allow for a range of parton level energy scales, then one should take an ensemble average over the parton-level scattering matrix elements to determine the EFT validity for a proton level matrix element.⁴

In order to provide a quantitative discussion that is conceptually straightforward to interpret, we will be working with simple example UV toy models throughout

⁴One might be able to isolate the “parton” level matrix element to a very good approximation by changing the cuts appropriately, but this would correspond to a different “experiment.”

Ch. III, leaving a detailed analysis of more realistic situations to future work. This will allow us to derive a concrete EFT expansion by matching to the UV model, which we can use to probe the physics associated with the regions that are deemed invalid. For an experimental search that includes a range of $\sqrt{\hat{s}}$, PDF effects can significantly shift the perturbative unitarity bounds on EFT validity into the region where $M \ll \sqrt{s}$. Interestingly, this conclusion begins to break down as one includes higher-and-higher terms in the E/M expansion; eventually there are enough $\sqrt{\hat{s}}$ factors in the numerator to beat the strong PDF suppression at large momentum fraction. Therefore, one of our main results is that any claim of EFT validity for a given search region requires knowing both the scale M and the maximum dimension Δ (the truncation dimension) of the EFT operators. We conclude that the question of when one can consistently use EFTs to perform searches at a hadron collider depends on both *theoretical and experimental* considerations.

CHAPTER II

JET SUBSTRUCTURE IN DARK SECTORS

Throughout this chapter, we assume the dark sector includes \tilde{n}_F families of dark quarks which bind into dark hadrons at energies below some dark confinement scale $\tilde{\Lambda}$ due to a non-Abelian dark $SU(\tilde{N}_C)$ gauge group. Dark quarks will be produced with large transverse momentum $p_T \gg \tilde{\Lambda}$ such that they shower and hadronize, yielding jets of dark hadrons. We assume that these dark hadrons decay promptly back to Standard Model quarks,¹ yielding QCD-like jets. We then explore the impact on the $e_2^{(\beta)}$ observable as we vary the dark sector parameters $\tilde{\Lambda}$, \tilde{n}_F , \tilde{N}_C , and the effect of making the dark quarks massive. In addition, we provide an approximate characterization of the non-perturbative uncertainties associated with dark hadronization by exploring the impact of varying the phenomenological parameters associated with the Lund string model [78]. We then use our error bars to estimate the extent to which dark sector showers can be distinguished from QCD when including the impact of substructure.

The rest of this chapter is organized as follows. In Sec. 2.1, we introduce the two-point energy correlation function, which will be used as our benchmark substructure variable. We then review how to calculate this observable to next-to-leading-logarithmic accuracy utilizing traditional resummation techniques. Our enveloping procedure that combines the analytic predictions with numerical results derived from PYTHIA is then introduced, and provides a proxy for the systematic error associated with making a dark substructure prediction. In Sec. 2.2, we present the extent to which the substructure changes as a function of some of the dark sector parameters: the dark confinement scale $\tilde{\Lambda}$, the number of dark colors \tilde{N}_C , dark flavors

¹Decays to gluons are also in principle possible but to have them dominate the decay rate would require more involved model building.

\tilde{n}_F , and the dark quark mass \tilde{m}_q . In Sec. 2.3, we explore the effect of varying the parameters that model the dark sector hadronization. In Sec. 2.4, we estimate our ability to experimentally probe a dark sector jet against the QCD background. In App. A, we detail the expressions that are used to derive the analytic contributions to our systematic error envelopes.

2.1 Substructure Observables with Error Envelopes

A large array of jet substructure observables and algorithms have been developed, and are being combined in analyses in increasingly complicated ways. However, the majority of substructure techniques are designed to find evidence of hard processes buried within boosted hadronic events,² and as such, most observables are optimized for the identification of distinct multi-prong structures within a jet. A dark sector has no guarantee that it will produce such structure. Instead, we are interested in observables that are sensitive to the structure of the color charge and gauge group of the radiation making up the parton shower. This problem is closely analogous to the problem of quark/gluon discrimination in QCD, and we may look to prior work in this context for guidance [81, 82, 83, 84, 85, 86, 56, 87, 88, 89, 90, 55, 91, 92, 93, 94, 95, 96, 97, 59]. Additionally, we would like to work with infrared and collinear (IRC) safe observables, so that they are perturbatively calculable. This is particularly important for a dark sector search since, unlike the situation for QCD, we have no data from which to extract any of the non-perturbative parameters which are required to make predictions. Thus, there is no way to estimate their uncertainties without resorting to *ad hoc* empirical models.

²For signals that yield high multiplicity final states via perturbative decays, so-called “accidental substructure” can also provide a useful handle, e.g. see [79, 80].

These two considerations almost uniquely limit us to considering observables which characterize the angular spread of radiation within the jet. A representative choice is the two-point energy correlation function [55], defined as

$$e_2^{(\beta)} = \sum_{i < j \in J} z_i z_j (\theta_{ij})^\beta, \quad (2.1)$$

where β is the angular dependence parameter that determines how sensitive the variable is to the angular distribution of the radiation. The jet algorithm determines the constituent particles in jet J that are summed over in Eq. (2.1). In the context of a hadron collider like the LHC, it is most useful to define $z_i \equiv p_{T_i}/p_{T_J}$ and $\theta_{ij} \equiv R_{ij}/R_0$, where p_{T_J} is the total p_T of the jet, R_{ij} is the Euclidean distance between the i^{th} and j^{th} partons in the η - ϕ plane, and R_0 is the jet radius.³ For brevity, we will usually drop the (β) superscript below when making general statements, and will also refer to the two-point energy correlation function as the energy correlator when appropriate from context. Note that $e_2^{(\beta)}$ is equivalent to the $C_1^{(\beta)}$ variable introduced in Ref. [55] and widely used in experimental studies [98, 99, 100].

To build intuition, one can consider a jet with two constituents; in the infrared and collinear limit, the jet mass is given by $m^2/p_T^2 \simeq z_1 z_2 (\theta_{12}/R_0)^2$, such that $e_2^{(2)} \simeq m^2/p_T^2$. Hence, $e_2^{(\beta)}$ can be seen as a generalization of jet mass that incorporates arbitrary angular dependence. It is also closely related to the family of jet angularities [101, 102], without the need to define a jet axis.

³For an e^+e^- collider, a more convenient choice would be $z_i \equiv E_i/E_J$ and $\theta_{ij} \equiv 2p_i \cdot p_j/E_i E_j$ or the actual Euclidean angle between the i^{th} and j^{th} partons. In the strict collinear limit, all these definitions collapse to be equivalent, and thus only differ in terms that are non-singular in the small $e_2^{(\beta)}$ limit. We choose to normalize θ_{ij} by the jet radius R_0 to eliminate the leading dependence on R_0 .

Our essential idea is to calculate the distributions of interest analytically and numerically assuming various approximations, and then use these to determine an error bar such that it spans the range of predictions. First, we review the analytic calculation of the resummed substructure distributions at leading and next-to-leading log order, followed by a brief discussion of the numerical implementation using `PYTHIA`. Then, we explain how we combine the various approximations into an error envelope in the context of a QCD calculation. This will set the stage for Sec. 2.2, where we explore the range of predictions for the substructure distributions resulting from a dark sector shower.

2.1.1 Analytics Using Traditional Resummation Techniques

To understand the robustness of the e_2 distributions, it is useful to explore the range of predictions that result from analytic techniques for calculating the normalized differential cross section. These formulas were derived in Ref. [103], and we present a summary of the main steps for the calculations in App. A. The collinear limit of the leading order e_2 distribution generates a collinear logarithm from the integral over the splitting angle θ and a soft logarithm from the integral over the momentum fraction z . Enforcing the kinematics of two-body momentum conservation with a delta function, we can write down the differential distribution for e_2 by appealing to the definition in Eq. (2.1):

$$\frac{1}{\sigma} \frac{d\sigma_i^{\text{LO}}}{de_2} = \frac{\alpha_s}{\pi} \int_0^{R_0} \frac{d\theta}{\theta} \int_0^1 dz p_i(z) \delta\left(z(1-z)\left(\frac{\theta}{R_0}\right)^\beta - e_2\right), \quad (2.2)$$

where R_0 is the jet radius⁴ and $p_i(z)$ is the appropriate parton splitting function for a quark-initiated jet or a gluon-initiated jet, which are given by

⁴Although we work in a small jet radius limit, this is known to be a reasonable approximation even up to $R_0 \sim 1$ [104, 105].

$$\begin{aligned}
p_q(z) &= P_{g \leftarrow q}(z) = C_F \frac{1+z^2}{1-z}, \\
p_g(z) &= \frac{1}{2} P_{g \leftarrow g}(z) + n_F P_{q \leftarrow g}(z) \\
&= C_A \left(\frac{z}{1-z} + \frac{1-z}{z} + z(1-z) \right) + n_F T_R (z^2 + (1-z)^2), \quad (2.3)
\end{aligned}$$

where $T_R = \frac{1}{2}$ is the index of the quark representation, i.e., the fundamental representation. These splitting functions encode the divergences associated with a shower that is initiated by the emission of a soft gluon.

In the limit where $e_2 \ll 1$, we can simplify $z(1-z)(\theta/R_0)^\beta \simeq z(\theta/R_0)^\beta$ by assuming $z \ll 1$. It is then straightforward to evaluate Eq. (2.2), which yields

$$\frac{e_2}{\sigma} \frac{d\sigma_i^{\text{LO}}}{de_2} \simeq \frac{2\alpha_s}{\pi} \frac{C_i}{\beta} \left(\ln \frac{1}{e_2} + B_i + O(e_2) \right), \quad (2.4)$$

where $C_q = C_F = \frac{N_C^2-1}{2N_C}$ and $C_g = C_A = N_C$ are the color factors associated with the jet, and $B_q = -\frac{3}{4}$ and $B_g = -\frac{11}{12} + \frac{n_F T_R}{3C_A}$ encode the subleading terms in the splitting functions that arise from hard collinear emissions. Identifying the characteristic logarithm $L \equiv \ln(1/e_2)$, the cumulative distribution at leading order exhibits a characteristic double logarithm in the limit of small e_2 :

$$\Sigma_i^{\text{LO}} \equiv \int_0^{e_2} dx \frac{1}{\sigma} \frac{d\sigma_i^{\text{LO}}}{dx} = 1 - \frac{\alpha_s}{\pi} \frac{C_i}{\beta} \left(L^2 + 2B_i L + O(L^0) \right). \quad (2.5)$$

This shows that perturbation theory breaks down in the limit of small e_2 , so we would like to resum this double logarithm to derive a convergent prediction.

The authors of Refs. [106, 107] derived a concise expression for the next-to-leading logarithmic (NLL) resummation of the cumulative distribution for recursively

IRC safe observables such as e_2 :

$$\Sigma_i^{\text{NLL}} = \frac{e^{-\gamma_E R'_i}}{\Gamma(1 + R'_i)} e^{-R_i} e^{-\frac{\alpha_s}{\pi}(R_{1,i} - G_{2,i}L^2 - G_{1,i}L)}, \quad (2.6)$$

where the “radiator” R_i is given by

$$R_i = \int_0^{R_0} \frac{d\theta}{\theta} \int_0^1 dz p_i(z) \frac{\alpha_s(\kappa)}{\pi} \Theta\left(z \left(\frac{\theta}{R_0}\right)^\beta - e_2\right), \quad (2.7)$$

with $R'_i \equiv \frac{dR_i}{dL}$ and $\kappa = z\theta p_{TJ}$, and $R_{1,i}$ is the fixed-order (FO) correction at next-to-leading order, which allows one to match (in the Log- R scheme [108]) between the resummed and perturbative regimes, ensuring the appropriate kinematic endpoint is respected. As such, $G_{2,i}L^2$ and $G_{1,i}L$ are the logarithms appearing in the fixed-order expression (in the collinear limit) that must to be subtracted to avoid double counting the resummed logarithms. Simplifying $z(1-z)$ to z in Eq. (2.2) is justified by the identical structure of the two collinear limits and is compensated by a suitable combinatoric factor, as further discussed in App. A.

In the context of quark/gluon discrimination, a number of observables have been proposed that seemingly satisfy our property of being perturbatively calculable while claiming to offer improved discrimination over the energy correlation function above [57, 58, 59]. This comes at a price. Instead of contributions from individual emissions contributing linearly to the observable, each emission’s weight depends on the entire shower history. However, this feature also increases the resulting sensitivity to non-perturbative corrections by reducing the parametric suppression of these effects, and until more detailed understanding of these features is available, it is difficult to recommend the use of such substructure variables in situations where these effects cannot be constrained by data. Note that even in the case of the better

understood $e_2^{(\beta)}$, the β dependence of quark/gluon discrimination has been measured, and it noticeably deviates from that of the perturbative predictions [109].

An analytic evaluation of R_i is possible, although challenging, e.g. see Ref. [110]. The calculation of the resulting efficiencies at NLL due to a cut on e_2 requires evaluating the gauge coupling α_s at two-loop order using the CMW scheme [111], such that efficiencies still need to be computed numerically. Another issue is related to α_s becoming non-perturbative as the integral is evaluated at low enough scales. To mitigate these complications, we follow the procedure outlined in Ref. [103]: the coupling is only run at one-loop order and is frozen at a “non-perturbative scale” $\mu_{\text{NP}} = 7\Lambda$, where the factor of 7 is an arbitrary choice. This allows us to find a closed-form solution to Eq. (2.7) at the expense of limiting its logarithmic accuracy. We will call this approximate evaluation of Eq. (2.6) the “modified leading logarithmic” (MLL) resummed cumulative distribution with FO corrections. All analytic distributions presented will be MLL+FO accuracy (with the exception of Fig. 1).

2.1.2 Numerics From Pythia

Our analytic expressions have the benefit that they are transparent, in that we can precisely identify the approximations that go into the calculations. However, they do not account for important corrections from, e.g. hadronization or finite quark masses. They also do not provide any way for us to assess the impact of dark sector hadronization on our prediction. To address these shortcomings, we compare our results for the e_2 observables to those of a Monte Carlo parton shower that models a new confining gauge group. Although all parton showers in common use are formally accurate to leading log, they include various corrections with the goal of modeling certain higher order effects, e.g. see the Monte Carlo Event Generators

review in Ref. [112]. It is worth emphasizing here that all such corrections assume QCD, and as such should be revisited in the context of more general confining theories. Specifically here, we simulate events using PYTHIA 8.240 [113]. We simulate pp collisions at $\sqrt{s} = 14$ TeV including initial- and final-state radiation (without multiple parton interactions) for all our events. The signal is generated via a direct portal from $\bar{q}q$ pairs to dark sector quarks, and the evolution of the dark sector is implemented in PYTHIA's Hidden Valley module [10, 11, 12], including a dark parton shower, hadronization, and decay back to Standard Model states. Events are clustered into anti- k_t jets [114] with radius $R_0 = 1.0$ and e_2 computed for each jet using FASTJET 3.3.2 [115], subject to a jet-level cut of $p_T > 1$ TeV.

We will briefly comment on the implementation of the parton shower in PYTHIA's Hidden Valley module.⁵ The underlying physics model is the same as that used for the time-like QCD shower. Showering proceeds via the emission of a dark gluons from both dark quarks and gluons. The dark quarks may be duplicated up to eight flavors, \tilde{n}_F , with identical masses and integer spin by default (we set the dark quark spin to be 1/2). Running of the dark gauge coupling is included up to one-loop for an arbitrary $SU(\tilde{N}_C)$ gauge group, assuming massless quarks. Although the functionality to include an arbitrary dark quark mass spectrum is available, we take the masses \tilde{m}_q to be degenerate throughout this study. We do not include any states that are charged under both the Standard Model and dark sector symmetry groups, although such states may be considered to extend the range of phenomenological handles in the resulting signal.

A number of aspects of our analytic calculation make its perturbative accuracy greater than that of the PYTHIA parton shower. Dark gluon splitting into quark pairs

⁵For a more complete discussion, see the corresponding section of the PYTHIA manual: <http://home.thep.lu.se/~torbjorn/pythia82html/HiddenValleyProcesses.html>.

Model		Showering		Hadronization	
<code>Ngauge</code>	3	<code>FSR</code>	on	<code>fragment</code>	on
<code>nFlav</code>	5	<code>alphaFSR</code>	—	<code>probVector</code>	0.75
<code>spinFv</code> ⁶	0	<code>alphaOrder</code>	1	<code>aLund</code>	0.3
<code>spinqv</code>	—	<code>Lambda</code>	1 GeV	<code>bmqv2</code>	0.8
<code>doKinMix</code>	off	<code>pTminFSR</code>	1.1 GeV	<code>rFactqv</code>	1.0

Table 1. List of variables within the PYTHIA 8.240 Hidden Valley module, along with the default choices made for the study performed here. All of these variables should be prepended with “HiddenValley:” when being called within PYTHIA. Note that `spinqv` (`alphaFSR`) are derived from `spinFv` (`Lambda`), which is why they are marked with “—” in the table. Decay tables for the dark mesons must additionally be specified.

is not currently implemented in PYTHIA; the $P_{q\leftarrow g}(z)$ splitting function is not singular in the soft limit, and therefore provides contributions beyond LL accuracy. A choice of minimum allowed p_T for emissions controls the termination of the shower at low scales. This threshold may be tuned to data in the case of QCD, but for a dark parton shower, this is a parameter that should not be much larger than the confinement scale. Matrix element corrections ensuring the accuracy of parton splitting to one-loop order are included in the QCD parton shower of PYTHIA but, being model-dependent, not for the Hidden Valley module. Comparing the analytic results to the PYTHIA predictions will estimate the resulting uncertainties, which are either included or (in the case of the p_T cut) have no impact on our analytic results.

The dark sector is assumed to confine, and hadronization is implemented via the Lund string model [78], which has some associated parameters whose values are unknown a priori. We explore the consequences of this fact below in Sec. 2.3. Hadronization proceeds exclusively to dark pions and dark rho mesons, which all

⁶`spinFv` controls the spin of particles charged under both the Standard Model and dark sector. If this flag is nonzero (zero), then the dark quark spins are forced to be either 0 or 1 (1/2).

decay back to the Standard Model using flat matrix elements (assuming no flavor symmetries leading to stable dark mesons, see e.g.Refs. [42, 44]). Table 1 enumerates the relevant parameters discussed along with their default settings.

2.1.3 Error Envelopes

In this section, we describe the procedure used to compute the error envelopes presented in Sec. 2.2. To capture the “perturbative” theoretical uncertainty associated with these distributions, we combine a number of variations that probe the systematic uncertainties inherent to making dark shower predictions. First, to incorporate uncertainties in the showering step, we capture the range of parton level predictions by comparing the LL order and the MLL + FO order analytics (which we refer to as MLL in the figures). Next, we compare the MLL order analytics and the parton level numerics, i.e., turning off hadronization. Finally, we compare the parton level and the hadron level numerics to account for the effects of hadronization. For events originating from a dark sector shower, we also compare the dark hadron level and the visible hadron level numerics to capture the effects of decaying dark hadrons and their subsequent recombination into Standard Model hadrons. To construct our error bands, we sum the widths of these comparison sub-envelopes in quadrature to produce an averaged final envelope. The results of this procedure when applied to QCD are presented in Fig. 1. Note that for the later plots we show the central value of the envelope merely to guide the eye; this curve does not simply follow from our analytic results. Then in Sec. 2.3 below, we investigate the uncertainty due to hadronization modeling. The total error band that includes the perturbative and hadronization errors is then used as the input to our search sensitivity estimates for the LHC presented in Sec. 2.4.

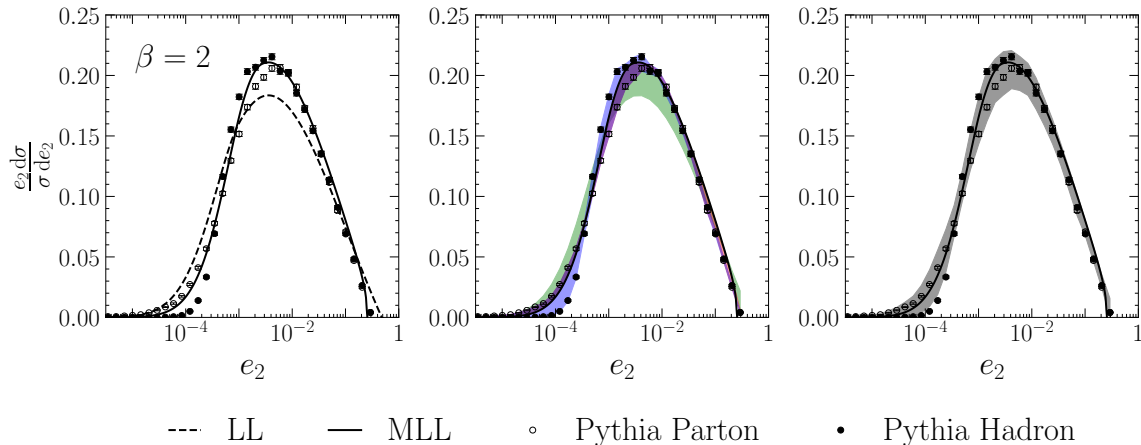


Figure 1. Illustration of the enveloping procedure utilized to estimate theory systematic errors as applied to QCD, for $p_T = 1$ TeV jets. The analytic and numerical predictions for the e_2 distributions are shown assuming various levels of approximation as detailed in the legend [left panel].⁷ These predictions are used to create error sub-envelopes [middle panel] that are then combined to result in the final envelope [right panel]. The green sub-envelope captures the difference between the LL and MLL analytic predictions. The red sub-envelope captures the difference between the MLL analytic prediction and the parton level numerical result from PYTHIA. The blue sub-envelope captures the difference between the parton and hadron level prediction from PYTHIA. These envelopes are added in quadrature to compute the total envelope [right panel]. Note that when computing envelopes for the dark sector, we include three numerical predictions when the final states are dark partons, dark hadrons, or visible hadrons. The angular dependence parameter is set to $\beta = 2$ for illustration.

We note that a common approach to calculating a theory uncertainty is to vary factorization, resummation, and (when considering exclusive observables) fragmentation scale parameters by a factor of two away from their canonical choices. This is a way of estimating higher-order terms that have not been explicitly computed by assuming they are dominated by their logarithmically enhanced pieces. The logarithms dominating our distributions are not due to a running effect so that uncertainties in the resummation procedure will not be captured by such an approach.

⁷Note that the excellent agreement between the analytic and numerical distributions here does not persist across parameter variations (and may actually be due to the fact that PYTHIA is tuned using jet mass as one of the inputs).

Theoretical uncertainties for resummed calculations typically require more involved multi-scale variational schemes using effective field theory frameworks.⁸

The enveloping approach advocated here is designed to incorporate this uncertainty, while also accounting for unknown details of the hadronization and decay properties of the dark sector. Our estimates of perturbative errors are comparable to those of the effective field theory scale variational approaches for QCD, where similar calculations have been done [118]. Depending on the precise treatment of the normalization when taking scale variations, it is possible to find significantly larger errors below the Sudakov peak (e.g. see Fig. 5 in Ref. [119]), where the interplay of constraints from the integrated cross section calculation and breakdown of resummation convergence makes uncertainties particularly sensitive to choice of scheme [120]. However, the resulting effect on signal yields is minimal, since such large uncertainties occur in a vary rapidly falling part of the distribution.

Before showing the results from varying parameters in the dark sector, we note that the analytic approximation for the radiator R_i used in our calculations is not continuously differentiable, see Eqs. (A.21) to (A.23). This is a consequence of sharply cutting off the integrals using the non-perturbative scale μ_{NP} introduced in Sec. 2.1.1 above, which leads to a kink in the second derivative of the radiator R_i'' . To avoid this issue, we follow Ref. [103] and replace this derivative with a discrete approximation:

$$R_i''(e_2) \simeq \frac{R_i'(e^{-\delta}e_2) - R_i'(e_2)}{\delta}, \quad (2.8)$$

where the choice $\delta = 1$ is an additional source of theoretical uncertainty that is negligible to single logarithmic accuracy.

⁸For work on adopting such variations in traditional resummation techniques, see Ref. [116]. Alternative schemes for estimating theory errors have also been introduced in the context of Standard Model calculations, e.g. see Ref. [117].

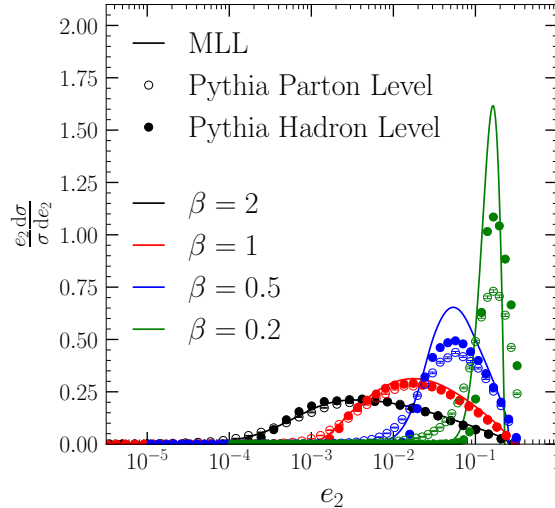


Figure 2. Dependence on the angular dependence parameter β in QCD for $p_T = 1$ TeV jets. We show the predictions derived using the MLL analytic calculation, along with the parton and hadron level numerical results from PYTHIA. Larger (smaller) angular dependence emphasizes the contribution from pairs of partons with larger (smaller) angular distance. The analytic calculations begin to break down for angular dependence values $\beta < 0.5$, which is reflected here in the fact that the $\beta = 0.2$ curve does not appropriately terminate at the kinematic endpoint.

Fig. 2 shows the analytic and numeric e_2 distributions for QCD jets across various angular dependence values β . We note the agreement between the analytic and the numeric distributions begin to diverge for low angular dependences $\beta < 0.5$. Furthermore, the $\beta = 0.2$ analytic distribution does not appropriately terminate at the kinematic endpoint. We conclude that even though we are working in parameter space where the resummation techniques should be a good approximation, the low angular dependence regime of e_2 is not well modeled. For this reason, we will focus our analysis on the behavior of the $e_2^{(2)}$ and $e_2^{(0.5)}$ to explore the impact of varying β .

From the definition of e_2 in Eq. (2.1), we see that increasing β gives greater weight to emissions at larger angular distances in the distribution. Since emissions at large angle within a jet are preferentially softer at large angles, giving lower weight to large-angle emissions leads to e_2 distributions closer to their kinematic endpoint,

behavior that is clearly reflected in Fig. 2. Simultaneously, the distribution of e_2 is dominated by emissions in singular regions of phase space, so that lower values of β provide more sensitivity to the structure of the collinear singularity of partonic splitting functions. This comes at the cost of loss of perturbative control. Sec. 2.1.1 makes clear that the effective coupling in the calculation of $e_2^{(\beta)}$ is α_s/β and that for values of $\beta \ll 1$, perturbative control of the e_2 distribution is lost throughout phase space.

2.1.4 Applying the Predictions

In addition to plotting the normalized e_2 distributions, we will provide a few different ways of presenting the predictions. We will show the cumulative cross section, which is derived by taking the differential distribution and numerically evaluating the following integral, see the bottom row of Figs. 3, 5, and 7:

$$\Sigma(x_{\text{cut}}) = \int_{x_{\text{cut}}}^{e_{2,\text{max}}} de_2 \frac{1}{\sigma} \frac{d\sigma}{de_2}, \quad (2.9)$$

where $e_{2,\text{max}} = \frac{1}{4}R_0^\beta$. To incorporate the error envelopes, we assume they are fully correlated. In practice, this simply means we compute the upper (lower) error envelope of the cumulative distribution by integrating the upper (lower) edge of the differential distribution. The choice of x_{cut} will be optimized below when we discuss the discovery potential of dark substructure in Sec. 2.4.

We also provide some quantitative insight into how different the signal and background distributions are using the MLL analytic predictions directly, see Figs. 4, 6, and 8. The left and middle panels of these figures provide two different figures of merit, which give a quantitative sense of how well one could distinguish signal from background, in this case approximated by quark initiated jets. Specifically, on the left we show ROC curves, which are the parametric curve that traces the background

rejection $1 - \epsilon_B$ as a function of signal acceptance ϵ_S , due to varying a cut on e_2 . The middle panels show the parametric curve for discovery significance $\epsilon_S/\sqrt{\epsilon_B}$ as a function of signal acceptance ϵ_S , again due to varying a cut on e_2 . The right panels show the change in the signal rate as a function of the dark sector parameter that is being varied, for a benchmark fixed background factor, which is taken to be $1 - \epsilon_B = 90\%$. As we will explore in the next section, these various ways of presenting the predictions provide additional insight into the behavior of the e_2 observable across the dark sector parameter space.

2.2 Distinguishing Dark Substructure from QCD

Now that we have established a method to estimate the theoretical uncertainties inherent to calculating substructure distributions, we will apply this technology to explore the range of predictions one can expect from a dark sector including error bars. This demonstrates the behavior of the dark sector as a function of its parameters. In particular, we will highlight how the uncertainties depend on the parameters. While we incorporate the effects of hadronization in this section, we set the hadronization parameters to their default values. The results presented here will be combined with an estimate of hadronic uncertainties in Sec. 2.3, which are computed by varying the non-perturbative parameters. These are then used as the inputs to the estimates performed in Sec. 2.4, where we study to what extent it is possible to distinguish dark sector showers from QCD via substructure measurements. Note that we have made the simplifying assumption that the QCD background is entirely composed of quark jets in what follows, since the signal will dominate in the central region of the detector. A more realistic study should of course incorporate a more sophisticated modeling of the background. However, since our uncertainties are dominated by the

signal modeling, a more careful accounting of the quark/gluon composition of the background should be a subdominant effect.

2.2.1 $\tilde{\Lambda}$ Dependence

In this section, we explore the dependence on the dark sector confinement scale $\tilde{\Lambda}$. The plots shown in Fig. 3 compare the e_2 distribution for a dark-quark-initiated jet against a QCD-quark-initiated jet for a range of confinement scales $\tilde{\Lambda} \neq \Lambda_{\text{QCD}}$ compared to the QCD quark background, for two choices of β . As the confinement scale increases, the dark sector distribution shifts toward larger values of e_2 . The larger confinement scale implies that the dark sector coupling is larger than the QCD coupling at the energy scale of the jet. This implies that the peak of the differential distribution occurs at a larger value of e_2 , or equivalently, that the resummation approximation $\tilde{\alpha}L^2 \sim 1$ becomes relevant for larger values of e_2 . Therefore, the distribution peaks closer to the kinematic endpoint.

In the bottom row of Fig. 3, we provide the cumulative distribution $\Sigma(x_{\text{cut}})$ for the various choices of $\tilde{\Lambda}$. For $\beta = 2$, the envelope saturates at $x_{\text{cut}} = 10^{-3}$ for large values of $\tilde{\Lambda}$ and shifts toward $x_{\text{cut}} = 10^{-4}$ as $\tilde{\Lambda}$ decreases. The range of this envelope is 0.22 and insensitive to the size of $\tilde{\Lambda}$. Similarly, for $\beta = 0.5$, the envelope saturates at $x_{\text{cut}} = 10^{-2}$. The envelope range increases as $\tilde{\Lambda}$ decreases, from a minimum of 0.26 and a maximum of 0.40.

As Fig. 4 shows, the discriminatory power of a dark sector signal against a QCD background increases as the dark sector's confinement scale $\tilde{\Lambda}$ increases. However, this increased discrimination power saturates for large confinement scales $\tilde{\Lambda} \gtrsim 50 \text{ GeV}$. This saturation is caused by freezing the running coupling at the “non-perturbative scale” $\mu_{\text{NP}} = 7\tilde{\Lambda}$, which we emphasize is a nonphysical prescription designed to obtain

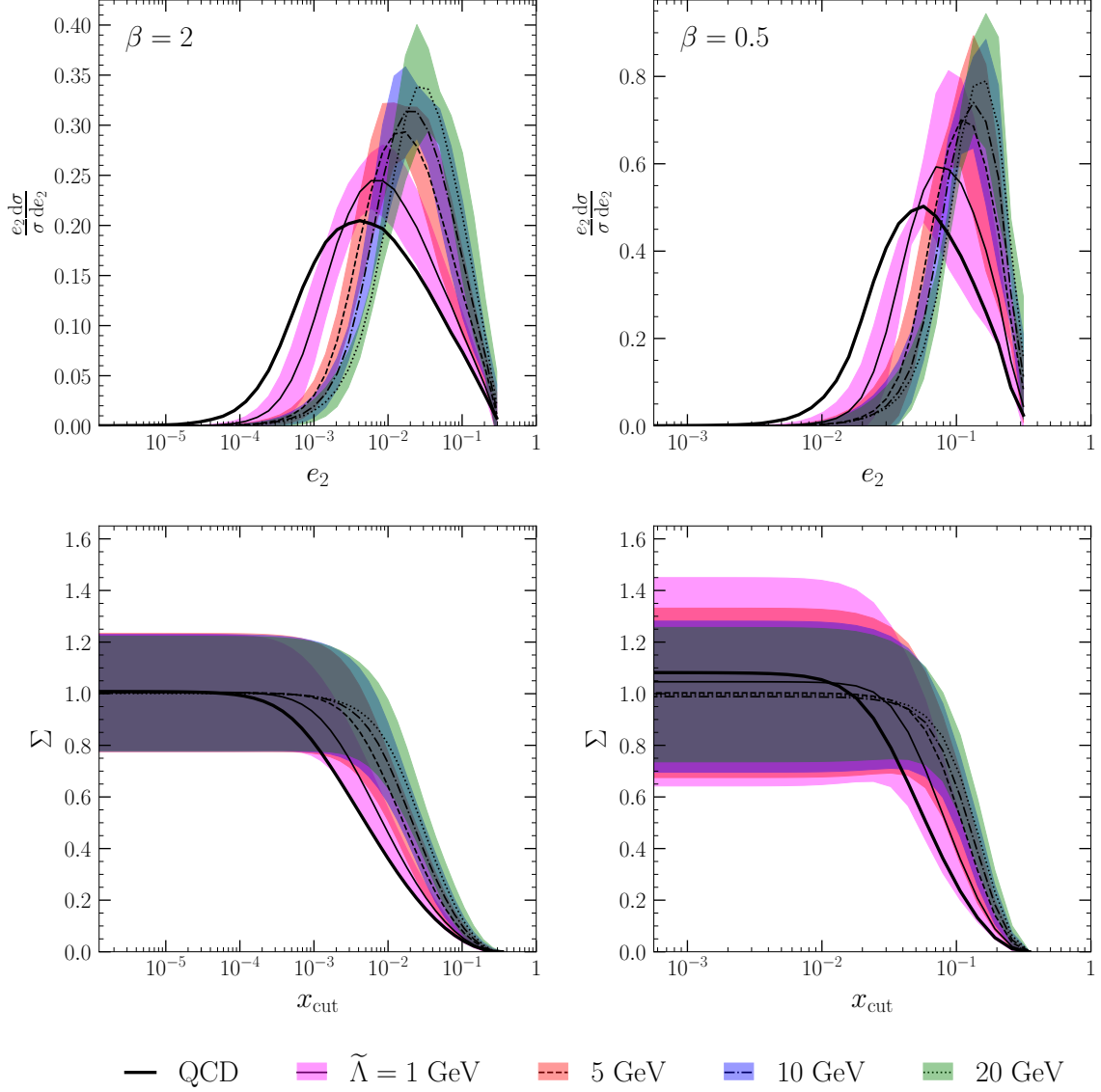


Figure 3. The behavior of e_2 as the dark confinement scale $\tilde{\Lambda}$ is varied, for $p_T = 1$ TeV jets. See the legend for values of $\tilde{\Lambda}$; all other values are given in Table 1. We show the normalized e_2 distributions [top], where the central value of the envelope is marked with the black lines, while the shaded region denotes the envelope. The peak shifts to larger values of e_2 as $\tilde{\Lambda}$ is increased. The cumulant distributions Σ as a function of x_{cut} are also provided [bottom], where again the lines denote the central values and the shaded bands are the integrated envelopes, see Eq. (2.9). We show both results for two choices of the angular dependence: $\beta = 2$ [left] and $\beta = 0.5$ [right].

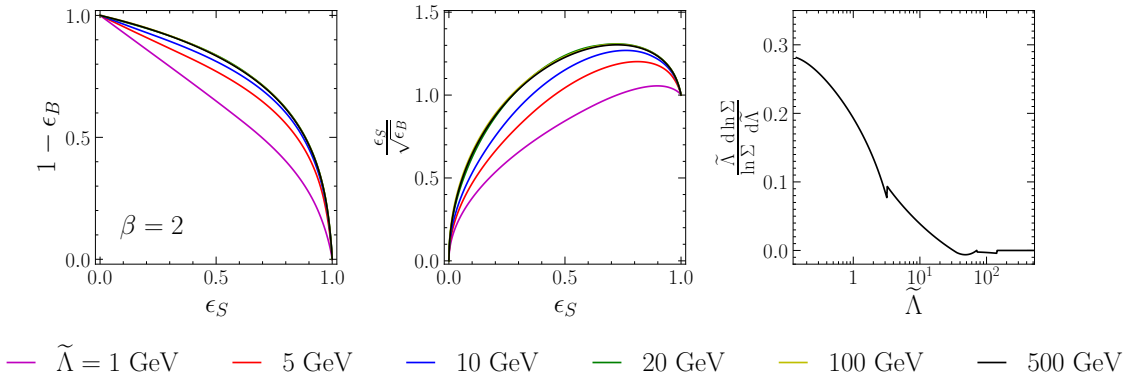


Figure 4. Discrimination of dark sector against QCD for various choices of the confinement scale $\tilde{\Lambda}$ for $p_T = 1$ TeV jets, using the MLL analytic calculation. Note that the impact of errors is ignored here, see Sec. 2.1.4 for details. We show ROC curves in the background rejection $1 - \epsilon_B$ versus signal efficiency ϵ_S plane [left]. We show the curve of discriminatory significance $\epsilon_S/\sqrt{\epsilon_B}$ against signal efficiency ϵ_S [middle]. Fixing the background rejection at 90%, we then show the relative change in discriminatory power as a function of $\tilde{\Lambda}$. The angular dependence parameter is $\beta = 2$ for all panels.

a closed-form solution to (2.7). Using the explicit dependence of μ_{NP} on $\tilde{\Lambda}$, we can derive a naïve small coupling expansion for the discriminator,

$$\frac{\tilde{\Lambda}}{\ln \Sigma} \frac{d \ln \Sigma}{d \tilde{\Lambda}} \simeq \left(\ln \frac{p_T R_0}{\tilde{\Lambda}} \right)^{-1}. \quad (2.10)$$

This provides a reasonable estimate of the scaling until $\tilde{\Lambda} \gtrsim 5$ GeV, when the approximation begins to fail. This can be traced back to the behavior of Eqs. (A.21) to (A.23), from which we infer that as the confinement scale increases, the non-perturbative effects become more relevant for larger values of e_2 .

2.2.2 \tilde{N}_C Dependence

In this section, we explore how the substructure depends on the number of dark colors, \tilde{N}_C . The set of plots shown in Fig. 5 compare the e_2 distribution for a QCD-quark-initiated jet against a dark sector-quark-initiated jet for various choices of the number of dark colors $\tilde{N}_C > 3$. As the number of dark colors increases, the β -function

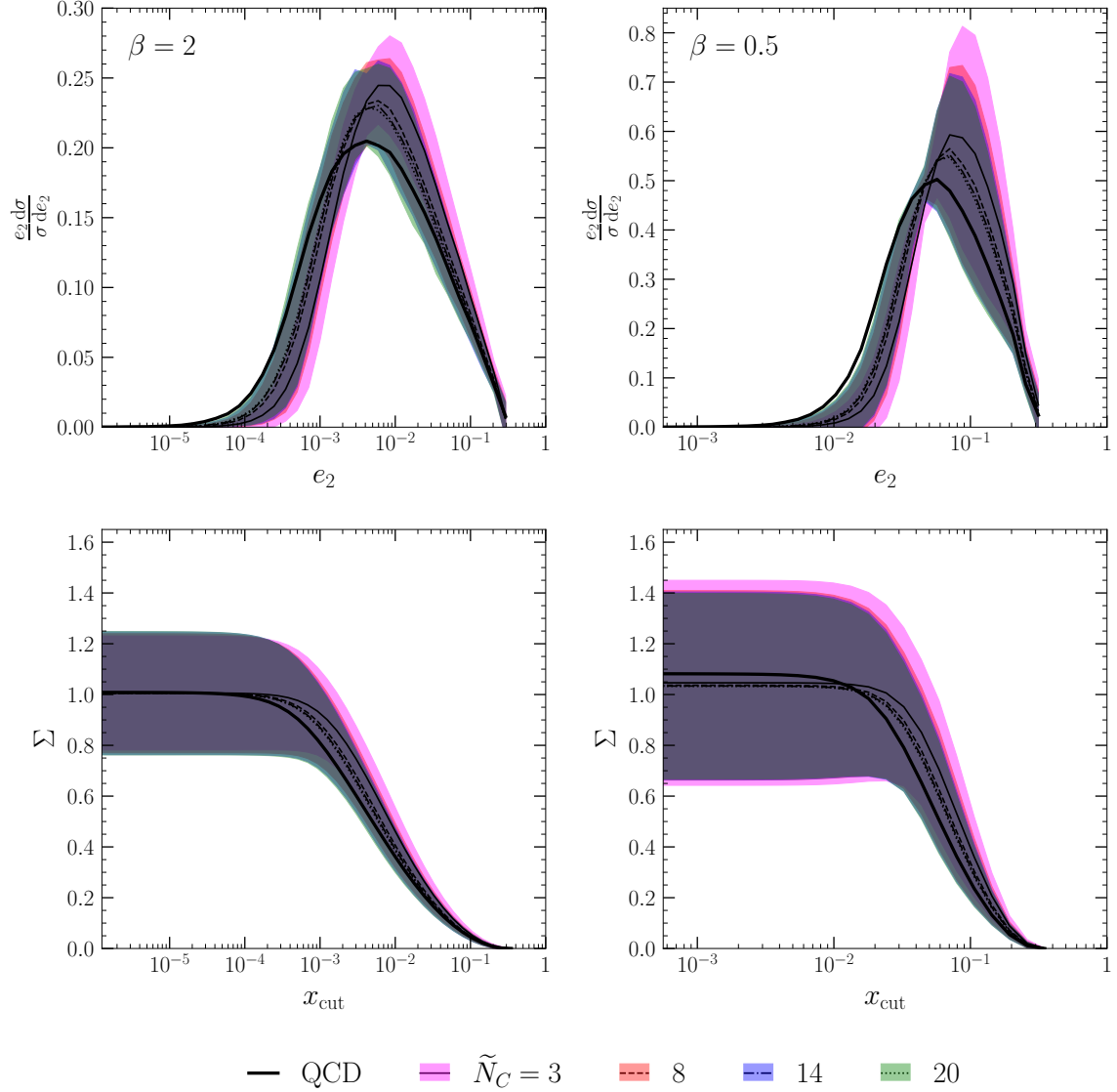


Figure 5. The behavior of e_2 as the dark sector gauge group $SU(\tilde{N}_C)$ is varied, for $p_T = 1$ TeV jets. See the legend for values of \tilde{N}_C ; all other values are given in Table 1. We show the normalized e_2 distributions [top], where the central value of the envelope is marked with the black lines, while the shaded region denotes the envelope. The peak moves to slightly lower values of e_2 as \tilde{N}_C is increased. The cumulant distributions Σ as a function of x_{cut} are also provided [bottom], where again the lines denote the central values and the shaded bands are the integrated envelopes, see Eq. (2.9). We show both results for two choices of the angular dependence: $\beta = 2$ [left] and $\beta = 0.5$ [right].

for the dark sector gauge coupling becomes more negative, so the scale evolution is faster for the dark sector than for the QCD background. This faster running of the

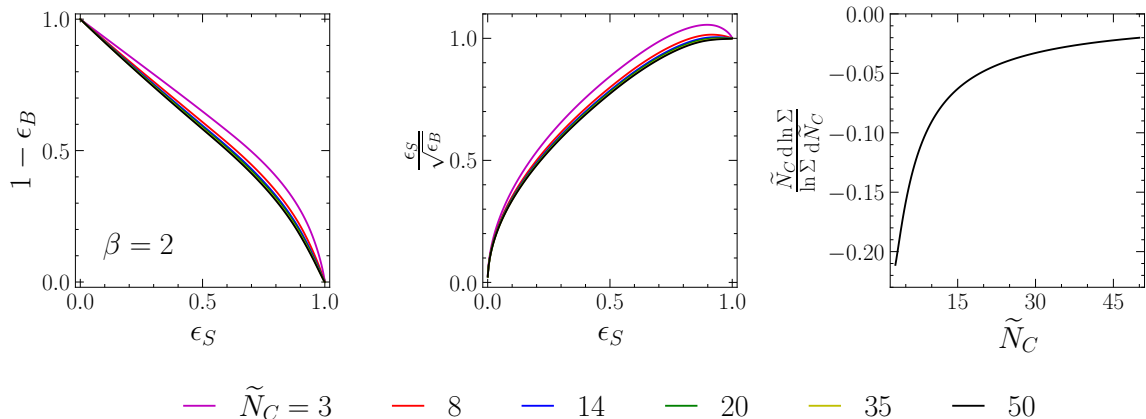


Figure 6. Discrimination of dark sector against QCD for various choices of the number of colors in the dark sector \tilde{N}_C for $p_T = 1$ TeV jets, using the MLL analytic calculation. Note that the impact of errors is ignored here, see Sec. 2.1.4 for details. We show ROC curves in the background rejection $1 - \epsilon_B$ versus signal efficiency ϵ_S plane [left]. We show the curve of discriminatory significance $\epsilon_S/\sqrt{\epsilon_B}$ against signal efficiency ϵ_S [middle]. Fixing the background rejection at 90 %, we then show the relative change in discriminatory power as a function of \tilde{N}_C . The angular dependence parameter is $\beta = 2$ for all panels.

coupling shifts the dark sector distribution toward smaller values of e_2 since $\tilde{\alpha} < \alpha_s$ at the scale set by the jet p_T .

In the bottom row of Fig. 5, we provide the cumulative distribution $\Sigma(x_{\text{cut}})$ for the various choices of \tilde{N}_C . For $\beta = 2$, the envelope saturates at $x_{\text{cut}} = 10^{-4}$, regardless of the value of \tilde{N}_C . The range of this envelope is 0.22 and insensitive to the size of \tilde{N}_C . Similarly, for $\beta = 0.5$, the envelope saturates at $x_{\text{cut}} = 10^{-2}$. The envelope range increases as \tilde{N}_C decreases, from a minimum of 0.36 and a maximum of 0.40.

As Fig. 6 shows, the discriminatory power of a dark sector signal against the QCD background decreases as the dark sector’s number of dark colors \tilde{N}_C increases. However, this decrease is rather marginal, and saturates for $\tilde{N}_C \sim 10$. We can understand this behavior analytically, by expanding the LL resummed cumulative distribution Eq. (A.6) to leading order in $\tilde{\alpha}$. We find that the \tilde{N}_C dependence is well

approximated by

$$\frac{\tilde{N}_C}{\ln \Sigma} \frac{d \ln \Sigma}{d \tilde{N}_C} \simeq \frac{1 + \tilde{N}_C^2}{\tilde{N}_C^2 - 1} + \frac{11 \tilde{N}_C}{4 \tilde{n}_F T_R - 11 \tilde{N}_C}. \quad (2.11)$$

This makes it clear that the discriminator quickly asymptotes as one increases \tilde{N}_C , thereby explaining the qualitative behavior in the figures, i.e., that the sensitivity of the observables studied here to the number of dark colors is minimal.

2.2.3 \tilde{n}_F Dependence

In this section, we explore how the substructure depends on the number of dark flavors \tilde{n}_F . The plots shown in Fig. 7 compare the e_2 distribution for a dark-quark-initiated jet against a QCD-quark-initiated jet for a range of dark flavors with $\tilde{n}_F > 5$; note that we take the number of flavors for QCD to be $n_F = 5$. As the number of dark flavors increases, the β -function for the dark sector coupling $\tilde{\alpha}$ decreases, and in particular the dark sector is no longer asymptotically free when $\tilde{n}_F > \frac{11 \tilde{N}_C}{4 T_R}$. This implies that the renormalization group evolution is slower for the dark sector than for the QCD background. This impacts the dark sector distribution by shifting it towards larger values of e_2 , since $\tilde{\alpha} > \alpha_s$ at the characteristic hard scale of the jet.

In the bottom row of Fig. 7, we provide the cumulative distribution $\Sigma(x_{\text{cut}})$ for the various choices of \tilde{n}_F . For $\beta = 2$, the envelope saturates at $x_{\text{cut}} = 5 \times 10^{-4}$ for large values of \tilde{n}_F and shifts toward $x_{\text{cut}} = 10^{-4}$ as \tilde{n}_F decreases. The range of the envelope is 0.24 and insensitive to the size of \tilde{n}_F . Similarly, for $\beta = 0.5$, the envelope saturates at $x_{\text{cut}} = 10^{-2}$, regardless of the value of \tilde{n}_F . The envelope range increases as \tilde{n}_F increases, from a minimum of 0.34 and a maximum of 0.50. While we are limited by how many flavors we allow the dark sector to have if we want a confining dark sector, the differential distribution shifts toward larger values of e_2 as \tilde{n}_F increases.

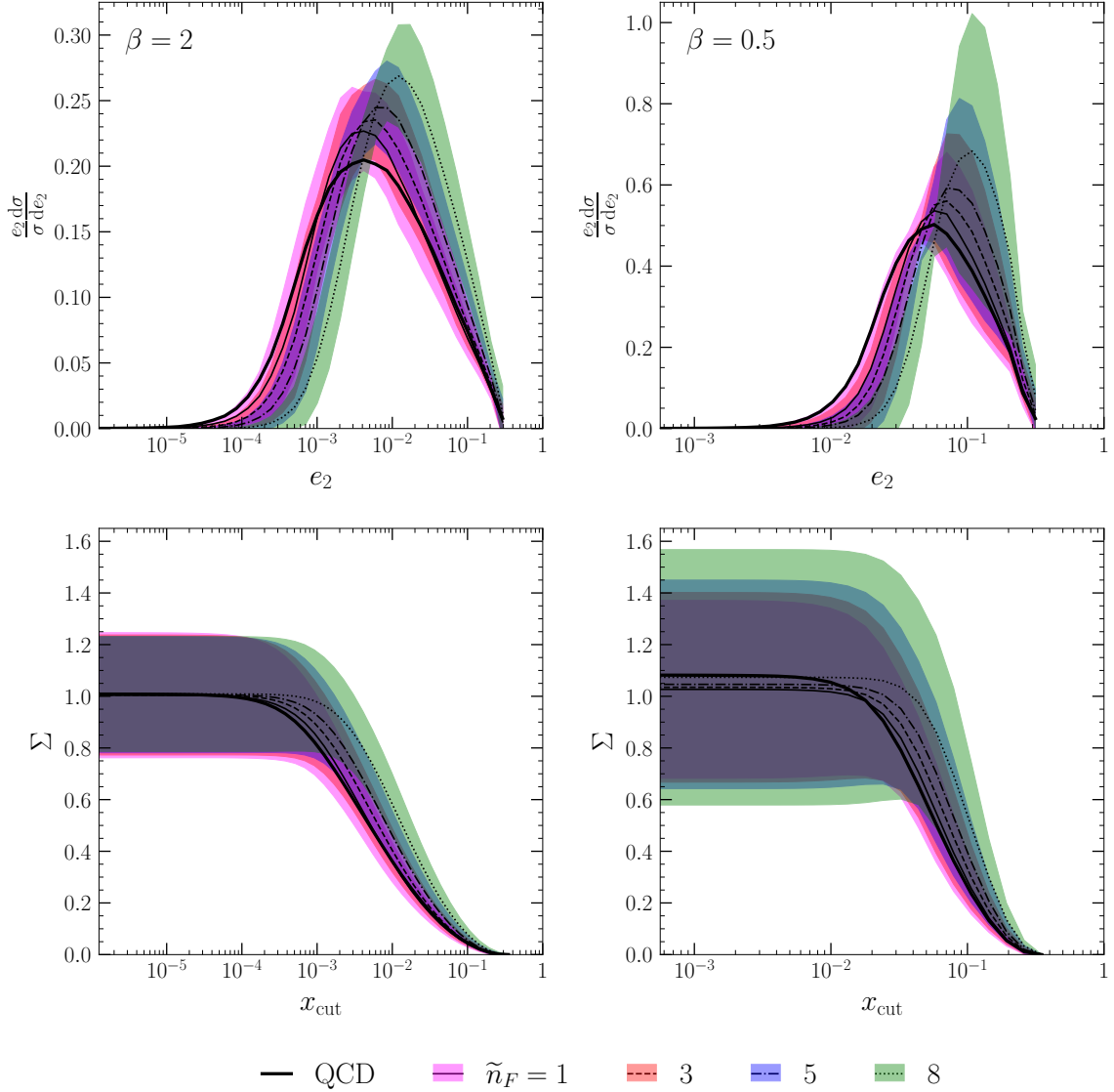


Figure 7. The behavior of e_2 as the number of dark quark flavors \tilde{n}_F is varied, for $p_T = 1$ TeV jets. See the legend for values of \tilde{n}_F ; all other values are given in Table 1. We show the normalized e_2 distributions [top], where the central value of the envelope is marked with the black lines, while the shaded region denotes the envelope. The peak moves to higher values of e_2 as \tilde{N}_C is increased. The cumulant distributions Σ as a function of x_{cut} are also provided [bottom], where again the lines denote the central values and the shaded bands are the integrated envelopes, see Eq. (2.9). We show both results for two choices of the angular dependence: $\beta = 2$ [left] and $\beta = 0.5$ [right].

As Fig. 8 shows, the ability to discriminate a dark sector signal against a QCD background increases as the number of dark flavors increases. Furthermore, this effect

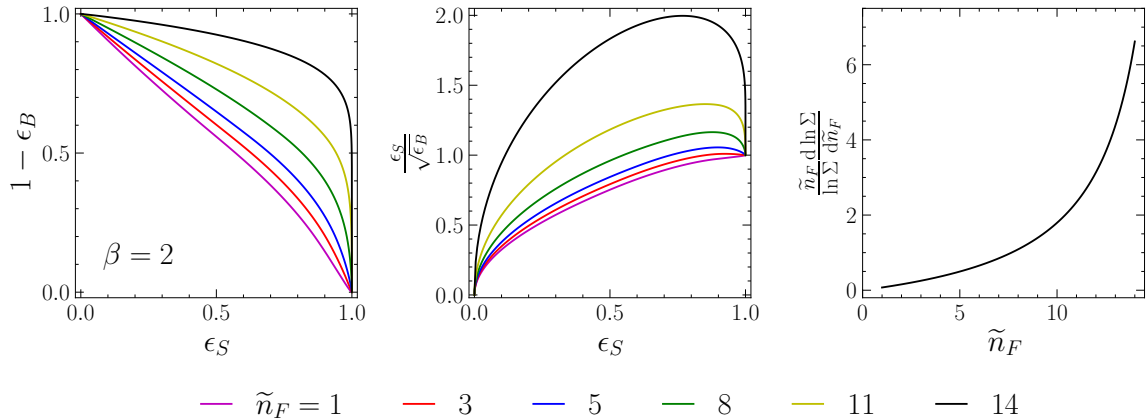


Figure 8. Discrimination of dark sector against QCD for various choices of the number of dark quark flavors \tilde{n}_F for $p_T = 1$ TeV jets, using the MLL analytic calculation. Note that the impact of errors is ignored here, see Sec. 2.1.4 for details. We show ROC curves in the background rejection $1 - \epsilon_B$ versus signal efficiency ϵ_S plane [left]. We show the curve of discriminatory significance $\epsilon_S/\sqrt{\epsilon_B}$ against signal efficiency ϵ_S [middle]. Fixing the background rejection at 90%, we then show the relative change in discriminatory power as a function of \tilde{n}_F . The angular dependence parameter is $\beta = 2$ for all panels.

increases rapidly as \tilde{n}_F^{-1} . The dark flavor dependence can be estimated by expanding the LL resummed cumulative distribution given in Eq. (A.6) to leading order in the coupling. This yields

$$\frac{\tilde{n}_F}{\ln \Sigma} \frac{d \ln \Sigma}{d \tilde{n}_F} \simeq \frac{4\tilde{n}_F T_R}{11\tilde{N}_C - 4\tilde{n}_F T_R}. \quad (2.12)$$

While naively this implies that we should be able to find regions of parameter space that are very non-QCD-like, the framework breaks down for $\tilde{n}_F > \frac{11\tilde{N}_C}{4T_R}$, because the dark sector does not confine as mentioned above. Practically, PYTHIA has limited the number of dark flavors one can include to be eight at most. Therefore, we are not able to numerically probe the discriminator beyond this point in parameter space. However, the trend agrees between the numeric and analytic calculations, and follows the analytic estimate in Eq. (2.12) to a good approximation.

2.2.4 \tilde{m}_q Dependence

Finally, we explore the impact of varying \tilde{m}_q on the e_2 distribution. Since the analytic calculations assume massless partons, we are not in a position to include the analytic contributions to our error envelopes. However, for IRC-safe observables such as $e_2^{(\beta)}$, the mass dependence of our distributions is suppressed as a power of $\tilde{m}_q/\tilde{\Lambda}$ when $\tilde{m}_q \ll \tilde{\Lambda}$, with the resulting effect on our results being negligible. This is not the case when quark masses exceed the confinement scale since \tilde{m}_q then set the scale where the parton shower terminates. In the latter case, an accurate analytic treatment of finite quark masses is challenging, due to the presence of multiple overlapping logarithms of both e_2 and ratios of quark masses and energy scales. As a result, the resummation of differential distributions becomes a more involved procedure, and we will content ourselves with simply providing the results of a numerical study, and will not estimate the error band for different choices of \tilde{m}_q .

With a degenerate spectrum, the impact of finite dark quark masses within PYTHIA is limited at stopping the parton shower from emitting at scales below \tilde{m}_q , since the resulting partons would not be able to subsequently hadronize, and treating the color strings as having massive endpoints in the evolution of the Lund string during the hadronization step. Since gluon splitting to quark pairs is not included, potential finite mass effects due to radiation dead cones around additional massive quarks from $g \rightarrow q\bar{q}$ splitting play no role. Matrix element corrections in emission, which induce additional mass-dependence in analogous QCD showers, are not included.

When the quark masses are above the confinement scale, the hadrons are more akin to quarkonia like the J/ψ or Υ than they are to light mesons like the π or ρ . Hadronization still occurs, since individual dark quarks cannot decay and can

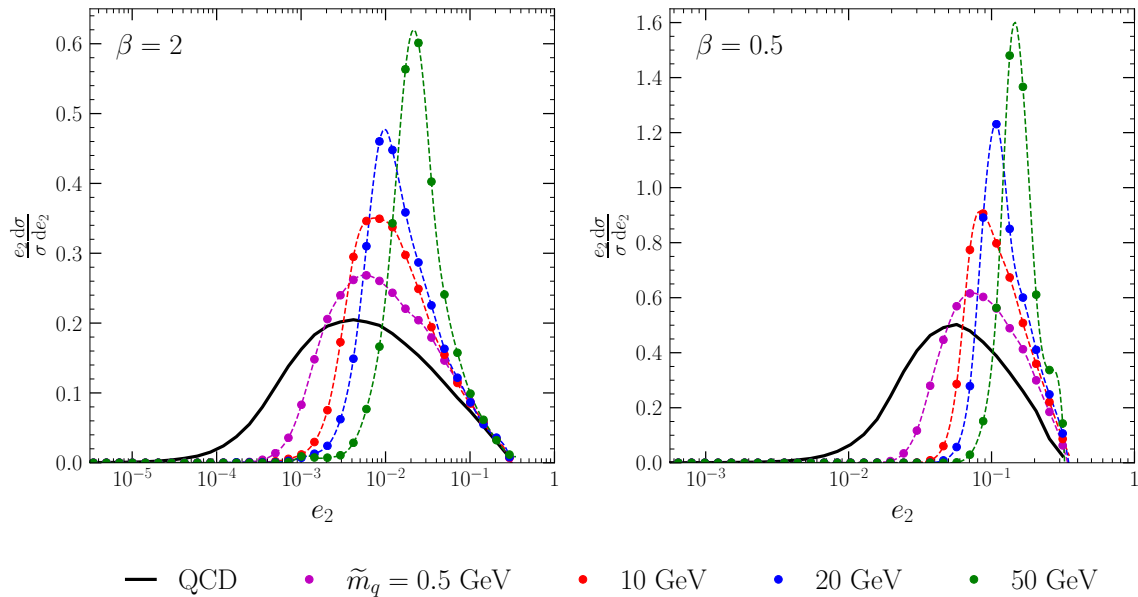


Figure 9. The behavior of e_2 for the dark sector as the degenerate dark quark mass \tilde{m}_q is varied, for $p_T = 1$ TeV jets. The value of \tilde{m}_q is varied according to the legend, while all other values are given in Table 1. The associated dark hadron masses are $2\tilde{m}_q$. Only a numerical study using PYTHIA is presented. We provide a cubic fit to these distributions to guide the eye. Larger dark quark masses move the peak to higher values due to the resulting cutoff imposed on collinear divergences for emissions from massive quarks. We show the results for two choices of the angular dependence: $\beta = 2$ [left] and $\beta = 0.5$ [right].

only annihilate once they become bound into hadrons. While the properties of these states may be well approximated by perturbative methods, as long as the multiplicity of quarkonia produced is larger than a few, a parton shower is still expected to provide a good approximation of the final state.⁹

The result is displayed in Fig. 9, where we compare the e_2 distribution for a quark-initiated QCD jet against the PYTHIA distributions for different choices of the dark quark mass \tilde{m}_q ; we assume that the dark quarks are degenerate and that the dark hadron masses are $2\tilde{m}_q$ for simplicity. The other dark sector parameters are

⁹This approximation will break down as the mass of the dark quarks approaches the energy of the jet such that production of multiple hadrons becomes kinematically disfavored. In this limit, dark glueball production would be expected to result in additional energy missing from the final state. We make no attempt to model this effect.

set to the default given in Table 1. We see that the peak of the distributions moves to higher values of e_2 as \tilde{m}_q is increased. Additionally, we note that the impact on the distributions is not as dramatic as when we varied $\tilde{\Lambda}$ above (*cf.*, Fig. 3). This can be understood due to the fact that increasing the quark masses for fixed gauge coupling simply acts to cut out more of the IR region of the shower phase space where the sector is becoming strongly coupled. While this has an impact on the resultant multiplicity of dark hadrons that are produced in a shower, their subsequent decay from a higher rest mass to nearly massless QCD hadrons obscured the impact of the specific mass scale set by \tilde{m}_q on the observable distribution.

2.3 Quantifying Hadronization Uncertainties

The enveloping procedure includes variations among predictions that result from either an analytic or a numerical approach to capture the dominant IR logs that result from showering. When considering sources of systematic uncertainties, it is critical to investigate the irreducible error on predictions due to incalculable strong coupling effects. Specifically, the numerical results rely on a phenomenological model of hadronization. In the case of PYTHIA, the hadronization step uses the Lund string model [78], which models the physics of confinement by iteratively connecting partons to each other with color strings, and breaking these strings by pair producing quarks from the vacuum when energetically favorable until an equilibrium configuration is achieved.¹⁰ This approach introduces incalculable parameters, which can be tuned to data in the case of real QCD, but must simply be set by hand for the dark sector. It is therefore critical to our goals here to include the uncertainty associated with these choices. As we will show here, hadronization systematics are of the same size as

¹⁰Another commonly used Monte Carlo shower program is HERWIG [121], which uses the cluster hadronization model.

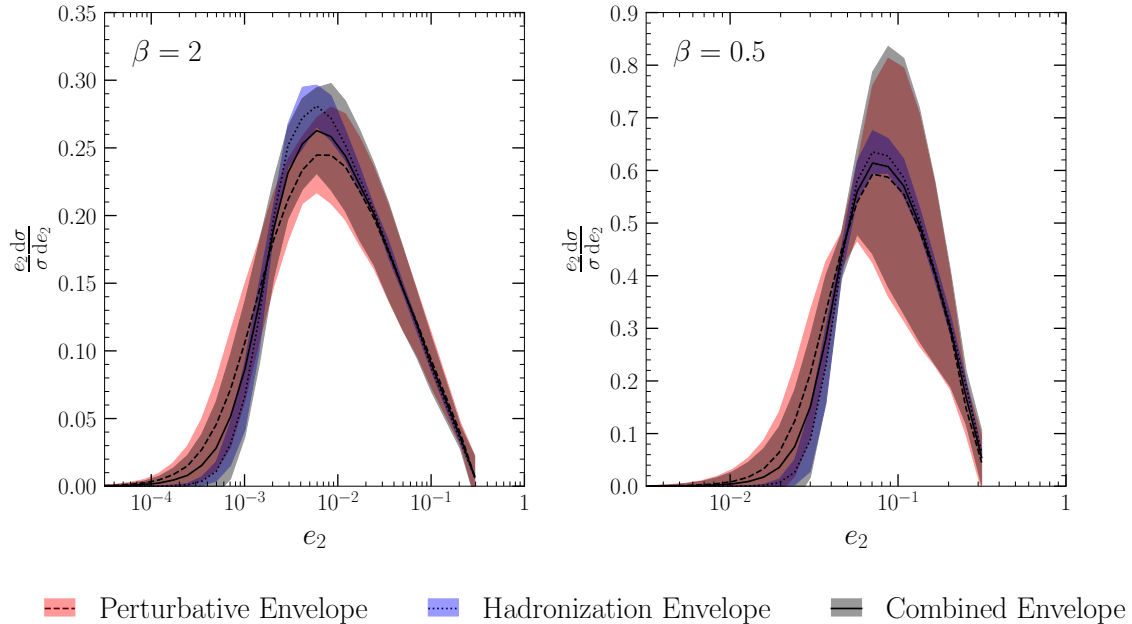


Figure 10. Total theory uncertainties on the e_2 distributions for $p_T = 1$ TeV jets for a dark sector whose model parameters are set to the benchmark values given in Table 1 due to both perturbative and hadronization effects. Perturbative uncertainties are largest around the peak region, dominating at larger e_2 values. Hadronization uncertainties contribute most noticeably starting from the peak and extend down to smaller values of e_2 . Results are presented for two choices of the angular dependence: $\beta = 2$ [left] and $\beta = 0.5$ [right].

the perturbative ones included in the error envelopes thus far. Clearly, they should additionally be included for searches performed by the experimental collaborations.

The results of varying the hadronization parameters is given in Fig. 10, where all other dark sector model parameters are set to the benchmark values given in Table 1. We then explored the hadronization parameter space to find a choice that resulted in the least (most) number of dark hadrons, which corresponds to the parameter choices $\text{aLund} = 0$, $\text{bmqv2} = 2$, and $\text{rFactqv} = 0$ ($\text{aLund} = 2$, $\text{bmqv2} = 0.2$, and $\text{rFactqv} = 2$). The hadronization band in Fig. 10 is then computed by taking the envelope across the result of the default hadronization parameters and these two extreme choices. For reference, we also plot the perturbative prediction, and provide the error envelope as computed above with default hadronization parameters, and we also show the

combination of the two envelopes by adding them in quadrature. The largest impact is that the peak of these distributions do shift; this is expected since the position of the turn over is not under robust theoretical control. We see that the variation from hadronization is of the same order as the perturbative uncertainty.¹¹ We will use the total envelope in the next section where we estimate the impact of non-trivial error envelopes on a mock search for dark sector substructure.

2.4 Discovering Dark Substructure

Having quantified the perturbative and hadronization theory errors on the prediction for substructure that results from dark sector showering, we will briefly turn to estimating the impact of including our error envelopes for a search. Our goal here is to simply estimate the discovery potential. Unsurprisingly given existing limits, the subtle nature of the signature and the overwhelming size of the QCD background will imply that additional handles are required to reduce the background by a factor of $O(10^5)$ if there is any hope of seeing evidence for dark substructure signals. For example, in models where some of the dark hadrons are stable, a cut on missing energy could play this role. In this case, ignoring the effect of jet to jet fluctuations in the number of unstable mesons, the predictions made above are unchanged, except that the statistics are reduced due to the fact that some particles are missing. We expect the associated theory uncertainty to be a subleading effect.

One important mitigating factor is that stringent limits on new physics contributions to QCD distributions already exist from ATLAS [122] and CMS [123]. Since these searches simply look for high p_T jets in the final state, the dark jets would fall in the signal region with essentially equal efficiency to QCD jets. Therefore, our

¹¹We caution that other observables could be even more sensitive to the details of hadronization, especially those that rely on shape aspects of the substructure.

first step to quantifying the discovery reach for models that yield substructure from dark showers is to interpret these bounds as a limit on the dark quark production cross section.

We assume the portal to the dark sector can be modeled by a contact interaction:

$$\mathcal{L}_{\text{int}} \supset \frac{1}{\Lambda_{\text{CI}}^2} (\bar{q} \gamma^\mu q) (\tilde{q} \gamma_\mu \tilde{q}). \quad (2.13)$$

By hunting for deviations in the tails of jet distributions, ATLAS [122] and CMS [123] have derived comparable limits $\Lambda_{\text{CI}} \gtrsim 22 \text{ TeV}$. We emphasize that this limit is essentially unchanged for our model, since the searches do not make any cuts on substructure.

We convert this limit on the new physics scale into a bound on the production cross section using an implementation of a $B-L$ extension of the Standard Model [124, 125] publicly available in the FEYNRULES [126] model database. We take the Z' mass to be large so that the production process $\bar{q}q \rightarrow Z' \rightarrow \tilde{q}\tilde{q}$ is well approximated by Eq. (2.13). Events are simulated using MADGRAPH5_AMC@NLO [127], taking the model parameters to correspond to the lower bound on Λ_{CI} . This allows us to compute the cross section for $pp \rightarrow \bar{q}q$, and we then simply interpret the result as the rate for dark quark production. We implement generator level cuts on rapidity $\eta < 2$ and transverse jet momentum $p_T > 1 \text{ TeV}$. Our dijet background is produced by all $2 \rightarrow 2$ QCD processes applying the same cuts. This results in a signal cross section $\sigma_S = 5 \times 10^{-5} \text{ pb}$, which can be compared to the enormous QCD background $\sigma_B = 13 \text{ pb}$.¹² These cross sections are used to compute the expected number of events for two choices of integrated luminosity; the final Run III data set of 300 fb^{-1} and the

¹²Since this is meant to be a simple estimate, we do not include a K -factor, which at NNLO is in the range $1.3 - 1.5$ [128].

complete high luminosity data set of 3000 fb^{-1} . These values should be interpreted as the number of events that survive a loose “pre-selection” for the search.

Next we approximate the discovery significance including the impact of both statistical and systematic uncertainties using

$$\mathcal{Z} = \frac{S}{\sqrt{S + B + \delta_S^2 S^2 + \delta_B^2 B^2}}, \quad (2.14)$$

where S is the number of signal events, B is the number of background events, and δ_i are their respective systematic uncertainties. Given the already stringent limits on the production of the dark quarks, it is easy to check that using dark substructure alone will not provide enough discriminating power to beat down the QCD background. Therefore, we will reframe the question in terms of a background reduction factor ϵ , which provides an estimate of what one must be able to achieve by incorporating other handles into the search, e.g. missing energy, resonances, and/or displaced objects.¹³ To compute ϵ , we solve Eq. (2.14) using the substitution $B \rightarrow \epsilon B$:

$$\epsilon = \frac{\sqrt{1 - 4\delta_B^2 S(1 + (\delta_S^2 - \frac{1}{Z^2})S)} - 1}{2\delta_B^2 B}. \quad (2.15)$$

Larger values of ϵ correspond to improved discrimination.

First, we estimate how large ϵ would need to be in order to see a 2σ excess of signal events *without* a cut on substructure and assuming no uncertainty on the signal production rate and assuming the cut has no impact on signal statistics, see the left panel of Fig. 11. This provides a baseline against which we can compare how much improvement can be obtained using substructure. Next, we include the

¹³These changes to the model would obviously also impact the limits on signal production rates, i.e., the limit on Λ_{CI} in Eq. (2.13).

substructure cut, using the models with varying $\tilde{\Lambda}$ as a concrete example. We assume the theory error bands on the dark sector distributions are fully correlated, just as we did above when computing the cumulative distributions, e.g. Fig. 3. For the QCD background, there is a wealth of data that is used for tuning and calibration, and as such the systematic error bars can be controlled by leveraging a variety of inputs. For the results presented in Fig. 11, we use the background uncertainty $\delta_B = 0.1$ as determined by a recent NNLO calculation [128]. We additionally assume that δ_B does not depend on the substructure cut. As a point of comparison, data driven approaches currently yield $\delta_B \sim 20\%$ [122].

In Fig. 11, we plot the background rejection factor required to achieve a 2σ exclusion as a function of the dark confinement scale $\tilde{\Lambda}$, by optimizing a substructure cut for each choice of model parameters. In order to explore the impact of the error envelopes, we provide the result with $\delta_S = 0$ in black and $\delta_S \neq 0$ in red, and we also provide the results for $\beta = 2$ and 0.5 to investigate varying the angular dependence parameter. We assume either 300 fb^{-1} or 3000 fb^{-1} of integrated luminosity, which allows us to explore the scaling as the data set size is increased.¹⁴

Most importantly, we see that a cut on substructure improves one's ability to discover these models, even when the systematic error on the signal shape is included. In particular, taking $\beta = 2$ and $\tilde{\Lambda} = 20 \text{ GeV}$ the relative change $\Delta\epsilon = 0.9(0.6)$ for no error (with error) for 300 fb^{-1} ; the relative change for 3000 fb^{-1} $\Delta\epsilon = 1.5(1.4)$ for no error (with error).¹⁵ This motivates future work quantifying the error envelopes

¹⁴It is worth noting that the bound on the scale for the contact operator Λ_{CI} will also improve with more data, which is not being taken into account here.

¹⁵Note that we have not included the constraint on the error of the integrated resummed cross section given by the inclusive calculation. This is the cause of the unphysical value for the background reduction factor for $\tilde{\Lambda} = 1 \text{ GeV}$ and $\beta = 0.5$. This only becomes a significant effect when the additional sensitivity gained from substructure discriminants becomes small.

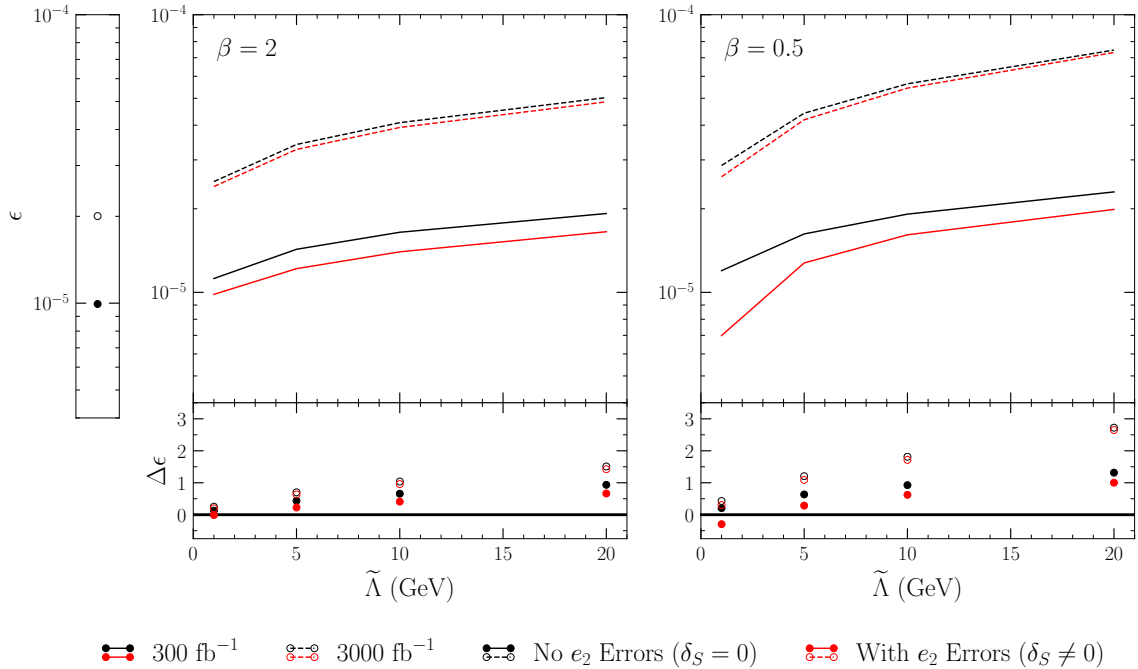


Figure 11. The background reduction factor (see Eq. (2.15)) required to observe new physics over the QCD background for $p_T = 1$ TeV jets. We show the value required if there are no additional cuts made on jet substructure (assuming $\delta_S = 0$) [left]. Then we provide the results as a function of $\tilde{\Lambda}$ taking $\beta = 2$ [middle] and $\beta = 0.5$ [right]. The resulting reduction in the needed ϵ as a result of the substructure cut is presented as a multiplicative factor below the middle and right plots. We vary the luminosity and provide results with and without errors, see the legend for details.

for a wider variety of substructure distributions that could result from dark sector showers, so that cuts on these variables can be properly incorporated into searches. In particular, it is important to include such systematics when deriving limits on signal parameter space, since the non-trivial error bands can result in more realistic exclusion regions. Finally, we note that for the 300 fb^{-1} data set, the optimized value of the cut yields a signal region that is statistics dominated. Then when we increase the data set size to 3000 fb^{-1} , we find that optimal signal region has comparable statistical and systematic errors. We conclude that this subtle signature of dark sector physics is an interesting target scenario for the physics program at the high luminosity LHC.

CHAPTER III

UNITARITY BOUNDS ON EFFECTIVE FIELD THEORIES

Given the extensive literature on the subject of EFT validity, we will put our work in context in Sec. 3.1. In Sec. 3.2, we discuss tree-level toy model UV completions of the benchmark pair production in Eq. (3.1), which are characterized by the exchange of a heavy BSM scalar of mass M in the s -channel or t -channel. For each case, we match to the corresponding EFT descriptions. In Sec. 3.3, we study perturbative partial-wave unitarity and show how to incorporate PDFs into this necessary test of EFT validity. We show that low-order EFTs can still be free of perturbative unitarity violation, even when the mass M of the new physics state being integrated out is significantly below the hadronic collision energy. In Sec. 3.4, we compare the pair production cross sections predicted by the EFTs against the predictions of the UV theories. This will provide us with a way to quantitatively understand the implications of the perturbative unitarity bound that are appropriate for hadronic initial states. In Sec. 3.5, we vary the PDF integration limits, which allows us to explore the impact on our results as the search design becomes less inclusive. App. B provides some results for the parameter space with a smaller mass for the final state particles.

3.1 Strategies for Assessing EFT Validity

In this section, we will briefly discuss the extensive related literature, which will allow us to put the present work in context. The subject of EFT validity is as old as the idea itself. As the framework was being developed and its renormalization properties were being understood, e.g. in the context of condensed matter systems [129, 130, 131] and gauge theories [132], it was always appreciated that the EFT was only meant to be applied in a limited low energy regime. This

question took on a renewed urgency in the modern era, as EFTs were being utilized as a way to design searches for new physics at the LHC, e.g. in the context of directly producing dark matter [66, 67, 68, 69, 70, 71, 72, 73, 133, 134, 135, 136, 137, 138, 139, 140, 141, 142, 143, 144, 145, 146, 147, 148, 149, 150, 151, 152, 153, 154], or looking for the imprint of the Standard Model EFT (SMEFT) itself [155, 156, 157, 158, 159, 160, 161, 162, 163, 164, 165, 166, 167, 168, 169, 170, 171, 172, 173, 174, 175, 176, 177, 178, 179, 180, 181, 182, 183, 184, 185, 186, 187, 188, 189, 190, 191, 192, 193, 194, 195, 196, 197, 198, 199, 200, 201, 202, 203, 204, 205]. Many of these analyses explored parameter space with $M < \sqrt{s}$, prompting a variety of studies to assess the validity of the EFT description and to propose modifications to make it more robust [206, 207, 208, 209, 210, 211, 212, 213, 214, 215, 216, 217, 218]. Conversely, many groups advocated to abandon the EFT approach all together in favor of Simplified Model descriptions that were clearly well defined [219, 220, 221, 222, 223, 224, 225, 226, 227, 228, 229, 230, 231, 232, 233, 234, 235, 236, 237, 238, 239, 240, 241, 242, 243, 244, 245, 246, 247, 248, 249, 250, 251, 252].

The issues addressed by these authors essentially stem from two concerns. The first is that when $M < \sqrt{s}$, one would expect to be able to produce the associated mediator particle directly, since it is the mediator’s mass that sets the scale M . This opens up new and often more powerful ways to search for the signatures of the associated model. We have nothing novel to say about this important effect. However, we remind the reader that in the narrow width approximation, the production of the heavy on-shell states would not interfere with the processes captured by the EFT. Therefore, including these additional direct mediator production processes would lead to a stronger limit, in principle, than what one would obtain by using the EFT alone. Since the EFT limit does not require specifying a concrete UV completion, it can be

applied to a broader class of models without a dedicated recasting effort. For these reasons, we advocate that EFT searches are still useful in their own right, although care must be taken with regards to their interpretation.

The second concern is of direct relevance to the study we perform here. Recognizing that $\sqrt{\hat{s}}$ is the quantity of interest when testing for EFT validity, a variety of proposals were put forward that shared a theme of “cutting away high energy events.” In other words, the kinematics were restricted so as to avoid the region of phase space where the EFT validity was in question.

For example, the authors of [213] proposed to cut away any event with $\sqrt{\hat{s}} > M$ (at simulation truth level) when computing the signal rates. Incorporating a maximum allowed value of $\sqrt{\hat{s}}$ within the signal simulation ensures the validity of the EFT, at the expense of reducing the EFT prediction significantly. One could even consider the cut on maximum allowed $\sqrt{\hat{s}}$ as an additional parameter of the signal model. One could vary this additional parameter to see how sensitive a given search is to such high energy events.¹ Although the limits derived with this approach are strictly valid, the resulting bounds on M can be artificially conservative.

Another group [207, 209, 210], proposed to cut on the observable kinematics of the final state as a proxy for removing high energy events. In the same spirit, experimentalists have applied a high energy cut parameter to some of their EFT analyses, investigating the robustness of the limits they derive when this parameter is varied [66, 67, 68, 69, 70, 71, 72, 73, 253]. An alternative strategy to “unitarize” the EFT has also been employed in some experimental searches [254, 255]. Note that essentially all previous validity studies are truncated at the leading order EFT dimension; see [211] for a notable exception.

¹We thank Markus Luty for emphasizing this point of view to us.

Our focus here is on exploring the impact of PDFs on the perturbative partial-wave unitarity bound. We emphasize that while perturbative partial-wave unitarity provides a good proxy for the question of EFT validity, satisfying this condition is necessary but not sufficient. The key insight of this work is to leverage the fact that a typical signal region includes events with a range of associated $\sqrt{\hat{s}}$. Therefore, one must incorporate an ensemble of events when diagnosing EFT validity — when working at a hadron collider, this can be accounted for by properly treating PDF effects. We will show that (for sufficiently inclusive signal regions) perturbative unitarity bounds on EFTs are typically insensitive to cutting away high energy events (when the cut is applied to both signal and background), which we take to be a sign that the EFT validity is being saved by the PDF suppression at high momentum fraction. One of the goals of this work is to make this intuition precise.

3.2 Benchmark Process and Toy Models

As we emphasized above, our goal is to study the impact of having an ensemble of events with various values of $\sqrt{\hat{s}}$ on the question of EFT validity. To this end, we will focus our attention on the benchmark pair production process

$$(pp \rightarrow \phi\phi^\dagger) = \sum_{\{q, \bar{q}\} \in p} (\phi_q \phi_q^\dagger \rightarrow \phi\phi^\dagger). \quad (3.1)$$

For simplicity, we will study this question using two simple toy model UV theories. At tree level, these models are characterized by how they generate the benchmark pair production by either the t -channel or s -channel exchange of a heavy BSM scalar, as illustrated in Figs. 12 and 13, respectively. We will then match these theories onto the subset of EFT operators that contribute to Eq. (3.1) at tree-level.

Note that to minimize the technical aspects of what follows, we have chosen to work with scalar “quarks” ϕ_q, ϕ_q^\dagger in the initial state (not to be confused with “squarks” in supersymmetric theories). Specifically, we will be using the q, \bar{q} quark PDFs when investigating the interpretation of the EFT parameter space. This has the benefit that the analytic formulas will be very simple, at the obvious expense of not being fully realistic.²

We will make an additional simplifying choice in what follows. When we integrate out a heavy state, the leading order contribution to the EFT Lagrangian appears at dimension 4, since we are working with pure scalar toy theories. Note that the operators of interest here are those that lead to cross section growth, which have dimension > 4 . Therefore, we will tune a Lagrangian quartic parameter against the EFT contribution so that the leading contribution to the 2-to-2 scattering of interest comes from a dimension 6 operator. This makes our results much more intuitive, and also more relevant to the realistic case where the quarks (and perhaps also the final state particles) are fermions.

The final state ϕ is a (relatively light) BSM scalar. It could be a dark matter candidate, some other BSM state, or even an Standard Model particle (as it would be in the case of SMEFT searches); all that matters in what follows is that it is a scalar, and otherwise we are agnostic about its identity. The only EFT operators that contribute to the benchmark pair production process in Eq. (3.1) are those involving extra derivatives with a fixed number of fields (leading to a $1/M$ expansion). We will briefly comment on the relation to the EFT operators that involve more powers of fields (leading to a $1/\Lambda$ expansion) in Sec. 3.2.3.

²We will perform the analysis for fermionic initial and final states in a future paper. We also anticipate that we will find similar conclusions if the production process is dominated by a gluon or mixed quark/gluon initial state, which we also plan to study in a future paper.

3.2.1 t -Channel Model

A model that results in t -channel pair production utilizes a heavy complex scalar mediator Φ that couples to the scalar quarks ϕ_q and the BSM singlet scalar ϕ through a tri-linear interaction:

$$\begin{aligned} \mathcal{L}_{t,\text{UV}} \supset \mathcal{L}_{\text{SM}} - \phi^\dagger (\partial^2 + m_\phi^2) \phi - \lambda_{q\phi} (\phi_q^\dagger \phi) (\phi^\dagger \phi_q) \\ - \Phi^\dagger (D^2 + M^2) \Phi - \mu_{q\phi} \phi_q^\dagger \phi \Phi - \mu_{q\phi}^* \Phi^\dagger \phi^\dagger \phi_q, \end{aligned} \quad (3.2)$$

where \mathcal{L}_{SM} is the Standard Model Lagrangian (including the kinetic term for the scalar quarks), D_μ is a gauge covariant derivative, m_ϕ is the mass of the BSM singlet scalars, $\lambda_{q\phi}$ is a cross quartic coupling, M is the mass of the heavy scalar mediator Φ , and $\mu_{q\phi}$ is a tri-linear coupling. Since ϕ is a Standard Model singlet, the heavy complex scalar Φ needs to have the same Standard Model charge as the scalar quark ϕ_q to ensure that the tri-linear coupling is gauge invariant. For concreteness, we will assume a universal coupling to the ϕ_q with $q \in \{d_R, s_R, b_R\}$. This choice has a minimal impact on our conclusions.

As depicted in Fig. 12, the EFT description for the t -channel pair production process can be obtained by expanding the propagator:

$$\frac{1}{\hat{t} - M^2} \rightarrow -\frac{1}{M^2} \sum_{r=0}^k \left(\frac{\hat{t}}{M^2} \right)^r, \quad (3.3)$$

where k corresponds to the desired EFT truncation order. Using the 2-to-2 kinematic constraints, we have

$$\hat{t} = (p_1 - p_3)^2 = (p_2 - p_4)^2, \quad (3.4)$$

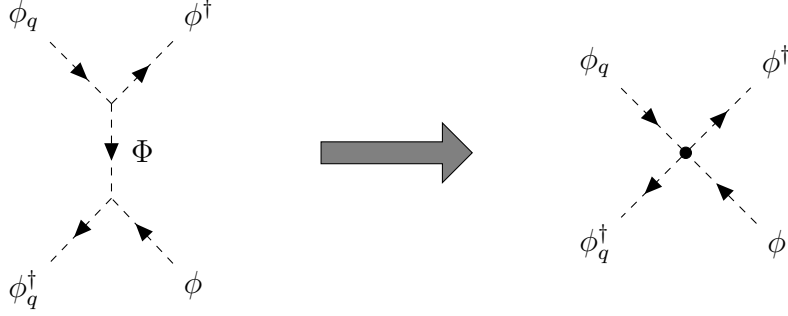


Figure 12. Pair production $\phi_q \phi_q^\dagger \rightarrow \phi \phi^\dagger$ through the t -channel exchange of a heavy complex scalar Φ . The EFT description can be obtained by expanding and truncating the t -channel propagator, yielding a series of local operators.

which implies that the relevant part of the EFT Lagrangian is given by

$$\begin{aligned}
 \mathcal{L}_{t, \text{EFT}} &\supset \mathcal{L}_{\text{SM}} - \phi^\dagger (\partial^2 + m_\phi^2) \phi - \lambda_{q\phi} (\phi_q^\dagger \phi) (\phi^\dagger \phi_q) + \frac{|\mu_{q\phi}|^2}{M^2} \sum_{r=0}^{k+1} (\phi_q^\dagger \phi) \left(-\frac{\partial^2}{M^2} \right)^r (\phi^\dagger \phi_q) \\
 &= \mathcal{L}_{\text{SM}} - \phi^\dagger (\partial^2 + m_\phi^2) \phi - \frac{\lambda_{q\phi}}{M^2} \sum_{r=0}^k (\phi_q^\dagger \phi) \left(-\frac{\partial^2}{M^2} \right)^r \partial^2 (\phi^\dagger \phi_q). \tag{3.5}
 \end{aligned}$$

In the second line, we have set

$$\lambda_{q\phi} = \frac{|\mu_{q\phi}|^2}{M^2}, \tag{3.6}$$

in order to tune away the dimension-4 contribution, and have relabeled the summation index r .³

The maximum dimension of the EFT operators Δ is related to the truncation order k :

$$\Delta = 6 + 2k. \tag{3.7}$$

³Note that the ∂^2 in this EFT Lagrangian should technically be promoted to D^2 to form gauge-invariant effective operators. However, the extra terms that result contain additional gauge bosons and hence do not contribute to $\phi_q \phi_q^\dagger \rightarrow \phi \phi^\dagger$ at tree level, and so we do not include them here.

At the lowest truncation order $k = 0$, our pair production process is modeled by the dimension-six operator

$$\mathcal{O}_6 = -\frac{\lambda_{q\phi}}{M^2} (\phi_q^\dagger \phi) \partial^2 (\phi^\dagger \phi_q) = -\frac{1}{\Lambda^2} (\phi_q^\dagger \phi) \partial^2 (\phi^\dagger \phi_q) . \quad (3.8)$$

The contribution from EFT operators are often said to be characterized by the scale $\Lambda \equiv M/\sqrt{\lambda_{q\phi}}$, which could be much higher than the mediator mass M in the weakly coupled limit $\lambda_{q\phi} \ll 1$. However, note that the contribution from higher orders in the EFT expansion for the 2-to-2 process of interest here is actually controlled by the suppression factor E^2/M^2 as opposed to E^2/Λ^2 , see Eq. (3.5). This distinction is important for interpreting analyses that go beyond dimension-6, see the discussion in Sec. 3.2.3 below.

3.2.2 s -Channel Model

Next, we can write down a model that will yield s -channel production of a pair of BSM singlet scalars ϕ . This can be accomplished by introducing a heavy real singlet scalar mediator S that couples to the scalar quarks $\phi_{q_i}^\dagger \phi_{q_i}$ and to $\phi^\dagger \phi$:

$$\begin{aligned} \mathcal{L}_{s, \text{UV}} \supset \mathcal{L}_{\text{SM}} - \phi^\dagger (\partial^2 + m_\phi^2) \phi - \lambda_q (\phi_{q_i}^\dagger \phi_{q_i}) (\phi^\dagger \phi) \\ - \frac{1}{2} S (\partial^2 + M^2) S - \mu_q \phi_{q_i}^\dagger \phi_{q_i} S - \mu_\phi \phi^\dagger \phi S , \end{aligned} \quad (3.9)$$

where \mathcal{L}_{SM} is the Standard Model Lagrangian, m_ϕ is the mass of the BSM singlet scalars, λ_q is a cross quartic coupling, M is the mass of the heavy scalar mediator S , μ_q and μ_ϕ are tri-linear couplings, and we interpret $\phi_{q_i}^\dagger \phi_{q_i}$ as the sum over all species and flavors of quarks in the Standard Model. Note that we have only included the leading interactions that are relevant for our purposes here, see Sec. 3.2.3 below for a related discussion.

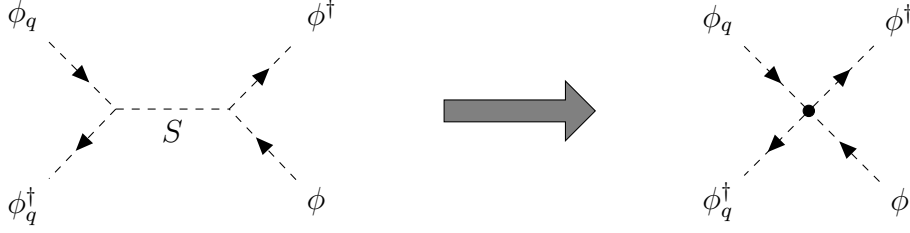


Figure 13. Pair production $\phi_q \phi_q^\dagger \rightarrow \phi \phi^\dagger$ through the s -channel exchange of a heavy singlet scalar S . The EFT description can be obtained by expanding and truncating the s -channel propagator, yielding a series of local operators.

As depicted in Fig. 13, the EFT description for the tree-level s -channel pair production can be obtained by expanding and truncating the propagator:

$$\frac{1}{\hat{s} - M^2} \rightarrow -\frac{1}{M^2} \sum_{r=0}^k \left(\frac{\hat{s}}{M^2} \right)^r, \quad (3.10)$$

where we are introducing the parameter k as in Sec. 3.2.1 above, and we have set the width of S to zero. Since

$$\hat{s} = (p_1 + p_2)^2 = (p_3 + p_4)^2, \quad (3.11)$$

for 2-to-2 kinematics, we infer that the EFT Lagrangian is given by

$$\begin{aligned} \mathcal{L}_{s,\text{EFT}} &\supset \mathcal{L}_{\text{SM}} - \phi^\dagger (\partial^2 + m_\phi^2) \phi - \lambda_q (\phi_{q_i}^\dagger \phi_{q_i}) (\phi^\dagger \phi) + \frac{\mu_q \mu_\phi}{M^2} \sum_{r=0}^{k+1} (\phi_{q_i}^\dagger \phi_{q_i}) \left(-\frac{\partial^2}{M^2} \right)^r (\phi^\dagger \phi) \\ &= \mathcal{L}_{\text{SM}} - \phi^\dagger (\partial^2 + m_\phi^2) \phi - \frac{\lambda_q}{M^2} \sum_{r=0}^k (\phi_{q_i}^\dagger \phi_{q_i}) \left(-\frac{\partial^2}{M^2} \right)^r \partial^2 (\phi^\dagger \phi). \end{aligned} \quad (3.12)$$

In the second line, we have again tuned the quartic coupling

$$\lambda_q = \frac{\mu_q \mu_\phi}{M^2}, \quad (3.13)$$

to cancel the dimension-4 effect. Of course the EFT generates many additional operators beyond the ones written here. However, none of these contribute to the pair production $\phi_q\phi_q^\dagger \rightarrow \phi\phi^\dagger$ at tree level, and so we do not write them explicitly. Similar to the t -channel model, we can identify a scale $\Lambda = M/\sqrt{\lambda_q}$, which sets the overall rate. Once that is specified, the EFT operators relevant here are controlled by a $1/M$ expansion.

3.2.3 On the $1/M$ Versus $1/\Lambda$ EFT Expansions

As explained in Sec. 1.2, current limits on M derived by LHC searches are typically around a few TeV, well below the collider energy, thereby raising the question of EFT validity for practical situations. Using the toy models discussed in Sec. 3.2.1 and Sec. 3.2.2, which characterize the corrections to our benchmark pair production process in Eq. (3.1), we will be focused on the effects of the E/M power series in the EFT expansions (see Eqs. (3.5) and (3.12)). One may be concerned that our results that follow are a special feature of this specific choice. In fact, a different but very typical expectation for a general EFT expansion is that effects from higher dimension operators would come with powers of E/Λ (instead of E/M), where $\Lambda \equiv M/\sqrt{\lambda}$ characterizes the effects of dimension six (leading order) operators with $\lambda = \lambda_{q\phi}$ or λ_q for the t - and s -channel models respectively. Since it is possible that $\Lambda \gg M$ in the weakly coupled limit $\lambda \ll 1$, it could also be the case that $\Lambda > \sqrt{s}$. Therefore, this expectation might make one wonder if EFT validity is actually a problem. In this subsection, we address this potential concern.

In fact, the EFT Lagrangians (Eqs. (3.5) and (3.12)) obtained from the toy models are somewhat special, in the sense that higher order EFT operators come with strictly more powers of *derivatives*. This is not the case for a generic EFT expansion. Taking, for example, the s -channel toy model in Eq. (3.9), we can include

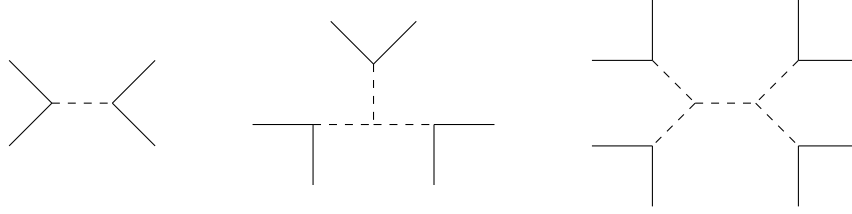


Figure 14. A series of EFT operators with more powers of fields generated by insertions of the self trilinear coupling in the s -channel model. Dashed lines denote the heavy scalar mediator S ; solid lines denote light particles, either scalar quarks or the BSM singlet scalars ϕ .

an allowed self trilinear coupling for the heavy scalar mediator S

$$\mathcal{L}_{s, \text{UV}} \supset \frac{1}{3!} a S^3. \quad (3.14)$$

Insertions of this vertex could generate a series of EFT operators with more powers of *fields* at each order, as illustrated in Fig. 14. In general, higher order EFT operators could contain more powers of either *derivatives* or *fields*. Operators of the former type would obviously contribute with more powers of E/M . Operators of the latter type would contribute with either more powers of E/Λ , or a mix of E/Λ and E/M factors.

To see an example of this, we consider the series of effective operators generated by the diagrams depicted in Fig. 14. We note that these operators have different external states, and hence the associated amplitudes do not interfere with each other. One way to compare the size of their contributions is to consider the inclusive cross section $\phi_q \phi_q^\dagger \rightarrow \text{anything}$. In this case, taking into account phase space, one can show that operators with more insertions of the self trilinear coupling lead to the pattern

$$\text{each cubic insertion} \Rightarrow \frac{\mu_\phi a}{M^2} \frac{E^2}{M^2}. \quad (3.15)$$

Analogous to Eq. (3.8), one could define a “ Λ ” for each UV coupling:⁴

$$\frac{1}{\Lambda_\phi} \equiv \frac{\mu_\phi}{M^2}, \quad \text{and} \quad \frac{1}{\Lambda_a} \equiv \frac{a}{M^2}. \quad (3.16)$$

Using these Λ 's, we can rewrite Eq. (3.15):

$$\frac{\mu_\phi a}{M^2} \frac{E^2}{M^2} = \frac{E}{\Lambda_\phi} \frac{E}{\Lambda_a}. \quad (3.17)$$

We see that in this specific example, operators with more fields would contribute with more powers of E/Λ , agreeing with the typical expectation. In general cases, contributions from operators with more fields and derivatives could come with a mix of E/Λ and E/M factors.

The above discussion shows that the typical expectation that the EFT expansion is governed by E/Λ alone is incomplete; for certain sets of operators it is true (such as in Eq. (3.17)), but other operators could be governed by an E/M expansion (such as in Eqs. (3.5) and (3.12)). Therefore, when $\Lambda \gg M$ as it is for weakly coupled scenarios, our choice to focus on EFTs for the benchmark pair production process in Eq. (3.1) is exploring the *most dangerous* contributions to the question of EFT validity. As we will show in the rest of this chapter, even when considering these most dangerous operators at the limit of perturbativity, EFTs parameter space with $M < \sqrt{s}$ can still be a valid framework for BSM searches using inclusive signal regions, provided that the EFT expansion is not extended to a ridiculously high order.

⁴We note that M and Λ have different units when the factors of \hbar are restored, see e.g. [256, 165]. This underscores the point we are trying to make here, namely that they control two different categories of EFT expansions.

3.3 Partial-Wave Unitarity Bounds

In this section, we investigate the impact of incorporating PDFs into perturbative partial-wave unitarity bounds. This will allow us to explore the interplay of perturbative unitarity violation, which emerges when one probes an EFT at high energies, and PDFs, which act to suppress the production of those problematic high energy events. To this end, we will need to develop a formalism to incorporate PDFs into the partial wave perturbative unitarity test. Specifically, we will generalize the standard partial wave perturbative unitarity argument that applies to pure initial quantum states (appropriate for parton-level scattering) to the case of mixed/ensemble initial quantum states (appropriate for hadron-level scattering).

The results presented in this section are obtained by working with the EFTs discussed in Sec. 3.2. Thus, everything in this section is specific to our simple toy UV completions. The approach of using perturbative unitarity violation to determine EFT validity is often viewed as a bottom-up consistency test. It provides a necessary (but not sufficient) condition that the EFT is a well behaved quantum theory. Although we are providing model specific results here, the conclusions we will draw are expected to apply to general EFTs.

First, Sec. 3.3.1 presents the perturbative unitarity constraints derived using parton-level scattering for the UV theories and the EFTs detailed in Sec. 3.2. Then we turn to Sec. 3.3.2, where we show how to incorporate PDFs into the s -wave perturbative unitarity test. In Sec. 3.3.3, we apply this technique to numerically explore when these constraints are violated. We are particularly interested in scenarios where the new physics scale is below the hadron collider energy $M \ll \sqrt{s}$, and we will show that perturbative unitarity is violated when the EFT truncation order k is sufficiently large. However, when k is small and the signal region is

sufficiently inclusive, the theory passes the perturbative partial-wave unitarity test due to the PDF suppression of high-energy partons. Therefore, such low-order EFTs are free of perturbative unitarity violation. This will allow us to derive upper bounds on the (M, Δ) parameter space, which will denote regions of parameter space where the EFT predictions can not be trusted, i.e., regions where one cannot place experimental bounds on the EFT.

3.3.1 Partonic Initial State

Tree-level perturbative unitarity constraints on a scattering process at the parton level can be obtained by checking that the S -matrix is unitary. In principle, this can be done for each component in the partial wave expansion of the amplitude. We focus on the s -wave component for simplicity. It is somewhat tedious to keep track of all the S -matrix components corresponding to the various spin configurations when fermions are involved in the scattering (see example calculations in [139, 164, 141, 229, 257] and [192, 197] for recent reviews). Minimizing this technical complication is the reason for studying the scalar toy models introduced in Sec. 3.2. As we stated there, we will give $\phi_q(\phi_q^\dagger)$ the same proton PDFs as the quark fields $q(\bar{q})$, and will treat them as massless.

The s -wave perturbative unitarity condition on the parton-level pair production in Eq. (3.1) can be succinctly summarized as:⁵

$$\Omega(\hat{s}) \equiv |\mathcal{M}(\hat{s})|^2 \leq 1, \quad (3.18a)$$

$$\mathcal{M}(\hat{s}) \equiv \left(\frac{\hat{s} - 4m_\phi^2}{\hat{s}} \right)^{1/4} \frac{1}{16\pi} \int_{-1}^1 d(\cos\theta) \mathcal{A}(\cos\theta). \quad (3.18b)$$

⁵Our notation for the normalized s -wave amplitude \mathcal{M} here follows that in [192, 197], which differs from the a_0 notation in *e.g.* [258] by a factor of two: $\mathcal{M} = 2a_0$.

Here \mathcal{A} is the usual scattering amplitude and \mathcal{M} is its s -wave component. In what follows, we will apply this test to the t -channel and s -channel production models detailed in Sec. 3.2, to determine if perturbative partial-wave unitarity is satisfied for this process.

t-Channel UV Theory

For the t -channel production UV model in Eq. (3.2), the scattering amplitude is

$$\mathcal{A}_t = -\frac{|\mu_{q\phi}|^2}{\hat{t} - M^2} - \lambda_{q\phi} = -\lambda_{q\phi} \frac{\hat{t}}{\hat{t} - M^2}, \quad (3.19)$$

where we have applied Eq. (3.6) to tune away the dimension-4 contribution. Following Eq. (3.18) and using the kinematic relation

$$\hat{t} = m_\phi^2 - \frac{\hat{s}}{2} \left(1 - \sqrt{\frac{\hat{s} - 4m_\phi^2}{\hat{s}}} \cos \theta \right), \quad (3.20)$$

the s -wave component is given by integrating over the scattering angle:

$$\begin{aligned} \mathcal{M}_t &= \left(\frac{\hat{s} - 4m_\phi^2}{\hat{s}} \right)^{1/4} \frac{1}{16\pi} \int_{-1}^1 d(\cos \theta) \mathcal{A}_t \\ &= \frac{\lambda_{q\phi} M^2}{8\pi} \frac{\hat{s}}{\hat{s}} \left(\frac{\hat{s} - 4m_\phi^2}{\hat{s}} \right)^{-1/4} \left[\log \frac{1 + \kappa_+}{1 + \kappa_-} - (\kappa_+ - \kappa_-) \right], \end{aligned} \quad (3.21)$$

where we have introduced the dimensionless quantities

$$\kappa_\pm \equiv \frac{\hat{s}}{4M^2} \left(1 \pm \sqrt{\frac{\hat{s} - 4m_\phi^2}{\hat{s}}} \right)^2. \quad (3.22)$$

This leads to the parton-level s -wave perturbative unitarity condition for the t -channel UV model

$$\hat{\Omega}_{t,\text{UV}}(\hat{s}) = |\mathcal{M}_t|^2 = \frac{\lambda_{q\phi}^2}{64\pi^2} \frac{M^4}{\hat{s}^2} \left(\frac{\hat{s} - 4m_\phi^2}{\hat{s}} \right)^{-1/2} \left[\log \frac{1 + \kappa_+}{1 + \kappa_-} - (\kappa_+ - \kappa_-) \right]^2 \leq 1. \quad (3.23)$$

For most of the numerical results that follow, we will set

$$\lambda_{q\phi} = 8\pi, \quad (3.24)$$

which is compatible with the condition in Eq. (3.23), see Fig. 15.

t -Channel EFT

We can obtain the corresponding EFT result $\hat{\Omega}_{t,\text{EFT}}(\hat{s})$ by repeating the above calculation for the EFT Lagrangian in Eq. (3.5). Equivalently, we can expand the UV result for the s -wave amplitude \mathcal{M}_t in Eq. (3.21) as a power series in $1/M^2$ up to some order k (or dimension $\Delta = 6 + 2k$).⁶ This yields

$$\mathcal{M}_t^{[k]} = \frac{\lambda_{q\phi}}{8\pi} \frac{M^2}{\hat{s}} \left(\frac{\hat{s} - 4m_\phi^2}{\hat{s}} \right)^{-1/4} \sum_{r=0}^k \frac{(-1)^{r+1}}{r+2} (\kappa_+^{r+2} - \kappa_-^{r+2}), \quad (3.25)$$

which leads to the EFT s -wave perturbative unitarity condition

$$\hat{\Omega}_{t,\text{EFT}}^{[k]}(\hat{s}) \equiv |\mathcal{M}_t^{[k]}|^2 = \frac{\lambda_{q\phi}^2}{64\pi^2} \frac{M^4}{\hat{s}^2} \left(\frac{\hat{s} - 4m_\phi^2}{\hat{s}} \right)^{-1/2} \left[\sum_{r=0}^k \frac{(-1)^{r+1}}{r+2} (\kappa_+^{r+2} - \kappa_-^{r+2}) \right]^2 \leq 1. \quad (3.26)$$

We see that $\hat{\Omega}_{t,\text{EFT}}^{[k]}(\hat{s})$ goes to infinity as $\hat{s} \rightarrow \infty$. Therefore, we can interpret the condition in Eq. (3.26) as setting a perturbative unitarity cutoff for the parton-level

⁶Note that when deriving the perturbative unitarity condition, the EFT expansion should be applied to the s -wave amplitude \mathcal{M}_t , not to its modulus square $\hat{\Omega}_{t,\text{UV}} \equiv |\mathcal{M}_t|^2$. The latter should always be kept as a complete norm square for each choice of k .

center-of-mass energy $\sqrt{\hat{s}}$. The precise value of this cutoff depends on the EFT truncation dimension Δ , but it will be close to the new physics scale M .

s-Channel UV Theory

Turning to the s -channel UV model defined in Eq. (3.9), the scattering amplitude is

$$\mathcal{A}_s = -\frac{\mu_q \mu_\phi}{\hat{s} - M^2 + iM\Gamma} - \lambda_q = -\lambda_q \frac{\hat{s} + iM\Gamma}{\hat{s} - M^2 + iM\Gamma}, \quad (3.27)$$

where we have applied Eq. (3.13) to tune away the dimension-4 contribution. Again following Eq. (3.18), the s -wave component is

$$\mathcal{M}_s = \left(\frac{\hat{s} - 4m_\phi^2}{\hat{s}} \right)^{1/4} \frac{1}{8\pi} \mathcal{A}_s = -\frac{\lambda_q}{8\pi} \frac{\hat{s} + iM\Gamma}{\hat{s} - M^2 + iM\Gamma} \left(\frac{\hat{s} - 4m_\phi^2}{\hat{s}} \right)^{1/4}, \quad (3.28)$$

which leads to the parton-level s -wave perturbative unitarity condition

$$\hat{\Omega}_{s, \text{UV}}(\hat{s}) = |\mathcal{M}_s|^2 = \frac{\lambda_q^2}{64\pi^2} \frac{\hat{s}^2 + M^2\Gamma^2}{(\hat{s} - M^2)^2 + M^2\Gamma^2} \sqrt{\frac{\hat{s} - 4m_\phi^2}{\hat{s}}} \leq 1. \quad (3.29)$$

The UV theory prediction is maximized on-resonance. Hence, if the theory is free of perturbative unitarity violation when $\hat{s} = M^2$, it will be free of perturbative unitarity violation for all \hat{s} . To ensure this condition, we will set

$$\lambda_q = 2, \quad (3.30)$$

in the rest of this section (see Fig. 19).⁷

⁷We note that although $\hat{\Omega}_{s, \text{UV}}(\hat{s})$ hits 1 at $\hat{s} = M^2$ for $\lambda_q = 2$, imposing tree-level perturbative unitarity for $\sqrt{\hat{s}} \gg M$ actually allows λ_q to be as large as 8π , similar to the t -channel case.

s-Channel EFT

We can obtain the corresponding EFT prediction $\hat{\Omega}_{s,\text{EFT}}(\hat{s})$ by repeating the above calculation for the EFT Lagrangian in Eq. (3.12). Equivalently, we can just expand the UV result for the *s*-wave amplitude \mathcal{M}_s given in Eq. (3.28) in powers of $1/M^2$ (setting $\Gamma \rightarrow 0$) up to some order k . This yields

$$\mathcal{M}_s^{[k]} = \frac{\lambda_q}{8\pi} \left(\frac{\hat{s} - 4m_\phi^2}{\hat{s}} \right)^{1/4} \frac{\hat{s}}{M^2} \sum_{r=0}^k \left(\frac{\hat{s}}{M^2} \right)^r, \quad (3.31)$$

which leads to the partonic *s*-channel EFT *s*-wave perturbative unitarity condition

$$\hat{\Omega}_{s,\text{EFT}}^{[k]}(\hat{s}) \equiv |\mathcal{M}_s^{[k]}|^2 = \frac{\lambda_q^2}{64\pi^2} \sqrt{\frac{\hat{s} - 4m_\phi^2}{\hat{s}}} \left[\frac{\hat{s}}{M^2} \sum_{r=0}^k \left(\frac{\hat{s}}{M^2} \right)^r \right]^2 \leq 1. \quad (3.32)$$

We see that $\hat{\Omega}_{s,\text{EFT}}^{[k]}(\hat{s})$ grows monotonically with \hat{s} (for $\hat{s} \geq 4m_\phi^2$) and goes to infinity as $\hat{s} \rightarrow \infty$. Therefore, the condition in Eq. (3.32) places an upper bound on the parton-level center-of-mass energy $\sqrt{\hat{s}}$, which is identified as the perturbative unitarity cutoff. Its precise value depends on the EFT truncation dimension Δ , but it is always close to the new physics scale M .

3.3.2 Hadronic Initial State

Next, we will derive the *s*-wave perturbative unitarity constraints for the hadronic scattering process in Eq. (3.1). This requires generalizing the standard partial wave perturbative unitarity argument for pure initial quantum states to the case of mixed (or ensemble) initial quantum states.

To begin, recall that for a pure initial state $|i\rangle$, and a pure final state $|f\rangle \neq |i\rangle$, the usual perturbative unitarity condition reads

$$\hat{\Omega}_{i \rightarrow f} \equiv |\mathcal{M}_{i \rightarrow f}|^2 = |\langle f|T|i\rangle|^2 \leq 1, \quad (3.33)$$

where T denotes the scattering operator $S = 1 + iT$. In order to generalize this to the case when the initial state is a mixed state, we rewrite the above condition using the density matrix of the (pure) initial state $\rho_i = |i\rangle\langle i|$:

$$|\langle f|T|i\rangle|^2 \leq 1 \quad \iff \quad \text{tr}(\rho_i T^\dagger |f\rangle\langle f| T) \leq 1. \quad (3.34)$$

Next, we allow the initial state to be an ensemble, whose density matrix is given by

$$\rho_p = \sum_i p_i |i\rangle\langle i| = \sum_i p_i \rho_i, \quad (3.35)$$

where $p_i \geq 0$ are the coefficients (not necessarily normalized) of each pure-state density matrix $|i\rangle\langle i|$. In this case, if the condition in Eq. (3.34) holds for each pure-state, then it must be true that

$$\text{tr}(\rho_p T^\dagger |f\rangle\langle f| T) = \sum_i p_i \text{tr}(\rho_i T^\dagger |f\rangle\langle f| T) \leq \sum_i p_i. \quad (3.36)$$

One can further sharpen this condition by making use of the fact that certain selection rules can be imposed at the amplitude level. Suppose that for a specific final state $|f\rangle$, the amplitude can be nonzero only when the initial state $|i\rangle$ belongs to a subset I of the ensemble

$$|\langle f|T|i\rangle|^2 = \text{tr}(\rho_i T^\dagger |f\rangle\langle f| T) = 0 \quad \text{for } i \notin I. \quad (3.37)$$

In this case, we can incorporate this effect into Eq. (3.36), which gives us

$$\text{tr}(\rho_p T^\dagger |f\rangle\langle f| T) = \sum_{i \in I} p_i \text{tr}(\rho_i T^\dagger |f\rangle\langle f| T) \leq \sum_{i \in I} p_i. \quad (3.38)$$

For the application of interest here, we take the initial state to be the ensemble state formed by the pair of protons, and the final state to be $|f\rangle = |\phi\phi^\dagger\rangle$. Then the left-hand side of Eq. (3.38) is nothing but the parton-level $\hat{\Omega}_{\phi_q\phi_q^\dagger\rightarrow\phi\phi^\dagger}(\hat{s})$ integrated over the parton distribution functions:

$$\begin{aligned} \text{tr}(\rho_p T^\dagger |f\rangle\langle f| T) &= \sum_i p_i |\langle f|T|i\rangle|^2 \\ &= \sum_{\{q,\bar{q}\}\in p} \int_0^1 dx_1 dx_2 \left[f_q(x_1) f_{\bar{q}}(x_2) + f_{\bar{q}}(x_1) f_q(x_2) \right] \hat{\Omega}_{\phi_q\phi_q^\dagger\rightarrow\phi\phi^\dagger}(x_1 x_2 s), \end{aligned} \quad (3.39)$$

where the f_q ($f_{\bar{q}}$) are the PDFs for quarks (anti-quarks), x_1 and x_2 are the corresponding momentum fractions, and we are suppressing the PDF dependence on the renormalization scale.

Since the parton-level $\hat{\Omega}_{\phi_q\phi_q^\dagger\rightarrow\phi\phi^\dagger}(\hat{s})$ only depends on the product

$$\tau \equiv x_1 x_2 = \hat{s}/s, \quad (3.40)$$

it is convenient to work with the parton luminosity function [259]

$$\begin{aligned} L_{q\bar{q}}(\tau) &\equiv \int_0^1 dx_1 dx_2 \left[f_q(x_1) f_{\bar{q}}(x_2) + f_{\bar{q}}(x_1) f_q(x_2) \right] \delta(\tau - x_1 x_2) \\ &= 2 \int_\tau^1 dx \frac{1}{x} f_q(x) f_{\bar{q}}(\tau/x). \end{aligned} \quad (3.41)$$

This allows us to rewrite Eq. (3.39) as

$$\text{tr}(\rho_p T^\dagger |f\rangle\langle f| T) = \sum_{\{q,\bar{q}\}\in p} \int_{\tau_\phi}^1 d\tau L_{q\bar{q}}(\tau) \hat{\Omega}_{\phi_q\phi_q^\dagger\rightarrow\phi\phi^\dagger}(\hat{s} = \tau s), \quad (3.42)$$

where $\tau_\phi = 4m_\phi^2/s$ is the kinematic threshold for the pair production process at the parton level. On the other hand, the right-hand side of Eq. (3.38) can be written as

$$\sum_i p_i = \sum_{\{q, \bar{q}\} \in p} \int_{\tau_\phi}^1 d\tau L_{q\bar{q}}(\tau). \quad (3.43)$$

(Note that we are suppressing the explicit dependence on the selection rule in the sum, see Eq. (3.38).) Therefore, we obtain the s -wave perturbative unitarity condition for the hadronic scattering process $pp \rightarrow \phi\phi^\dagger$:

$$\Omega_{pp \rightarrow \phi\phi^\dagger}(s) \equiv \frac{\sum_{\{q, \bar{q}\} \in p} \int_{\tau_\phi}^1 d\tau L_{q\bar{q}}(\tau) \hat{\Omega}_{\phi_q \phi_{\bar{q}}^\dagger \rightarrow \phi\phi^\dagger}(\hat{s} = \tau s)}{\sum_{\{q, \bar{q}\} \in p} \int_{\tau_\phi}^1 d\tau L_{q\bar{q}}(\tau)} \leq 1. \quad (3.44)$$

This result applies to the case of either scalar or fermionic initial state partons.

3.3.3 Unitarity and EFT Truncation

Now that we have a hadronic formalism for the s -wave perturbative unitarity condition $\Omega \leq 1$, we can investigate its implications when interpreted as an EFT validity test. We will show results for both the t -channel and s -channel models, finding that they yield similar results. Note that to better understand the perturbative unitarity constraints, we will be varying the partonic (hadronic) center-of-mass energy $\sqrt{\hat{s}}$ (\sqrt{s}) in what follows. In particular, \sqrt{s} will not be fixed to 14 TeV. We therefore introduce a notation E_{cm} that denotes this varying center-of-mass energy to avoid confusion.

For the numerical evaluation, we use the CT10 PDFs [260] and set the renormalization scale to 10 TeV for convenience.^{8,9} We choose $m_\phi = 1$ TeV as a

⁸The PDFs minimally change as we vary the renormalization scale from 3 to 100 TeV.

⁹For certain values of M and Δ , efficiently performing the numerical integral over the PDFs is nontrivial. To overcome this challenge, we implemented the adaptive Simpson's method along with some carefully chosen variable changes.

benchmark value, but we emphasize that choosing other values of m_ϕ will yield results with the same qualitative features. To support this claim, we have included a set of results for the case $m_\phi = 10$ GeV in App. B.

t-Channel UV Theory

We begin by investigating the validity of the UV theory by checking the s -wave perturbative unitarity condition for both the partonic and hadronic cases. In Fig. 15, we plot typical curves of $\Omega_{t,\text{UV}}$ as a function of the center-of-mass energy E_{cm} . We see that with our choice of the coupling $\lambda_{q\phi} = |\mu_{q\phi}|^2 / M^2 = 8\pi$ (see Eqs. (3.6) and (3.24)), the UV theory is free of perturbative unitarity violation. Specifically, $\Omega_{t,\text{UV}} < 1$ across the E_{cm} range of interest, in both the partonic initial state and the hadronic initial state cases.

t-Channel EFT

Next, we investigate the consequences for the EFTs. In Fig. 16, we provide typical curves of $\Omega_{t,\text{EFT}}$ as a function of the center-of-mass energy E_{cm} . We see that $\Omega_{t,\text{EFT}}$ becomes larger than 1 in the E_{cm} range of interest, indicating a perturbative unitarity cutoff on E_{cm} .¹⁰ Comparing the partonic initial state case [left] to the hadronic initial state case [right], we see that the growth of $\Omega_{t,\text{EFT}}$ is significantly delayed by the PDF suppression of high-energy partons. Note that the curves are not flattened by the PDFs. This implies that although the perturbative unitarity cutoff on E_{cm} will be pushed significantly higher in the hadronic case, it will not be eliminated, as explicitly verified by Fig. 17. Moreover, the cutoff on E_{cm} is reduced as we increase the EFT truncation dimension Δ , and eventually approaches M in the large Δ limit. This implies that for $E_{\text{cm}} > M$, perturbative unitarity violation is guaranteed if one keeps including more operators beyond a critical truncation dimension.

¹⁰The growth with E_{cm} is not monotonic due to the $(-1)^r$ factor in Eq. (3.26), which comes from the fact that $\hat{t} < 0$.

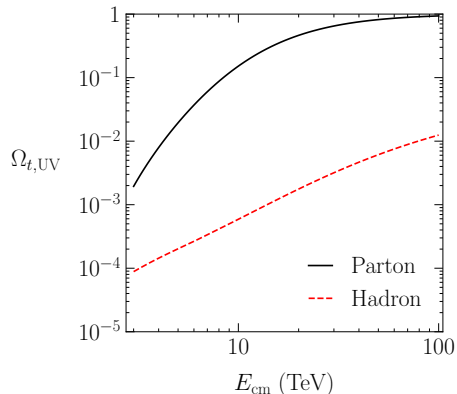


Figure 15. $\Omega_{t,\text{UV}}$ computed using the t -channel UV model as a function of the center-of-mass energy E_{cm} for parton and hadron initial states. This shows that the UV theory is free of perturbative unitarity violation, when the couplings are taken to be $\lambda_{q\phi} = |\mu_{q\phi}|^2/M^2 = 8\pi$.

We conjecture that this is a generic feature of EFTs used in collider searches.

This motivates adopting the following criterion for when an EFT is invalid:

$$\text{The EFT truncated to dimension } \Delta = 6 + 2k \text{ is invalid if } \Omega_{\text{EFT}}^{[k]}(s) > 1. \quad (3.45)$$

Note that this does not guarantee that the EFT is a good description of some underlying UV physics outside of the region deemed invalid by this criterion.

In Fig. 18, we plot the invalid region in the (M, Δ) parameter space obtained by applying this criterion to the t -channel model. We see that going from partons to hadrons opens up significant parameter space for which the EFT could be a valid description. This tells us that perturbative unitarity arguments for the invalidity of EFT analyses performed at hadron colliders in the parameter space where $M < \sqrt{s}$ should incorporate PDF effects when the search region is sufficiently inclusive.

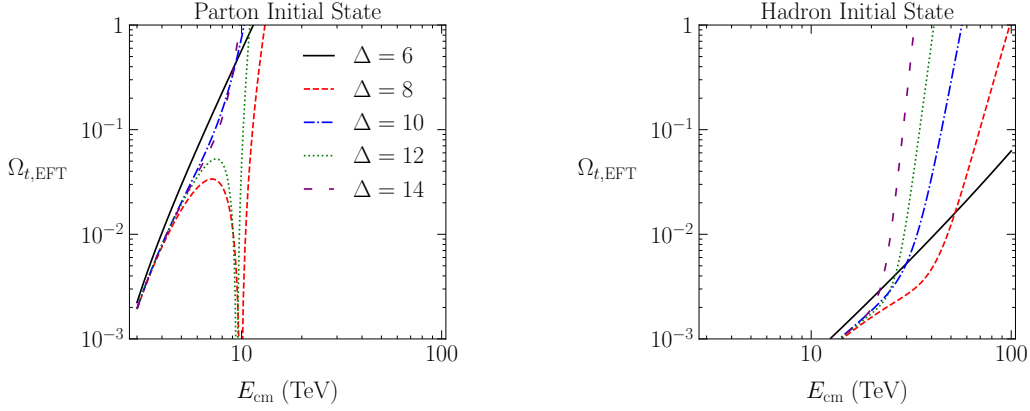


Figure 16. $\Omega_{t,\text{EFT}}$ computed using the EFT expansion of the t -channel model as a function of the center-of-mass energy E_{cm} , for low choices of the truncation dimension $\Delta = 6 + 2k$. For the Partonic Initial State case [left], when $\Delta > 0$, $\Omega_{t,\text{EFT}}$ grows at large E_{cm} and approaches infinity as $E_{\text{cm}} \rightarrow \infty$. This tells us there will be a perturbative unitarity cutoff for a critical value of E_{cm} . In the Hadronic Initial State case [right], the growth of $\Omega_{t,\text{EFT}}$ is significantly delayed as compared to the partonic case.

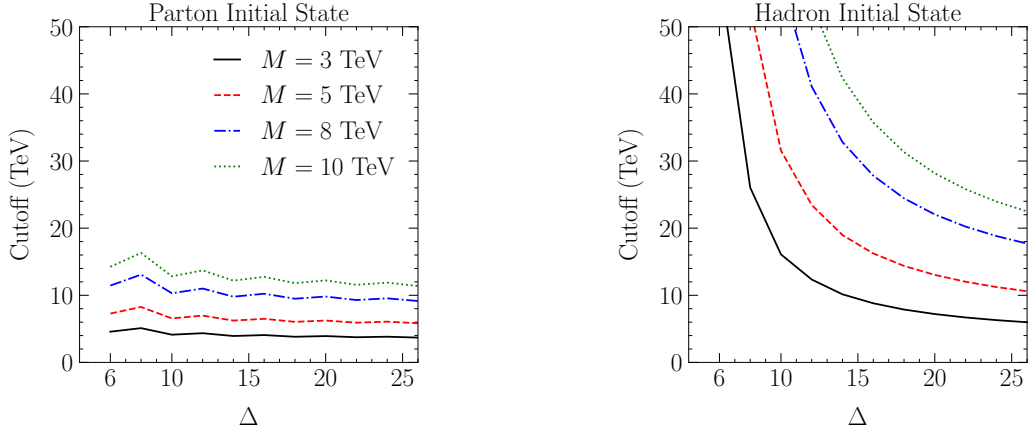


Figure 17. The perturbative unitarity cutoff on E_{cm} as a function of the EFT truncation dimension Δ for the t -channel model, derived using Eq. (3.45). In the Partonic Initial State case [left], the perturbative unitarity cutoffs are more severe than for the Hadronic Initial State case [right], although the PDF effects do not fully remove the bounds.

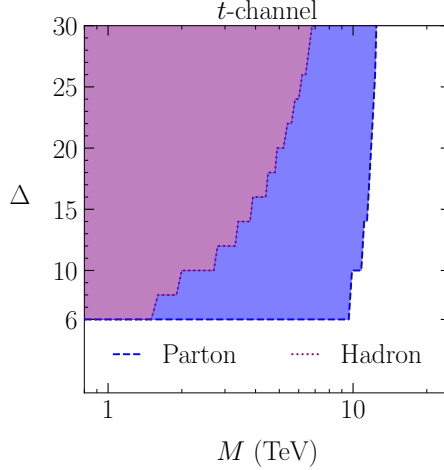


Figure 18. The shaded region shows the parameter space where the EFT is invalid for the t -channel model in the plane of the EFT truncation dimension Δ versus the BSM scale M with $\lambda_{q\phi} = 8\pi$. In the Partonic (Hadronic) Initial State case, we take $\sqrt{\hat{s}}$ (\sqrt{s}) = 14 TeV. The inclusion of PDF effects opens up a region of potentially viable parameter space.

s-Channel UV Theory

The s -channel model yields qualitatively similar results to those we found for the t -channel case. As before, we begin by checking the s -wave perturbative unitarity of the UV theory. In Fig. 19, we plot $\Omega_{s,\text{UV}}$ as a function of the center-of-mass energy E_{cm} . We see that for our choice of the couplings $\lambda_q = \mu_q \mu_\phi / M^2 = 2$ (see Eqs. (3.13) and (3.30)), the UV theory is free of perturbative unitarity violation; $\Omega_{s,\text{UV}} < 1$ across the E_{cm} range of interest at both the parton and hadron level. The resonance feature is clear when varying E_{cm} for the partonic case, but it is smeared out by PDF effects for the hadronic case.

s-Channel EFT

Switching to the EFTs, the requirement of s -wave perturbative unitarity will again tell us that the EFT becomes invalid for some large E_{cm} . As with the t -channel scenario, the growth of $\Omega_{s,\text{EFT}}$ is significantly delayed by the PDF suppression of high-energy partons in the hadronic initial state case. In Fig. 20, we plot the invalid

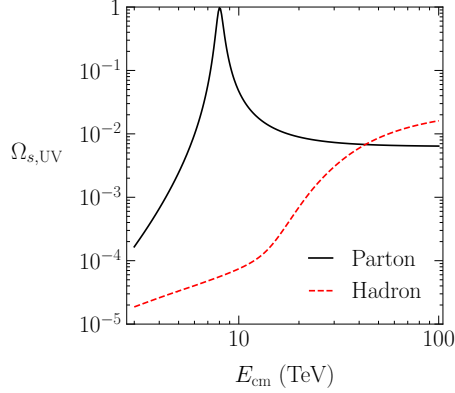


Figure 19. $\Omega_{s,UV}$ computed using the s -channel UV model as a function of the center-of-mass energy E_{cm} . This shows that the UV theory is free of perturbative unitarity violation, when the couplings are taken to be $\lambda_q = \mu_q \mu_\phi / M^2 = 2$.

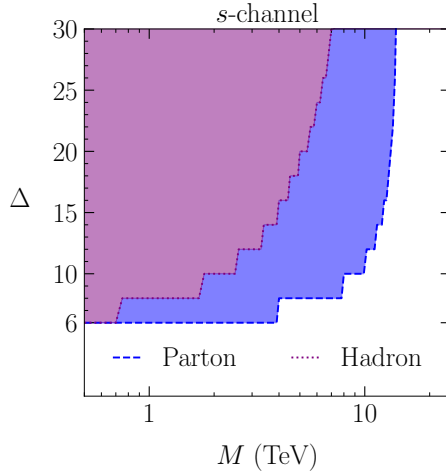


Figure 20. The shaded region shows the parameter space in the plane of the EFT truncation dimension Δ versus the BSM scale M with $\lambda_q = 2$, where the EFT is deemed invalid using the criterion in Eq. (3.45) for the s -channel model. In the Partonic (Hadronic) Initial State case, we take $\sqrt{\hat{s}}$ (\sqrt{s}) = 14 TeV. The inclusion of PDF effects opens up a region of potentially viable parameter space.

region in the (M, Δ) parameter space obtained by applying Eq. (3.45) to the s -channel model. We again see that going from partons to hadrons opens up significant parameter space for which the EFT could be a valid description. Note we have taken $\Gamma \rightarrow 0$ in the EFT expansion when deriving these bounds.

3.4 Interpreting Unitarity Violation

So far, we have simply explored the impact of PDFs on partial wave perturbative unitarity bounds. In particular, we showed the quantitative impact that PDF suppression has on the high energy growth of EFT amplitudes for sufficiently inclusive search regions. This suppression postpones the scale of perturbative unitarity violation, thereby potentially opening up parameter space with $M < \sqrt{s}$ where the EFT could be a useful description. The goal of this section is to interpret these results by comparing them against the predictions for a physical observable.

We will continue to focus on the simple 2-to-2 scattering process in Eq. (3.1). We compare the predictions for its cross section σ as derived from the UV theory and the EFT as we vary the truncation dimension Δ and the mediator mass M against the invalid regions derived in the previous section. For our purposes here, a “valid” EFT is one that

- (i) reproduces the full theory cross section to a reasonable approximation, and
- (ii) converges toward the full theory result as Δ is increased.

We will show that valid EFTs exist in the region opened up by PDF effects.

To determine the hadronic pair production cross section $\sigma_{pp \rightarrow \phi\phi^\dagger}(s)$ from the corresponding partonic one $\hat{\sigma}_{\phi_q\phi_q^\dagger \rightarrow \phi\phi^\dagger}(\hat{s})$, we integrate the partonic cross section over the parton distribution functions using the standard formula

$$\sigma_{pp \rightarrow \phi\phi^\dagger}(s) = \sum_{\{q, \bar{q}\} \in p} \int_{\tau_\phi}^1 d\tau L_{q\bar{q}}(\tau) \hat{\sigma}_{\phi_q\phi_q^\dagger \rightarrow \phi\phi^\dagger}(\hat{s} = \tau s) , \quad (3.46)$$

where we have used the parton luminosity function defined in Eq. (3.41), and the lower bound on the integral $\tau_\phi = 4m_\phi^2/s$ is the kinematic threshold for the pair production process at the parton level.

We are interested in varying the new physics scale M while investigating to what extent

$$\sigma_{\text{EFT}}^{[k]} \equiv \sum_{r=0}^k \sigma_{\text{EFT}}^{(r)} \stackrel{?}{\simeq} \sigma_{\text{UV}}, \quad (3.47)$$

where we are defining the notation $\sigma^{[k]}$ to distinguish the cross section that includes the sum of EFT contributions up to order k ($\Delta = 6 + 2k$; see Eq. (3.7)), from the contribution of an individual term $\sigma^{(r)}$. To this end, Sec. 3.4.1 provides the predictions for the parton-level cross sections $\hat{\sigma}_{\phi_q \phi_q^\dagger \rightarrow \phi \phi^\dagger}(\hat{s})$ for the UV theories and the EFTs detailed in Sec. 3.2. The main results of this section are given in Sec. 3.4.2, where we investigate the question posed in Eq. (3.47) by comparing the numerical results for σ_{EFT} and σ_{UV} for different choices of M and Δ , and use these results to interpret the perturbative partial-wave unitarity results of the previous section.

In the parameter space $M < \sqrt{s}$, we will show that in the limit $\Delta \rightarrow \infty$, the EFT expansion of the cross section is not a convergent series. This implies that one cannot blindly increase the truncation dimension Δ to achieve an arbitrarily good approximation of the underlying UV physics. Nevertheless, thanks to the PDF suppression of high-energy partons, when Δ is small, the relative error between the UV and EFT predictions actually decreases with Δ , as if it were a convergent series. Then for Δ larger than a critical value Δ_{crit} , the error will begin to grow with Δ . This tells us that an EFT analysis performed at low orders can provide an adequate approximation of the underlying UV physics that improves with Δ , even when $M < \sqrt{s}$.

3.4.1 Partonic Initial State Cross Sections

The parton-level cross sections $\hat{\sigma}_{\phi_q \phi_q^\dagger \rightarrow \phi \phi^\dagger}(\hat{s})$ can be computed from the amplitudes derived in the previous section.

t-channel UV Theory

We begin with the t -channel UV model defined in Eq. (3.2). The 2-to-2 scattering amplitude is given in Eq. (3.19). This yields the color averaged squared amplitude

$$\overline{|\mathcal{A}_t|^2} = \frac{1}{3} \lambda_{q\phi}^2 \frac{\hat{t}^2}{(\hat{t} - M^2)^2}. \quad (3.48)$$

Using the kinematic relation in Eq. (3.20), we can integrate over the scattering angle to derive the parton-level total cross section

$$\begin{aligned} \hat{\sigma}_{t,\text{UV}}(\hat{s}) &= 2\pi \int_{-1}^1 d(\cos\theta) \frac{1}{64\pi^2 \hat{s}} \overline{|\mathcal{A}_t|^2} \sqrt{\frac{\hat{s} - 4m_\phi^2}{\hat{s}}} \\ &= \frac{\lambda_{q\phi}^2}{48\pi} \frac{M^2}{\hat{s}^2} \left[\kappa_+ - \kappa_- + \frac{\kappa_+ - \kappa_-}{(1 + \kappa_+)(1 + \kappa_-)} - 2 \log \frac{1 + \kappa_+}{1 + \kappa_-} \right], \end{aligned} \quad (3.49)$$

where κ_\pm is defined in Eq. (3.22), and we are assuming that the initial state scalar quarks are massless.

t-channel EFT

The EFT predictions for the t -channel production cross section can be obtained by repeating the above calculation with the Lagrangian defined in Eq. (3.5). This amounts to expanding the UV result in Eq. (3.49) in powers of $1/M^2$ (encoded by the κ_\pm dependence, see Eq. (3.22)) and truncating the expansion at some EFT order k :

$$\hat{\sigma}_{t,\text{EFT}}^{[k]}(\hat{s}) = \sum_{r=0}^k \hat{\sigma}_{t,\text{EFT}}^{(r)}(\hat{s}), \quad (3.50a)$$

$$\hat{\sigma}_{t,\text{EFT}}^{(r)}(\hat{s}) = \frac{\lambda_{q\phi}^2}{48\pi} \frac{M^2}{\hat{s}^2} \frac{r+1}{r+3} (-1)^r (\kappa_+^{r+3} - \kappa_-^{r+3}). \quad (3.50b)$$

s-channel UV Theory

Now we turn to the s -channel UV model defined in Eq. (3.9). The 2-to-2 scattering amplitude is given in Eq. (3.27). The color averaged squared amplitude is then

$$\overline{|\mathcal{A}_s|^2} = \frac{1}{3} \lambda_q^2 \frac{\hat{s}^2 + M^2 \Gamma^2}{(\hat{s} - M^2)^2 + M^2 \Gamma^2}, \quad (3.51)$$

which leads to the parton-level cross section

$$\hat{\sigma}_{s, \text{UV}}(\hat{s}) = \frac{1}{16\pi \hat{s}} \overline{|\mathcal{A}_s|^2} \sqrt{\frac{\hat{s} - 4m_\phi^2}{\hat{s}}} = \frac{\lambda_q^2}{48\pi} \frac{1}{\hat{s}} \frac{\hat{s}^2 + M^2 \Gamma^2}{(\hat{s} - M^2)^2 + M^2 \Gamma^2} \sqrt{\frac{\hat{s} - 4m_\phi^2}{\hat{s}}}, \quad (3.52)$$

where we are treating the initial state quarks as massless. For the numerics that follow, we will always take $\Gamma = M/(4\pi)$ for simplicity.

s-channel EFT

To work out the EFT predictions for the s -channel production cross section, we can repeat the above calculation with the Lagrangian given in Eq. (3.12), with the width effects incorporated. Equivalently, one can expand the UV result in Eq. (3.52) in powers of $1/M^2$ and truncating the expansion at some order k . This yields

$$\hat{\sigma}_{s, \text{EFT}}^{[k]}(\hat{s}) = \sum_{r=-2}^k \hat{\sigma}_{s, \text{EFT}}^{(r)}(\hat{s}), \quad (3.53a)$$

$$\hat{\sigma}_{s, \text{EFT}}^{(r)}(\hat{s}) = \frac{\lambda_q^2}{48\pi M^2} \sqrt{\frac{\hat{s} - 4m_\phi^2}{\hat{s}}} c_r(\Gamma/M) \left(\frac{\hat{s}}{M^2}\right)^{r+1}, \quad (3.53b)$$

where the coefficient is defined as

$$c_{r-2}(\Gamma/M) \equiv \frac{1}{r!} \left(\frac{\partial}{\partial x}\right)^r \left[\frac{x^2 + (\Gamma/M)^2}{(1-x)^2 + (\Gamma/M)^2} \right] \Bigg|_{x=0}. \quad (3.54)$$

Note that the sum in Eq. (3.53a) starts with $r = -2$ in order to capture the width effects $\Gamma/M \neq 0$ (which technically only appear at loop level). In the zero width limit, the $r = -2$ and $r = -1$ terms would vanish ($c_{-2} = c_{-1} = 0$), because the expression in the square bracket in Eq. (3.54) would have a Taylor expansion that starts with x^2 . The reason we are incorporating the width effects in the EFT matching is that they will be important for properly examining the question posed in Eq. (3.47) when one goes to sufficiently high truncation dimension. We will explore the impact of this “width improved matching” when we compare Figs. 26 and 27 below.

3.4.2 Evidence for EFT Validity

With the cross sections σ_{UV} and σ_{EFT} in hand, we can now turn to answering the question raised in Eq. (3.47). Specifically, we investigate the behavior of the relative error as a function of the truncation dimension $\Delta = 6 + 2k$:

$$\text{Relative Error} \equiv \frac{\sigma_{\text{EFT}}^{[k]}}{\sigma_{\text{UV}}} - 1, \quad (3.55)$$

which provides a proxy for the question of EFT validity. Another useful quantity for exploring this question is the “power counting uncertainty” on the EFT prediction, which we will compute using

$$\text{Power Counting Uncertainty} \equiv \left| \frac{\sigma_{\text{EFT}}^{(k+1)}}{\sigma_{\text{EFT}}^{[k]}} \right|. \quad (3.56)$$

This captures the fact that the EFT is an approximation of the full theory, and this power counting uncertainty provides an indication for the level of confidence one should have when using the EFT prediction.

We will provide results for the t -channel and s -channel models separately; while they are qualitatively similar to each other, we will highlight some interesting

differences in the details. For the numerical results that follow, we again use the CT10 PDFs [260] and set the renormalization scale to 10 TeV for convenience. For the BSM singlet mass, we stick to our benchmark value $m_\phi = 1$ TeV; other values would yield results with the same qualitative feature, as supported by App. B, where we show some results with $m_\phi = 10$ GeV.

3.4.2.1 *t*-channel Results

We plot the absolute value of the relative error in Fig. 21. In the parton case with $M < \sqrt{\hat{s}} = 14$ TeV, the error grows monotonically with Δ , meaning that the EFT approximation keeps getting worse as Δ is increased. This is exactly the expected behavior, since this is effectively attempting to do an expansion when the relevant parameter $\hat{s}/M^2 > 1$, see Eq. (3.50b). For contrast, in the hadron case (now with $M < \sqrt{s} = 14$ TeV), we find that the error *decreases* with Δ for small values of Δ , but turns around at some point and starts increasing at larger Δ . We summarize this intriguing behavior of the EFT results:

- The hadronic EFT expansion appears to be converging at lower orders: we see the EFT approximation improving before hitting a critical value Δ_{crit} .
- The hadronic EFT expansion series does not converge absolutely: it becomes arbitrarily poor at sufficiently large Δ .

In order to illuminate this appearing-to-be converging feature, we provide Fig. 22, which shows typical curves of the relative error without taking the absolute value to highlight how Δ_{crit} is approached.^{11,12}

¹¹Note that the *t*-channel result alternates in sign, due to the $(-1)^r$ factor in Eq. (3.50b), which appears since $\hat{t} < 0$.

¹²This behavior of the EFT validity is very similar, in appearance, to the validity of the perturbation expansion series for the scattering matrix at low orders.

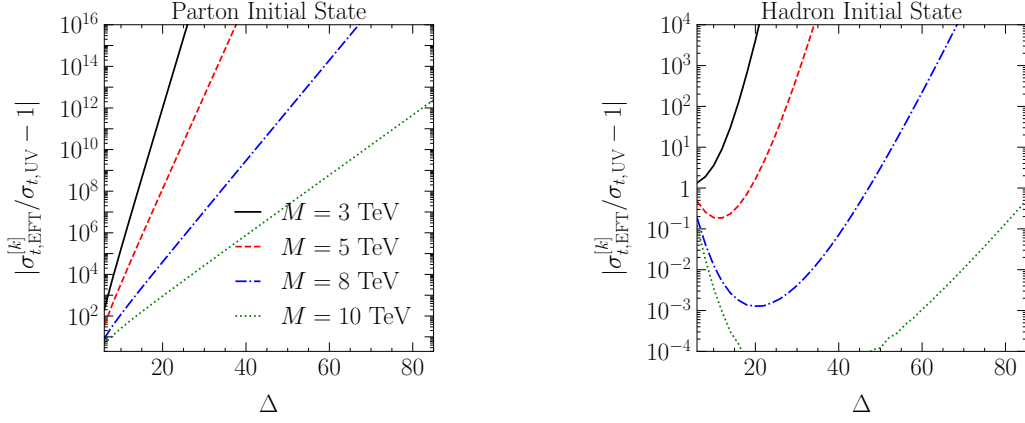


Figure 21. The absolute value of the relative error (see Eq. (3.55)) computed for the t -channel model as a function of the EFT truncation dimension Δ . For the “Partonic Initial State” case [left], we present curves for $M < \sqrt{\hat{s}} = 14$ TeV, which show that the error grows monotonically as Δ is increased. In the “Hadronic Initial State” case [right], we present curves for $M < \sqrt{s} = 14$ TeV, which show that the EFT approximation improves for small values of Δ , but then the error begins to grow for $\Delta > \Delta_{\text{crit}}$.

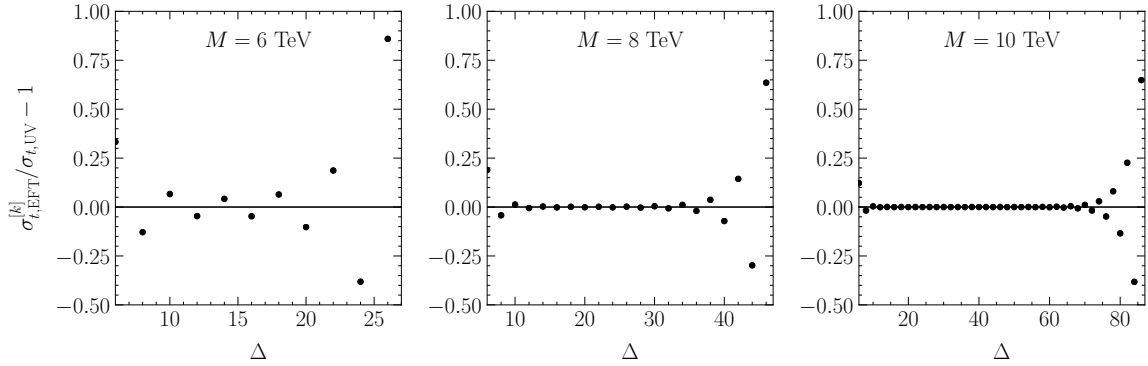


Figure 22. The relative error (see Eq. (3.55)) as computed for the t -channel model in the “Hadronic Initial State” case for $M < \sqrt{s} = 14$ TeV.

We emphasize that this behavior of the EFT expansion only happens for the parameter space where $M < \sqrt{s}$. If instead the new physics scale M is above the collider energy \sqrt{s} , the EFT expansion will yield a convergent series as expected. The contrast between these two regimes can be seen in Fig. 23, where we plot $\sigma_{t,\text{EFT}}^{[k]}/\sigma_{t,\text{UV}}$ as a function of M for a few low lying choices of Δ .

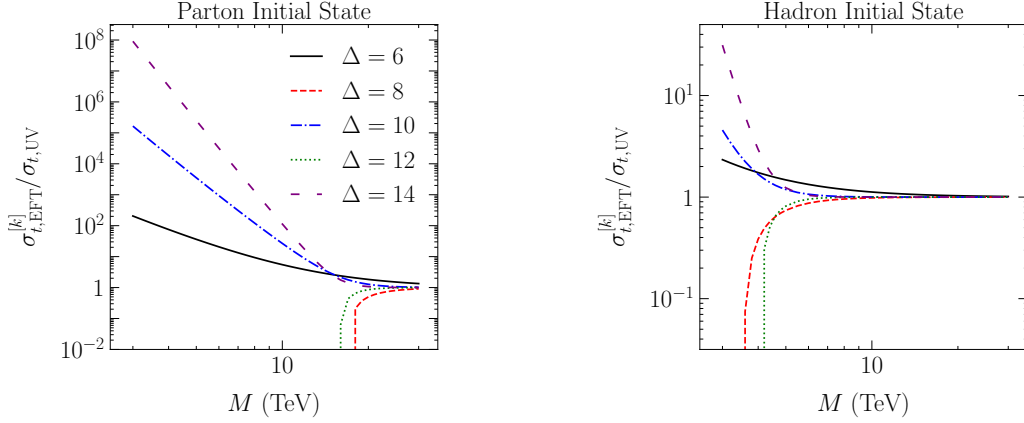


Figure 23. The ratio $\sigma_{t,\text{EFT}}^{[k]}/\sigma_{t,\text{UV}}$ for the first few $\Delta = 6 + 2k$ as a function of M . For the “Partonic Initial State” case [left], the series converges for $M > \sqrt{\hat{s}}$ and diverges for $M < \sqrt{\hat{s}}$. For the “Hadronic Initial State” case [right], the series converges for $M > \sqrt{\hat{s}}$ and appears to be converging when $M \lesssim \sqrt{\hat{s}}$ (although it actually diverges for $\Delta > \Delta_{\text{crit}}$).

We can explore the nature of this critical point in the EFT expansion series by investigating the size of its r^{th} term $|\sigma_{t,\text{EFT}}^{(r)}/\sigma_{t,\text{UV}}|$ as a function of r , see Fig. 24. We see that in the parton case, the terms grow monotonically with r . This is expected because higher-order terms in the EFT expansion come with more powers of $\hat{s}/M^2 > 1$. Moving to the hadron case, we see that the terms tend to decrease with r at small r (as long as M is not too small), making the series appear to be converging. This happens because the PDF suppression of high-energy partons brings down the average parton-level center-of-mass energy

$$\hat{s}_{\text{ave}} \equiv \left(\langle \hat{s}^r \rangle_{\text{PDF}} \right)^{1/r}, \quad (3.57)$$

below M^2 , yielding a suppression factor $\hat{s}_{\text{ave}}/M^2 < 1$. However, the size of $\hat{s}_{\text{ave}} \in [0, s]$ of course depends on r . As one increases r , the effects of $(\hat{s}/M^2)^r$ will eventually win over the PDF suppression factor, causing $\hat{s}_{\text{ave}}/M^2 > 1$, which corresponds to where

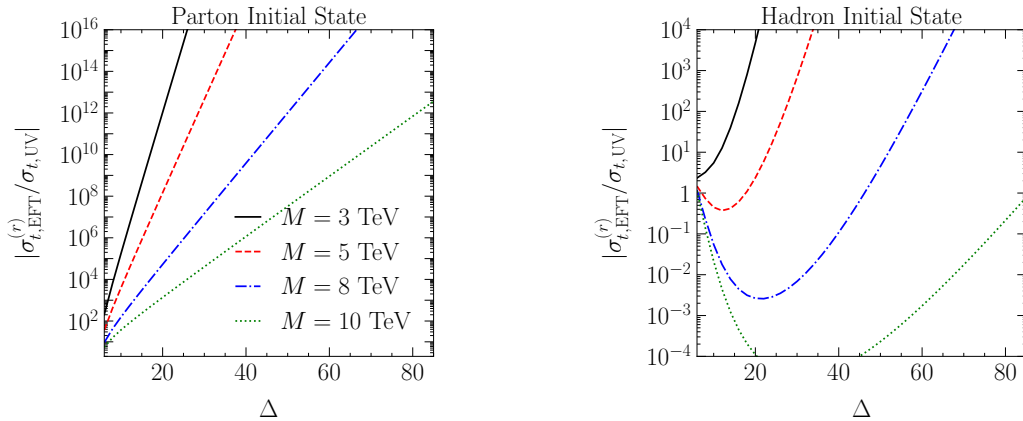


Figure 24. The size of the r^{th} term $|\sigma_{t,\text{EFT}}^{(r)}/\sigma_{t,\text{UV}}|$ as a function of r . In the “Partonic Initial State” case [left], we have $M < \sqrt{\hat{s}} = 14$ TeV; the term grows monotonically with r . In the “Hadronic Initial State” case [right], we have $M < \sqrt{\hat{s}} = 14$ TeV; the term tends to decrease with r for small r (for $M \gtrsim 5$ TeV), and then begins to increase for large r .

the curves turn around in Fig. 24. In fact, \hat{s}_{ave} becomes infinitely close to the collider energy s as we take $r \rightarrow \infty$, so the relative error will always diverge when $s/M^2 > 1$.

Having understood the behavior of the cross section as we vary M and Δ , we can use these results to understand the meaning of the perturbative unitarity bounds derived in the previous section. In Fig. 25, we plot the perturbative unitarity constraint for two points in parameter space, $\lambda_{q\phi} = (8\pi, 2)$ in the (left, right) panel. Additionally, we overlay contours of constant EFT power counting uncertainty as defined in Eq. (3.56).¹³

As a rough guide, we say that the EFT is providing a good approximation of the underlying UV physics when this uncertainty is $< O(1)$. We see that when the coupling is large,¹⁴ violating the hadronic perturbative unitarity constraint essentially rules out the region with $> O(1)$ uncertainty. When the coupling is smaller, there is

¹³Due to the alternating behavior in Eq. (3.50b), the summation to order k is performed separately for even- and odd-valued r terms. We then obtain separate contours for the even and odd sets and interleave them together to restore proper dimension ordering, avoiding a distortion in the contours otherwise.

¹⁴Recall that $\lambda_{q\phi} = 8\pi$ saturates the parton level perturbative unitarity bound.

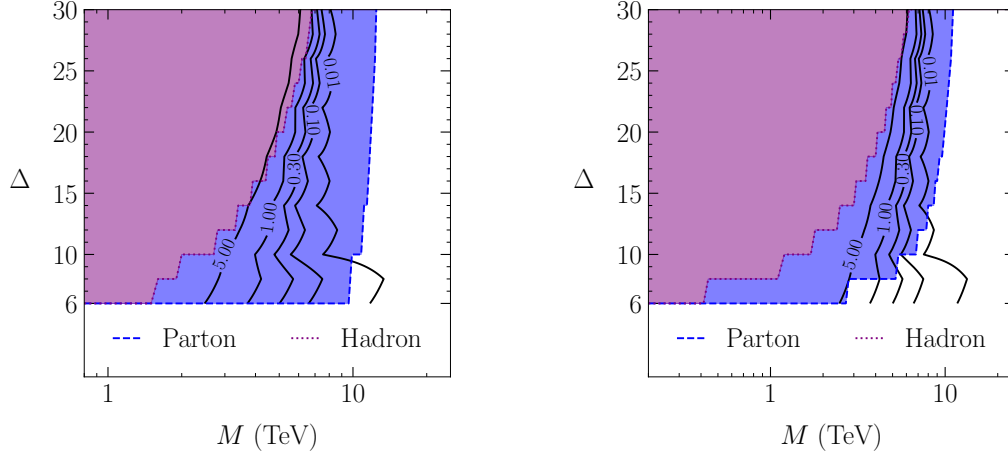


Figure 25. A comparison of the perturbative unitarity results against the t -channel cross section predictions for two choices of the UV parameters: $\lambda_{q\phi} = 8\pi$ [left] and $\lambda_{q\phi} = 2$ [right]. The shaded regions are the perturbative unitarity bounds. The contours show constant power counting uncertainty. This provides evidence that valid EFTs exist in the region excluded by the naive partonic perturbative unitarity bound.

a region with uncertainty $> O(1)$ that is not excluded by the hadronic perturbative unitarity bound. This is not a contradiction, since the perturbative unitarity test is only a necessary (but not sufficient) constraint on the validity of the EFT.

We conclude that there are valid EFTs that lie in the region that would be naively excluded by the partonic perturbative unitarity constraint. Furthermore, the region excluded by considerations of hadronic perturbative unitarity violation do not contain any valid EFTs.

3.4.2.2 s -channel Results

The s -channel production results share the same qualitative features as in the t -channel case. As before, we study the relative error defined in Eq. (3.55) as a function of the truncation order k for the case of the s -channel model. Typical curves of its absolute value are qualitatively similar to those for the t -channel in Fig. 21, where the hadronic EFT expansion also exhibits an apparently converging behavior for small k . This feature is elucidated in Fig. 26, where we plot the relative error without taking

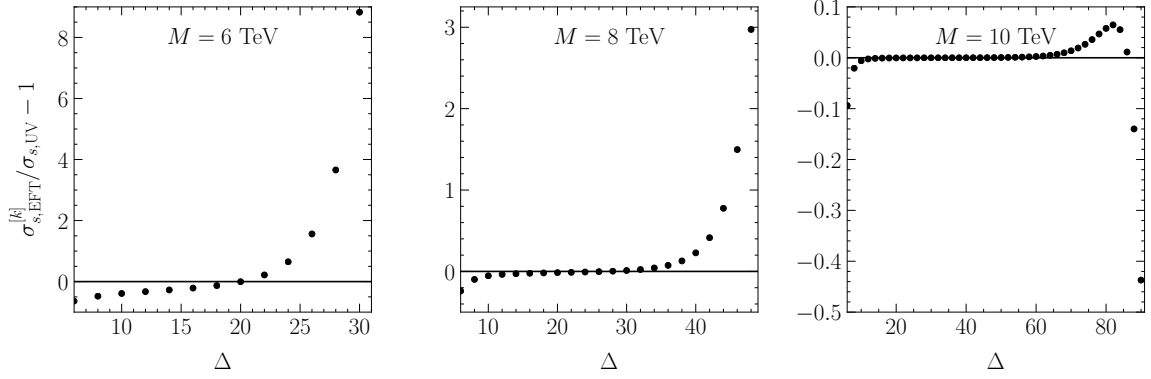


Figure 26. The relative error (see Eq. (3.55)) as computed for the s -channel model in the “Hadronic Initial State” case for $M < \sqrt{s} = 14$ TeV and $m_\phi = 1$ TeV.

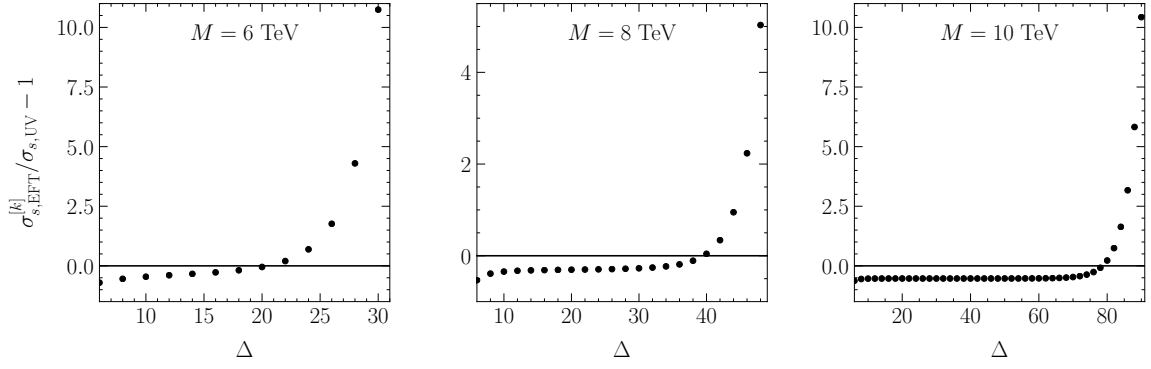


Figure 27. The relative error (see Eq. (3.55)) as computed for the s -channel model in the “Hadronic Initial State” case where $\Gamma \rightarrow 0$ for $M < \sqrt{s} = 14$ TeV and $m_\phi = 1$ TeV. For $\Delta < \Delta_{\text{crit}}$, the EFT prediction appears to be converging to the wrong value.

the absolute value. Note that it is important to include the width effects in the EFT description. In Fig. 27, we show that taking $\Gamma \rightarrow 0$ causes the EFT to converge to the wrong prediction for small k . Just as above, the apparently (but actually not) converging behavior of the EFT expansion only happens when the new physics scale M is below the collider energy \sqrt{s} ; otherwise, the EFT expansion yields a convergent series. The underlying reason for this apparent convergence at small k is again due to the PDF suppression of high-energy partons, which has a non-trivial impact on the relative size between the adjacent terms in the EFT expansion.

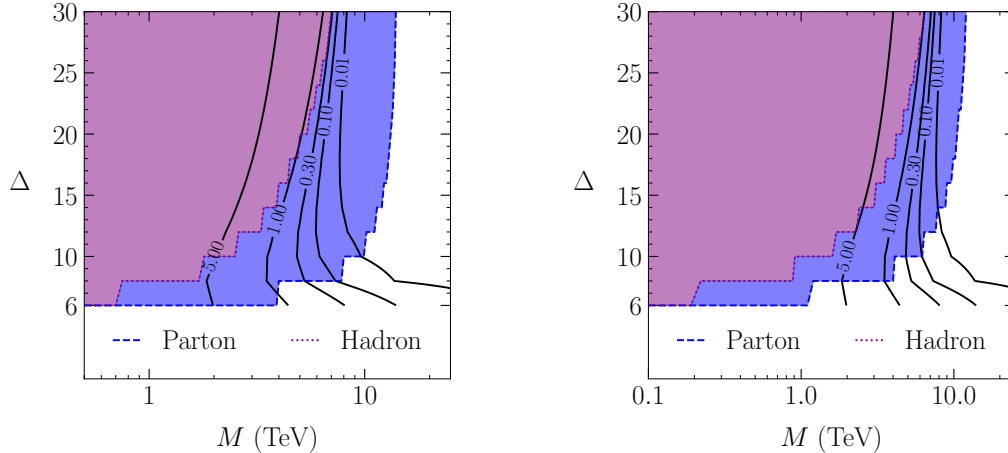


Figure 28. A comparison of the perturbative unitarity results against the s -channel cross section predictions for two choices of the UV parameters: $\lambda_q = 2$ [left] and $\lambda_q = 2/(4\pi)$ [right]. The shaded regions are the perturbative unitarity bounds. The contours show constant power counting uncertainty. This provides evidence that valid EFTs exist in the region excluded by the naive partonic perturbative unitarity bound.

We plot the perturbative unitarity constraint for two points in parameter space, $\lambda_q = (2, 2/(4\pi))$ in the (left, right) panel in Fig. 28, overlaying contours of constant EFT power counting uncertainty (taking $\Gamma = 0$), as defined in Eq. (3.56). Again, this provides evidence for our interpretation that incorporating PDFs into the perturbative unitarity bound is consistent.

3.5 Impact of Kinematic Cuts

In the previous sections, we explored the extent to which PDFs could soften the high energy contributions enough to maintain the validity of an EFT description. We saw it is possible that the EFT provides a useful approximation of the full theory even when $M < \sqrt{s}$, as long as one did not include operators with dimension above some critical value. Our conclusions stem from the essential fact that particle physics scattering is inherently probabilistic, so one needs to collect many events to populate a signal region in order to infer detailed properties of the underlying

theory. In particular, with no further knowledge on the parton-level center-of-mass energy assumed, we computed σ and Ω by integrating over the full kinematic range $\tau \in (\tau_\phi, 1)$ (see Eqs. (3.44) and (3.46)), which led us to the quantitative results in the previous sections.

The goal of this section is to explore how sensitive our conclusions are to incorporating additional information about the parton-level kinematics. Since we are still working in the context of toy models and are only considering 2-to-2 scattering, we will simply focus on just two types of kinematic cuts on the τ integration range:

- Cutting away low energy events (requiring $\sqrt{\hat{s}} > E_{\min}$): this is a proxy for a set of preselection cuts, including a trigger threshold and/or a minimum cut on a kinematic quantity such as p_T , H_T , missing energy, *etc.*
- Cutting away high energy events (requiring $\sqrt{\hat{s}} < E_{\max}$): this is a proxy for comparing with a test of EFT validity that is sometimes employed when doing analyses in the parameter space where $M < \sqrt{s}$. Specifically, we are referring to the test that introduces a cutoff on high energy events and checks that the results are insensitive to this cutoff.

The results of the study where we vary E_{\min} are presented in the left panel of Fig. 29. We adjust the E_{\min} cut from 0, labeled “Hadron” in the figure, to $0.5\sqrt{s}$. We see that the perturbative unitarity bound is not particularly sensitive to the $E_{\min} = 0.2\sqrt{s}$ cut, but then begins to become stronger quickly. When no cut is applied, the perturbative unitarity bound is roughly $M_{\text{bound}} \sim 1.5$ TeV, as compared to $M_{\text{bound}} \sim 5$ TeV when the cut is increased to $E_{\min} = 0.5\sqrt{s}$. This is a consequence of the shape of the PDFs, which decrease by orders of magnitude as x is increased. As we emphasized above, the PDFs suppress high energy events, and by increasing the cut on E_{\min} we are essentially removing that suppression which causes the

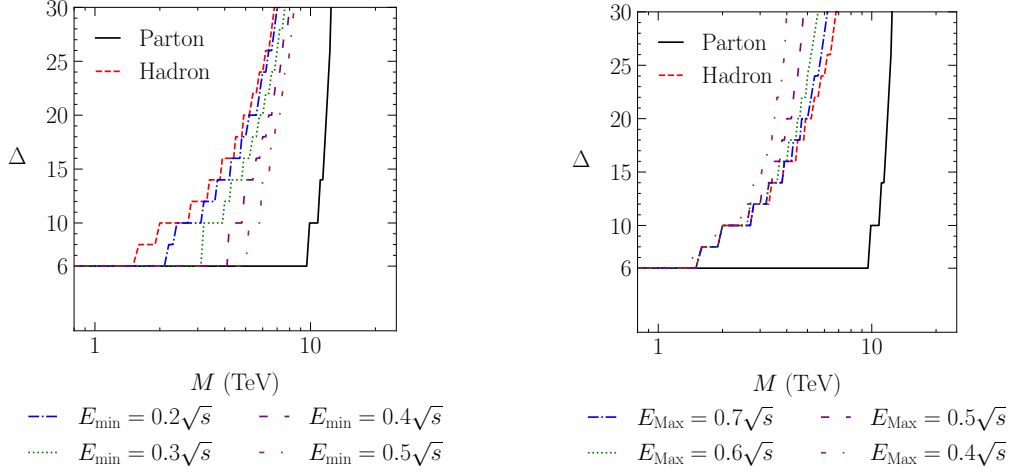


Figure 29. Perturbative unitarity bounds in the Δ versus M plane for various choices of a minimum energy cut E_{\min} [left] and of a maximum energy cut E_{\max} [right] for the t -channel model with $\lambda_{q\phi} = 8\pi$. The region that is incompatible with hadronic perturbative partial-wave unitarity is to the left of the curves.

perturbative unitarity bounds to asymptote to the parton result $M_{\text{bound}} \sim \sqrt{s}$ for $E_{\min} \rightarrow \sqrt{s}$ as they should. When computing the perturbative unitarity bounds on a scenario of interest, it is paramount that these low energy cuts are implemented, since the relevant signal regions often lie in the tails of kinematic distributions (see e.g. [168, 77]).

Next, we turn to the results where we vary E_{\max} presented in the right panel of Fig. 29. This is a proxy for an EFT test that is sometimes utilized, where robustness of the result of an analysis is tested against varying a cutoff on high energy events (see e.g. [66, 67, 68, 69, 70, 71, 72, 73, 253]). In this scheme, the validity of the result depends on how much the derived limits change as a function of E_{\max} . Typically, even in the parameter space where $M < \sqrt{s}$, results are shown to be relatively insensitive to such a cut. We can mimic this test by checking that the hadronic perturbative unitarity bound introduced here is robust to varying E_{\max} . Indeed, when taking the relatively extreme cut $E_{\max} = 0.4\sqrt{s}$, the bounds on M barely change for EFTs

with relatively low truncation dimensions, which is relevant for most of practical applications. This confirms that our bounds are compatible with this test. On the other hand, for large Δ , M_{bound} gets weaker with the E_{max} cut, consistent with our expectation that as we take Δ to be large, $M_{\text{bound}} \rightarrow E_{\text{max}}$.

CHAPTER IV

CONCLUSIONS

4.1 Jet Substructure in Dark Sectors

We explored the theory uncertainties associated with making predictions for a scenario where the presence of a new strongly coupled dark sector leaves its imprint on the substructure of QCD-like jets. We focused on the two-point energy correlation function, $e_2^{(\beta)}$. In particular, we quantified the error resulting from perturbative uncertainties associated with truncating to finite order in the logarithmic and gauge coupling expansions. We also explored the uncertainty due to incalculable non-perturbative hadronization effects. Varying the dark confinement scale $\tilde{\Lambda}$ had the most pronounced impact on the shape of the resulting distributions. We showed $e_2^{(\beta)}$ to be relatively insensitive to the number of dark colors \tilde{N}_C but observed more striking variations when varying the number of dark flavors \tilde{n}_F . We also briefly explored the dependence on the dark quark mass, although we did not provide an error envelope for these distributions due to the technical limitations discussed above.

We then used these error estimates to quantify one's ability to distinguish dark sector jets from the QCD background. We assumed that current bounds on four-quark contact operators apply, which was used to set the production rate for the dark sector. Achieving sensitivity to this subtle signal requires introducing additional handles for the search strategy that could reduce the QCD background by a factor of $O(10^5)$ assuming little impact on the signal efficiency. Depending on the model, one could implement a cut on missing energy, a requirement of one or more b -tagged jets, or identification of displaced vertices or resonances — these additional uncorrelated features could additionally impact the interpretation of the limit on the production cross section, a full exploration of the open parameter space for variations of the base

model is an interesting topic for future work.¹ This signature may also provide an interesting target opportunity for model agnostic approaches to new physics searches that rely on machine learning, e.g. [261, 262, 263, 264, 265, 266, 267, 268]. While such approaches could mitigate the impact of theory uncertainties on the discovery potential of searches using substructure, the importance of uncertainties in setting accurate limits or extracting model parameters in the case of discovery cannot be ignored. Regardless of these details, this study makes clear that a dedicated search that relies on subtle features in substructure will benefit from the full data set collected at the high luminosity LHC, thereby providing a compelling physics target for future experimental efforts.

Moving forward, we acknowledge the practical need for the generalization of the error envelopes presented here to additional substructure variables. It is important to note that properly accounting for the impact of theory errors for a different observable of interest would require a similar study to what we have presented above. In particular, comparable analytic calculations are necessary to characterize theory uncertainties. We do expect that for a class of mass-like observables, i.e., those that display Casimir scaling at LL [55], one would find conclusions broadly similar to the case of e_2 . However, there are cases, e.g. those briefly mentioned at the beginning of Sec. 2.1, with a sufficiently different structure, such that a dedicated study would be necessary to determine the size and scaling of the errors. In the case of uncertainties which can be reliably characterized via Monte Carlo alone, e.g. hadronization modeling, modern machine learning methods similar to those of Ref. [269] might prove helpful in reducing the effort involved. However, we emphasize that a proper analytic accounting of expected theory errors in a resummed

¹If these features are in fact correlated, then the analysis performed in this II would need to be redone.

calculation has no true substitute. The work presented here makes the case that a comprehensive characterization of how substructure observables can be most useful for LHC applications should be performed.

4.2 Unitarity Bounds on Effective Field Theories

We have studied the validity of the EFT framework as it applies to searching for new physics associated with a scale that is below the center-of-mass energy at hadron colliders $M < \sqrt{s}$. The key insight is that when the signal regions are designed to be inclusive regarding the partonic center-of-mass energy, one needs to carefully account for PDF effects, which serve to suppress events that have a high partonic center-of-mass energy. Using the tree-level pair production process in Eq. (3.1) as a benchmark, we have probed this question in the context of perturbative partial-wave unitarity constraints. We conclude that there exists parameter space where the EFT defined with $\Delta < \Delta_{\text{crit}}$ does not violate partial wave perturbative unitarity, even though $M \ll \sqrt{s}$. We provided evidence that there exist valid EFTs that lie in the parameter space opened up by PDF effects. Importantly, this conclusion is of practical relevance to EFT analyses being performed at the LHC, which often result in limits on the EFT scale that are below \sqrt{s} . We emphasize that the perturbative unitarity constraint depends on the kinematics of the process being studied, so for each given search one must perform a dedicated analysis to obtain the EFT parameter space compatible with perturbative partial-wave unitarity.

We view this work as demonstrating that PDF suppression of high energy events can dramatically increase the valid region of parameter space for an EFT search. The most obvious next step is to compute the perturbative unitarity bounds of realistic EFT extensions of the Standard Model, e.g. of relevance to dark matter searches, for

constraining SMEFT operator coefficients, *etc.* Specifically, we would like to revisit the perturbative partial-wave unitarity bound to incorporate fermionic initial states, and then to apply this upgraded calculation to specific EFTs that are being searched for at the LHC. As we discussed in Sec. 3.5, the details of the signal region cuts will also have an impact on the detailed bounds. This analysis will be critical to applying our results in detail at the LHC. It would additionally be interesting to understand the interplay between PDF fits and the inclusion of higher dimension SMEFT operators, along the lines of [270].

We also plan to investigate how our findings here generalize beyond the specific 2-to-2 process of Eq. (3.1). In particular, Eqs. (3.5) and (3.12) show that the EFT expansions for this process are only accounting for higher-dimension operators that strictly involve more powers of derivatives. In general, one would like to see that the same conclusions hold when including operators that involve more powers of fields. While we anticipate that our conclusions will be essentially unchanged when studying the effects of these operators due simply to dimensional analysis presented in Sec. 3.2.3, it will be interesting to see how the interplay of making inclusive/exclusive requirements on the final states will impact the bounds derived here. It will additionally be useful to explore EFT validity in the context of experimental limits that are placed with shape information.

Even if we restrict our scope to the derivative expansion as we have done, there are potential applications that could follow up on some recent studies where resumming the EFT field expansion was utilized:

- Refs. [271, 272, 273, 257] argued that one must include all orders in the field expansion in order to correctly identify if a BSM EFT can be matched onto SMEFT (as opposed to being forced to match onto the more general

formulation with non-linearly realized electroweak symmetry breaking). There is additionally a close relation between perturbative unitarity violation and inclusive amplitudes involving an arbitrary number of fields in the final state [274, 275].

- When focusing on BSM modifications to the two-point and three-point amplitudes, it was emphasized that the derivative expansion is trivial [276, 277]. In these cases, one can resum the field expansion in SMEFT, an approach that was recently advocated in [277].
- Going beyond two-point and three-point amplitudes, a resummation over the field expansion will leave us with a non-trivial derivative expansion [277]. Nevertheless, the derivative expansion can still be systematically organized through the use of group theoretical techniques [278, 276].

Once the field expansion is resummed, the EFT will only include a derivative expansion. Therefore, our study here helps to justify the validity of analyses that resum (some of) the field expansion, and it would be of significant interest to understand the interplay between these ideas and PDF effects.

Finally, we will briefly comment on the implications for new search designs at the LHC. Given the dependence of the perturbative unitarity bound on the kinematics used to define the signal region of the search, one could be motivated to narrow the range of final state energies to sharpen the perturbative unitarity bound. However, this typically increases the statistical error, thereby reducing the power of the search. Furthermore, since the meaning of the unitarity bound is limited to the assumption of perturbativity, it is unclear how much is gained by attempting to sharpen it by modifying the search strategy. Based on these considerations, we believe that in many cases, it might be advantageous to keep the energy bin of the experimental search

somewhat inclusive. Investigating this interplay is worthy of dedicated studies, which we leave for future work.

Analyses that utilize EFTs are of critical importance to the LHC program. Accounting for the impact of PDFs on their range of validity will allow us to utilize these frameworks with confidence as we continue to pursue the experimental signatures of beyond the Standard Model physics.

APPENDIX A

ANALYTIC DETAILS OF THE RESUMMATION CALCULATION

In this appendix, we review the analytic calculation of the e_2 distribution to NLL order. Our discussion closely follows those of Refs. [55, 103], which in turn are based on the framework developed in Refs. [279, 106, 107]. Our primary goal here is to provide some additional clarification on technical points that may be less familiar to reader not as versed in the details of QCD resummation. For a recent introduction to the general principles of final state resummation accessible to non-experts, see Ref. [280].

We begin with the collinear limit of the e_2 distribution, which is doubly divergent due to a collinear logarithm from the angular integral and a soft logarithm from the integral over the so-called splitting functions. These splitting functions $p_i(z)$, which depend on the momentum fraction z can be used to derived resummed distributions. The leading order (LO) contribution is due to a single emission. This can be simply modeled by integrating the splitting function against a delta function that enforces the 2-body momentum conservation as applied to Eq. (2.1). To this order, the differential distribution is

$$\frac{1}{\sigma} \frac{d\sigma_i^{\text{LO}}}{de_2} = \frac{\alpha_s}{\pi} \int_0^{R_0} \frac{d\theta}{\theta} \int_0^1 dz p_i(z) \delta\left(z(1-z)\left(\frac{\theta}{R_0}\right)^\beta - e_2\right), \quad (\text{A.1})$$

where $p_i(z)$ is the appropriate parton splitting function for a quark-initiated jet or a gluon-initiated jet, which are given by

$$\begin{aligned}
p_q(z) &= P_{g \leftarrow q}(z) = C_F \frac{1+z^2}{1-z}, \\
p_g(z) &= \frac{1}{2} P_{g \leftarrow g}(z) + n_F P_{q \leftarrow g}(z) \\
&= C_A \left(\frac{z}{1-z} + \frac{1-z}{z} + z(1-z) \right) + n_F T_R (z^2 + (1-z)^2). \tag{A.2}
\end{aligned}$$

For quark-initiated jets, only $P_{g \leftarrow q}$ is included, since the function $P_{q \leftarrow q}$ is not divergent in the soft limit and would effectively double count the jet core. Likewise, for gluon-initiated jets, the factor of $\frac{1}{2}$ multiplying $P_{g \leftarrow g}$ accounts for a double counting that results from there being the two gluons emerging from a single gluon, while the factor of n_F multiplying $P_{q \leftarrow g}$ provides the proper counting statistics for the gluon to split into n_F different quark pairs.

In the limit where $e_2 \ll 1$, we can simplify $z(1-z)(\theta/R_0)^\beta \simeq z(\theta/R_0)^\beta$ by assuming $z \ll 1$. It is then straightforward to evaluate Eq. (A.1), which yields

$$\frac{e_2}{\sigma} \frac{d\sigma_i^{\text{LO}}}{de_2} \simeq \frac{2\alpha_s}{\pi} \frac{C_i}{\beta} \left(\ln \frac{1}{e_2} + B_i + O(e_2) \right), \tag{A.3}$$

where $C_q = C_F = \frac{N_C^2-1}{2N_C}$ and $C_g = C_A = N_C$ are the color factors associated with the jet and $B_q = -\frac{3}{4}$ and $B_g = -\frac{11}{12} + \frac{n_F T_R}{3C_A}$ encode the subleading terms in the splitting functions and arise from hard collinear emissions. At LO, the cumulative distribution exhibits a characteristic double logarithm in the limit of small e_2 . Denoting the logarithm as $L \equiv \ln \frac{1}{e_2}$, one finds

$$\begin{aligned}
\Sigma_i^{\text{LO}} &\equiv \int_0^{e_2} dx \frac{1}{\sigma} \frac{d\sigma_i^{\text{LO}}}{dx} = 1 - \int_{e_2}^{e_2^{(\beta)\text{max}}} dx \frac{1}{\sigma} \frac{d\sigma_i^{\text{LO}}}{dx} \\
&= 1 - \frac{\alpha_s}{\pi} \frac{C_i}{\beta} \left(L^2 + 2B_i L + O(1) \right). \tag{A.4}
\end{aligned}$$

Note that the first integral is divergent, since we have not accounted for virtual corrections. However, we can sidestep this issue by assuming that the probability to emit anywhere is finite. Instead of computing the missing $O(\alpha_s)$ corrections to the total rate, we instead invoke unitarity to write the integral in the second finite form which implicitly includes the virtual corrections.

Due to presence of the logarithm in Eq. (A.4), perturbative control over the differential distribution is lost for small values of e_2 . Particles with different color charges are going to give qualitatively different behavior in precisely this limit, and so it is necessary to resum the resulting logarithms to all orders to explore how the distributions differ. To leading-log (LL) accuracy, one can consider the emission of n collinear partons within the jet as independent, with the scale of the (one-loop) coupling for each splitting m chosen at the relative transverse momentum scale $\kappa_m = z_m \theta_m p_{T,J}$. Virtual corrections do not change the kinematics, so they will contribute to the distribution for any value of the observable, whereas real emissions will only contribute if the kinematic configuration is such that the emission angle is smaller than the jet radius. At LO, virtual corrections only yield a divergent correction to the tree-level value of $e_2 = 0$. Thus, to LL accuracy, the resummed cumulative distribution can be computed by simply summing over all emissions off the initial parton while treating them as uncorrelated. In the small z limit, and taking the second form of the integral in Eq. (A.4) to work with finite quantities, the resummed cumulative distribution is given by

$$\begin{aligned} \Sigma_i^{\text{LL}} &= \sum_{n=0}^{\infty} \frac{1}{n!} \prod_{m=1}^n \int_0^{R_0} \frac{d\theta_m}{\theta_m} \int_0^1 dz_m p_i(z_m) \frac{\alpha_s(\kappa_m)}{\pi} \left(\Theta \left(e_2 - z_m \left(\frac{\theta_m}{R_0} \right)^\beta \right) - 1 \right) \\ &= \sum_{n=0}^{\infty} \frac{(-1)^n}{n!} \prod_{m=1}^n \int_0^{R_0} \frac{d\theta_m}{\theta_m} \int_0^1 dz_m p_i(z_m) \frac{\alpha_s(\kappa_m)}{\pi} \Theta \left(z_m \left(\frac{\theta_m}{R_0} \right)^\beta - e_2 \right), \quad (\text{A.5}) \end{aligned}$$

where the second line sums over virtual emissions, which have the same matrix element as real emissions by unitarity (modulo a sign difference) [106, 107]. The series above is readily resummed into a single term, correct to double logarithmic accuracy:

$$\begin{aligned}\Sigma_i^{\text{LL}} &= e^{-R_i}, \\ R_i &= \int_0^{R_0} \frac{d\theta}{\theta} \int_0^1 dz p_i(z) \frac{\alpha_s(\kappa)}{\pi} \Theta\left(z\left(\frac{\theta}{R_0}\right)^\beta - e_2\right).\end{aligned}\quad (\text{A.6})$$

The function R_i is called the radiator for the jet, and it captures the Sudakov double logarithms associated with the IR divergences that result from soft or collinear emissions from the hard parton. In the fixed coupling approximation, the radiator has the form

$$R_i \simeq \frac{\alpha_s C_i}{\pi \beta} \left(L^2 + 2B_i L + O(1) \right), \quad (\text{A.7})$$

so that expanding Σ^{LL} to leading order in the radiator recovers the LO behavior in Eq. (A.4).

At NLL order a number of new effects appear: multiple emissions, the two-loop running coupling, and non-global logarithms that arise from out-of-jet-emissions falling within the cone. The resummed cumulative distribution can be improved to single logarithmic accuracy by explicitly summing over uncorrelated emissions:¹

$$\begin{aligned}\Sigma_i^{\text{NLL}} &= \sum_{n=0}^{\infty} \frac{1}{n!} \prod_{m=1}^n \int_0^{R_0} \frac{d\theta_m}{\theta_m} \int_0^1 dz_m p_i(z_m) \frac{\alpha_s(k_m)}{\pi} \Theta(\theta_{m-1} - \theta_m) \\ &\times \Theta\left(e_2 - \sum_{m=1}^n z_m \left(\frac{\theta_m}{R_0}\right)^\beta\right) e^{-\int_0^{R_0} \frac{d\theta}{\theta} \int_0^1 dz p_i(z) \frac{\alpha_s(\kappa)}{\pi}}.\end{aligned}\quad (\text{A.8})$$

¹This formula ignores the effects of non-global logarithms, which must be separately implemented to achieve true NLL accuracy.

The angular ordering condition comes from the fact that when inserting an eikonal emission factor $\sum_i \mathbf{T}_i k_i \cdot \epsilon / k_i \cdot q$ into an existing matrix element \mathcal{M} , the squared matrix element picks up a kinematic factor of

$$|\mathcal{M}|^2 \sim \sum_{i < j} W_{ij}, \quad \text{where} \quad W_{ij} = \frac{1 - \cos \theta_{ij}}{(1 - \cos \theta_{iq})(1 - \cos \theta_{jq})}. \quad (\text{A.9})$$

Each such term can be rewritten as $W_{ij} = W_{ij}^{(i)} + W_{ij}^{(j)}$, where

$$W_{ij}^{(i)} = \frac{1}{2} \left(W_{ij} + \frac{1}{1 - \cos \theta_{iq}} - \frac{1}{1 + \cos \theta_{jq}} \right). \quad (\text{A.10})$$

The benefit of this rewriting is that every such term satisfies an angular ordering property,

$$\int_0^{2\pi} \frac{d\phi_{iq}}{2\pi} W_{ij}^{(i)} = \begin{cases} \frac{1}{1 - \cos \theta_{iq}} & \theta_{iq} < \theta_{ij} \\ 0 & \text{otherwise} \end{cases}, \quad (\text{A.11})$$

such that the soft limits are correctly reproduced through the treatment of collinear divergences and angular ordering together. The resulting expression can be evaluated in Laplace space, where the convolution of the splitting function, running coupling, and the Θ functions become a summable product, yielding [106]

$$\begin{aligned} \Sigma_i^{\text{NLL}} &= \int \frac{d\nu}{2\pi i \nu} e^{e_2} e^{-R_i}, \\ R_i &= \int_0^{R_0} \frac{d\theta}{\theta} \int_0^1 dz p_i(z) \frac{\alpha_s(\kappa)}{\pi} \left(1 - e^{-\nu z \left(\frac{\theta}{R_0}\right)^\beta} \right), \end{aligned} \quad (\text{A.12})$$

where R_i here is the Laplace space version of the expression in Eq. (A.6).

Logarithmic accuracy in ν tracks the logarithmic accuracy in e_2 , since they are Laplace conjugates of each other. Therefore, to derive the NLL cumulative

distribution, one must compute the radiator to single logarithmic accuracy in ν . Expanding about $\nu^{-1} = e_2$ gives

$$\begin{aligned}\Sigma_i^{\text{NLL}} &= N \frac{e^{-\gamma_E R'_i}}{\Gamma(1 + R'_i)} e^{-R_i}, \\ R'_i &\equiv \frac{dR_i}{dL},\end{aligned}\tag{A.13}$$

where $N = 1 + O(\alpha_s)$ is a matching coefficient that can be determined by comparing with the fixed-order cumulative distribution, γ_E is the Euler–Mascheroni constant, and the radiator R_i is given in Eq. (A.6).

Note that improving predictability to NLL order requires matching the resummed calculation to the fixed-order distribution. To this end, we implement the Log- R matching scheme [108] by first considering the LO cumulative distribution, i.e., the properly integrated form of Eq. (A.1),

$$\ln \Sigma_i^{\text{LO}} = \frac{\alpha_s}{\pi} \int_0^{R_0} \frac{d\theta}{\theta} \int_0^1 dz p_i(z) \Theta \left(z \left(\frac{\theta}{R_0} \right)^\beta - e_2 \right) = -\frac{\alpha_s}{\pi} R_{1,i},\tag{A.14}$$

where

$$\begin{aligned}R_{1,q} &= \frac{C_F}{\beta} \left(-4 \text{Li}_2 \left(\frac{1+u}{2} \right) + 3u + \ln^2(1-u) - 2 \ln(1+u) \ln(1-u) \right. \\ &\quad \left. + (4 \ln 2 - \ln(1+u)) \ln(1+u) - 3 \tanh^{-1} u + \frac{\pi^2}{3} - 2 \ln^2 2 \right), \\ R_{1,g} &= \frac{C_A}{\beta} \left(-4 \text{Li}_2 \left(\frac{1+u}{2} \right) + \left(\frac{67}{18} - \frac{2}{9} C_1^{(\beta)} \right) u - \frac{n_F}{C_A} \left(\frac{13}{18} - \frac{2}{9} C_1^{(\beta)} \right) u \right. \\ &\quad \left. + \ln^2(1-u) - 2 \ln(1+u) \ln(1-u) + (4 \ln 2 - \ln(1+u)) \ln(1+u) \right. \\ &\quad \left. - \left(\frac{11}{3} - \frac{2n_F}{3C_A} \right) \tanh^{-1} u + \frac{\pi^2}{3} - 2 \ln^2 2 \right),\end{aligned}\tag{A.15}$$

and $u \equiv \sqrt{1 - e_2}$. Here u takes values between $u = \sqrt{1 - e_{2,\max}} = \sqrt{1 - \frac{1}{4}R_0^\beta}$ and 1. With the Log- R matching scheme, it is straightforward to match the resummed and fixed-order results,

$$\Sigma_i^{\text{NLL}} = N \frac{e^{-\gamma_E R'_i}}{\Gamma(1 + R'_i)} \exp(-R_i) \exp\left(-\frac{\alpha_s}{\pi}(R_{1,i} - G_{2,i}L^2 - G_{1,i}L)\right), \quad (\text{A.16})$$

where $G_{2,i}L^2$ and $G_{1,i}L$ are the logarithms appearing in the fixed-order expression which must to be subtracted from $R_{1,i}$ to avoid double counting the resummed logarithms. From Eq. (A.4), these logarithms are explicitly

$$G_{2,i}L^2 + G_{1,i}L = \frac{C_i}{\beta}(L^2 + 2B_iL). \quad (\text{A.17})$$

Using this analytic form in Eq. (A.16) requires evaluating the radiator R_i , which is given in Eq. (A.6). An analytic evaluation of R_i is possible, although challenging, e.g. see Ref. [110]. The calculation of the resulting efficiencies at NLL due to a cut on e_2 requires evaluating the gauge coupling α_s at two-loop order using the CMW scheme [111], such that efficiencies still need to be computed numerically. Another issue is related to α_s becoming non-perturbative as the integral is evaluated at low enough scales. Following the procedure in Ref. [103], the coupling is only run at one-loop order and is frozen at the non-perturbative scale $\mu_{\text{NP}} \equiv 7\Lambda$. These choices result in a closed-form solution for R_i while limiting its logarithmic accuracy, so Eq. (A.16) provides a modified leading logarithmic (MLL) resummed cumulative distribution with FO corrections. All analytic distributions presented above are to LL or MLL+FO accuracy, but strictly not accurate to full NLL order.

The prescription of freezing the coupling at the non-perturbative scale $\mu_{\text{NP}} \equiv 7\Lambda$ leads to the explicit form

$$\alpha_s(\kappa) = \alpha_s^{(1\text{L})}(\kappa)\Theta(\kappa - \mu_{\text{NP}}) + \alpha_s^{(1\text{L})}(\mu_{\text{NP}})\Theta(\mu_{\text{NP}} - \kappa), \quad (\text{A.18})$$

where $\alpha_s^{(1\text{L})}(\kappa)$ is the standard one-loop order expression for the coupling,

$$\alpha_s^{(1\text{L})}(\kappa) = \frac{1}{2\beta_0 \ln(\frac{\kappa}{\Lambda})}. \quad (\text{A.19})$$

For brevity, we introduce the function $F(x) = x \ln x$ and define the following variables:

$$\begin{aligned} L &= \ln \frac{1}{e_2} & L_\mu &= \ln \frac{1}{\mu}, \\ \lambda &= 2\alpha_s\beta_0 L & \lambda_\mu &= 2\alpha_s\beta_0 L_\mu, \end{aligned} \quad (\text{A.20})$$

where $\mu = \frac{\mu_{\text{NP}}}{p_T R_0}$ is the relevant scale associated with the non-perturbative transition.

Finally, we will write down the explicit expressions for the radiator functions that are used here. Their form depends on the choice of the angular dependence β .

For $\beta > 1$,

$$R_i^{(\beta>1)} = \begin{cases} \frac{C_i}{2\pi\alpha_s\beta_0^2} \left(\frac{F(1-\lambda)}{\beta-1} - \frac{\beta F(1-\frac{1}{\beta}\lambda)}{\beta-1} - 2\alpha_s\beta_0 B_i \ln\left(1 - \frac{1}{\beta}\lambda\right) \right) & e_2 > \mu \\ \frac{C_i}{2\pi\alpha_s\beta_0^2} \left(\frac{F(1-\lambda_\mu)}{\beta-1} - \frac{\beta F(1-\frac{1}{\beta}\lambda)}{\beta-1} - \frac{1+\ln(1-\lambda_\mu)}{\beta-1}(\lambda - \lambda_\mu) \right. \\ \quad \left. - 2\alpha_s\beta_0 B_i \ln\left(1 - \frac{1}{\beta}\lambda\right) \right) + \frac{C_i\alpha_s(\mu_{\text{NP}})}{\pi} \frac{(L-L_\mu)^2}{\beta-1} & \mu \geq e_2 > \mu^\beta \\ \frac{C_i}{2\pi\alpha_s\beta_0^2} \left(-F(1-\lambda_\mu) - (1+\ln(1-\lambda_\mu))\lambda_\mu \right. \\ \quad \left. - 2\alpha_s\beta_0 B_i \ln(1-\lambda_\mu) \right) \\ \quad + \frac{C_i\alpha_s(\mu_{\text{NP}})}{\pi} \left((\beta-1)L_\mu^2 + \frac{L-\beta L_\mu}{\beta}(L + \beta L_\mu + 2B_i) \right) & \mu^\beta \geq e_2 \end{cases},$$

(A.21)

while for $\beta < 1$,

$$R_i^{(\beta < 1)} = \begin{cases} \frac{C_i}{2\pi\alpha_s\beta_0^2} \left(\frac{F(1-\lambda)}{\beta-1} - \frac{\beta F(1-\frac{1}{\beta}\lambda)}{\beta-1} - 2\alpha_s\beta_0 B_i \ln\left(1 - \frac{1}{\beta}\lambda\right) \right) & e_2 > \mu \\ \frac{C_i}{2\pi\alpha_s\beta_0^2} \left(\frac{F(1-\lambda)}{\beta-1} - \frac{\beta F(1-\lambda_\mu)}{\beta-1} - \frac{1+\ln(1-\lambda_\mu)}{\beta-1} (\lambda - \beta\lambda_\mu) \right. \\ \quad \left. - 2\alpha_s\beta_0 B_i \ln(1 - \lambda_\mu) \right) \\ \quad + \frac{C_i\alpha_s(\mu_{\text{NP}})}{\pi} \frac{L-\beta L_\mu}{\beta} \frac{L-\beta L_\mu+2(1-\beta)B_i}{1-\beta} & \mu \geq e_2 > \mu^\beta, \\ \frac{C_i}{2\pi\alpha_s\beta_0^2} \left(-F(1 - \lambda_\mu) - (1 + \ln(1 - \lambda_\mu))\lambda_\mu \right. \\ \quad \left. - 2\alpha_s\beta_0 B_i \ln(1 - \lambda_\mu) \right) \\ \quad + \frac{C_i\alpha_s(\mu_{\text{NP}})}{\pi} \frac{L(L+2B_i)-\beta L_\mu(L_\mu+2B_i)}{\beta} & \mu^\beta \geq e_2 \end{cases} \quad (\text{A.22})$$

Finally, in the limit $\beta \rightarrow 1$, Eq. (A.21) and Eq. (A.22) match:

$$R_i^{(\beta=1)} = \begin{cases} \frac{C_i}{2\pi\alpha_s\beta_0^2} \left(-F(1 - \lambda) - (1 + \ln(1 - \lambda))\lambda - 2\alpha_s\beta_0 B_i \ln(1 - \lambda) \right) & e_2^{(1)} > \mu \\ \frac{C_i}{2\pi\alpha_s\beta_0^2} \left(-F(1 - \lambda_\mu) - (1 + \ln(1 - \lambda_\mu))\lambda_\mu - 2\alpha_s\beta_0 B_i \ln(1 - \lambda_\mu) \right) \\ \quad + \frac{C_i\alpha_s(\mu_{\text{NP}})}{\pi} (L - L_\mu)(L + L_\mu + 2B_i) & \mu \geq e_2^{(1)} \end{cases} \quad (\text{A.23})$$

APPENDIX B

UNITARITY BOUNDS FOR SMALLER FINAL STATE MASS

In this Appendix, we provide the perturbative unitarity bounds on the EFT parameter space (M, Δ) for the case that the final state particles have a mass of 10 GeV, see Figs. B.1 and B.2. The impact of cutting away low (high) energy events is shown in the left (right) panel of Fig. B.3.

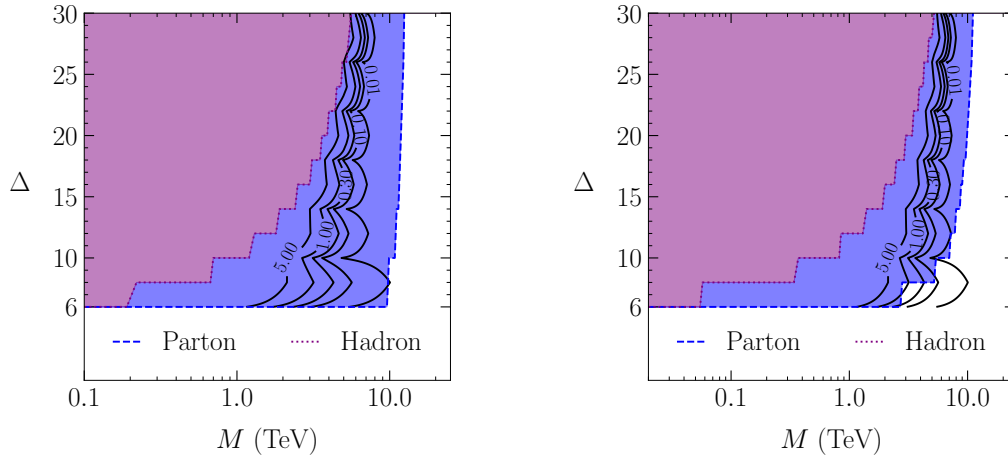


Figure B.1. A comparison of the perturbative unitarity results against the t -channel cross section predictions for two choices of the UV parameters: $\lambda_{q\phi} = 8\pi$ [left] and $\lambda_{q\phi} = 2$ [right] in the case that the final state particles have a mass of 10 GeV. The shaded regions are the perturbative unitarity bounds, while the contours show power counting error.

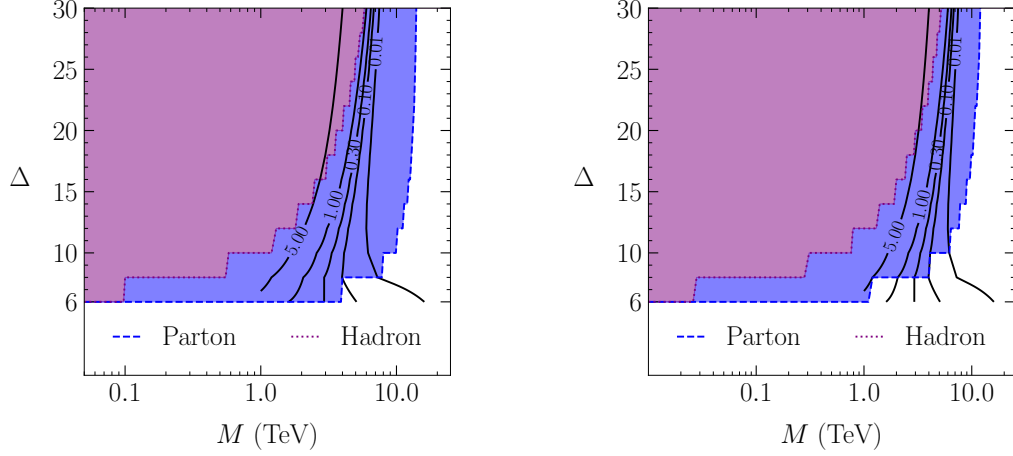


Figure B.2. A comparison of the perturbative unitarity results against the s -channel cross section predictions for two choices of the UV parameters: $\lambda_q = 2$ [left] and $\lambda_q = 2/(4\pi)$ [right] in the case that the final state particles have a mass of 10 GeV. The shaded regions are the perturbative unitarity bounds, while the contours show power counting error.

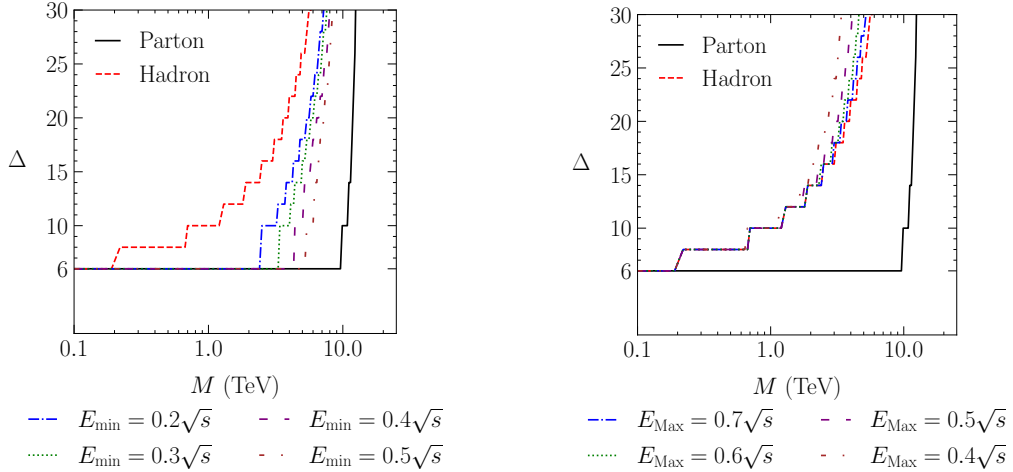


Figure B.3. Perturbative unitarity bounds in the Δ versus M plane for various choices of a minimum energy cut E_{\min} [left] and of a maximum energy cut E_{\max} [right] for the t -channel model with $\lambda_{q\phi} = 8\pi$ in the case that the final state particles have a mass of 10 GeV. The region that is incompatible with hadronic perturbative partial-wave unitarity is to the left of the curves.

REFERENCES CITED

- [1] J. Alwall, M.-P. Le, M. Lisanti, and J. G. Wacker, “Model-Independent Jets plus Missing Energy Searches,” *Phys. Rev.* **D79** (2009) 015005, [arXiv:0809.3264 \[hep-ph\]](#).
- [2] J. Alwall, P. Schuster, and N. Toro, “Simplified Models for a First Characterization of New Physics at the LHC,” *Phys. Rev.* **D79** (2009) 075020, [arXiv:0810.3921 \[hep-ph\]](#).
- [3] **LHC New Physics Working Group** Collaboration, D. Alves, “Simplified Models for LHC New Physics Searches,” *J. Phys.* **G39** (2012) 105005, [arXiv:1105.2838 \[hep-ph\]](#).
- [4] M. J. Strassler and K. M. Zurek, “Echoes of a hidden valley at hadron colliders,” *Phys. Lett.* **B651** (2007) 374–379, [arXiv:hep-ph/0604261 \[hep-ph\]](#).
- [5] T. Han, Z. Si, K. M. Zurek, and M. J. Strassler, “Phenomenology of hidden valleys at hadron colliders,” *JHEP* **07** (2008) 008, [arXiv:0712.2041 \[hep-ph\]](#).
- [6] R. Harnik and T. Wizansky, “Signals of New Physics in the Underlying Event,” *Phys. Rev.* **D80** (2009) 075015, [arXiv:0810.3948 \[hep-ph\]](#).
- [7] M. J. Strassler, “On the Phenomenology of Hidden Valleys with Heavy Flavor,” [arXiv:0806.2385 \[hep-ph\]](#).
- [8] J. E. Juknevich, D. Melnikov, and M. J. Strassler, “A Pure-Glue Hidden Valley I. States and Decays,” *JHEP* **07** (2009) 055, [arXiv:0903.0883 \[hep-ph\]](#).
- [9] J. E. Juknevich, “Pure-gluon hidden valleys through the Higgs portal,” *JHEP* **08** (2010) 121, [arXiv:0911.5616 \[hep-ph\]](#).
- [10] L. Carloni and T. Sjöstrand, “Visible Effects of Invisible Hidden Valley Radiation,” *JHEP* **09** (2010) 105, [arXiv:1006.2911 \[hep-ph\]](#).
- [11] L. Carloni, J. Rathsmann, and T. Sjöstrand, “Discerning Secluded Sector gauge structures,” *JHEP* **04** (2011) 091, [arXiv:1102.3795 \[hep-ph\]](#).
- [12] M. S. Seth, “A first study of Hidden Valley models at the LHC,” Master’s thesis, Lund Observ., 2011.
- [13] G. D. Kribs and E. T. Neil, “Review of strongly-coupled composite dark matter models and lattice simulations,” *Int. J. Mod. Phys.* **A31** (2016) no. 22, 1643004, [arXiv:1604.04627 \[hep-ph\]](#).

- [14] S. Knapen, S. Pagan Griso, M. Papucci, and D. J. Robinson, “Triggering Soft Bombs at the LHC,” *JHEP* **08** (2017) 076, [arXiv:1612.00850 \[hep-ph\]](#).
- [15] K. R. Dienes, F. Huang, S. Su, and B. Thomas, “Dynamical Dark Matter from Strongly-Coupled Dark Sectors,” *Phys. Rev.* **D95** (2017) no. 4, 043526, [arXiv:1610.04112 \[hep-ph\]](#).
- [16] A. Pierce, B. Shakya, Y. Tsai, and Y. Zhao, “Searching for confining hidden valleys at LHCb, ATLAS, and CMS,” *Phys. Rev.* **D97** (2018) no. 9, 095033, [arXiv:1708.05389 \[hep-ph\]](#).
- [17] O. Buchmueller, A. De Roeck, K. Hahn, M. McCullough, P. Schwaller, K. Sung, and T.-T. Yu, “Simplified Models for Displaced Dark Matter Signatures,” *JHEP* **09** (2017) 076, [arXiv:1704.06515 \[hep-ph\]](#).
- [18] G. D. Kribs, A. Martin, and T. Tong, “Effective Theories of Dark Mesons with Custodial Symmetry,” *JHEP* **08** (2019) 020, [arXiv:1809.10183 \[hep-ph\]](#).
- [19] G. D. Kribs, A. Martin, B. Ostdiek, and T. Tong, “Dark Mesons at the LHC,” *JHEP* **07** (2019) 133, [arXiv:1809.10184 \[hep-ph\]](#).
- [20] L. Lee, C. Ohm, A. Soffer, and T.-T. Yu, “Collider Searches for Long-Lived Particles Beyond the Standard Model,” *Prog. Part. Nucl. Phys.* **106** (2019) 210–255, [arXiv:1810.12602 \[hep-ph\]](#).
- [21] H. Beauchesne, E. Bertuzzo, and G. Grilli Di Cortona, “Dark matter in Hidden Valley models with stable and unstable light dark mesons,” *JHEP* **04** (2019) 118, [arXiv:1809.10152 \[hep-ph\]](#).
- [22] J. Alimena *et al.*, “Searching for Long-Lived Particles beyond the Standard Model at the Large Hadron Collider,” [arXiv:1903.04497 \[hep-ex\]](#).
- [23] E. Bernreuther, F. Kahlhoefer, M. Kramer, and P. Tunney, “Strongly interacting dark sectors in the early Universe and at the LHC through a simplified portal,” *Submitted to: J. High Energy Phys.* (2019) , [arXiv:1907.04346 \[hep-ph\]](#).
- [24] H.-C. Cheng, L. Li, E. Salvioni, and C. B. Verhaaren, “Light Hidden Mesons through the Z Portal,” [arXiv:1906.02198 \[hep-ph\]](#).
- [25] L. Li and Y. Tsai, “Detector-size Upper Bounds on Dark Hadron Lifetime from Cosmology,” *JHEP* **05** (2019) 072, [arXiv:1901.09936 \[hep-ph\]](#).
- [26] P. Brax, S. Fichet, and P. Tanedo, “The Warped Dark Sector,” *Phys. Lett. B* **798** (2019) 135012, [arXiv:1906.02199 \[hep-ph\]](#).
- [27] H. Beauchesne and G. Grilli di Cortona, “Classification of dark pion multiplets as dark matter candidates and collider phenomenology,” *JHEP* **02** (2020) 196, [arXiv:1910.10724 \[hep-ph\]](#).

- [28] A. Costantino, S. Fichet, and P. Tanedo, “Effective Field Theory in AdS: Continuum Regime, Soft Bombs, and IR Emergence,” [arXiv:2002.12335 \[hep-th\]](#).
- [29] B. Holdom, “Two $U(1)$ ’s and Epsilon Charge Shifts,” *Phys. Lett.* **166B** (1986) 196–198.
- [30] B. Patt and F. Wilczek, “Higgs-field portal into hidden sectors,” [arXiv:hep-ph/0605188 \[hep-ph\]](#).
- [31] A. Falkowski, J. Juknevič, and J. Shelton, “Dark Matter Through the Neutrino Portal,” [arXiv:0908.1790 \[hep-ph\]](#).
- [32] N. Arkani-Hamed and N. Weiner, “LHC Signals for a SuperUnified Theory of Dark Matter,” *JHEP* **12** (2008) 104, [arXiv:0810.0714 \[hep-ph\]](#).
- [33] M. Baumgart, C. Cheung, J. T. Ruderman, L.-T. Wang, and I. Yavin, “Non-Abelian Dark Sectors and Their Collider Signatures,” *JHEP* **04** (2009) 014, [arXiv:0901.0283 \[hep-ph\]](#).
- [34] Y. F. Chan, M. Low, D. E. Morrissey, and A. P. Spray, “LHC Signatures of a Minimal Supersymmetric Hidden Valley,” *JHEP* **05** (2012) 155, [arXiv:1112.2705 \[hep-ph\]](#).
- [35] **ATLAS** Collaboration, G. Aad *et al.*, “A search for prompt lepton-jets in pp collisions at $\sqrt{s} = 8$ TeV with the ATLAS detector,” *JHEP* **02** (2016) 062, [arXiv:1511.05542 \[hep-ex\]](#).
- [36] M. Buschmann, J. Kopp, J. Liu, and P. A. N. Machado, “Lepton Jets from Radiating Dark Matter,” *JHEP* **07** (2015) 045, [arXiv:1505.07459 \[hep-ph\]](#).
- [37] **ATLAS** Collaboration, G. Aad *et al.*, “Search for light long-lived neutral particles produced in pp collisions at $\sqrt{s} = 13$ TeV and decaying into collimated leptons or light hadrons with the ATLAS detector,” [arXiv:1909.01246 \[hep-ex\]](#).
- [38] P. Schwaller, D. Stolarski, and A. Weiler, “Emerging Jets,” *JHEP* **05** (2015) 059, [arXiv:1502.05409 \[hep-ph\]](#).
- [39] **CMS** Collaboration, A. M. Sirunyan *et al.*, “Search for new particles decaying to a jet and an emerging jet,” *JHEP* **02** (2019) 179, [arXiv:1810.10069 \[hep-ex\]](#).
- [40] S. Renner and P. Schwaller, “A flavoured dark sector,” *JHEP* **08** (2018) 052, [arXiv:1803.08080 \[hep-ph\]](#).
- [41] T. Cohen, M. Lisanti, and H. K. Lou, “Semivisible Jets: Dark Matter Undercover at the LHC,” *Phys. Rev. Lett.* **115** (2015) no. 17, 171804, [arXiv:1503.00009 \[hep-ph\]](#).

- [42] T. Cohen, M. Lisanti, H. K. Lou, and S. Mishra-Sharma, “LHC Searches for Dark Sector Showers,” *JHEP* **11** (2017) 196, [arXiv:1707.05326 \[hep-ph\]](#).
- [43] M. Park and M. Zhang, “Tagging a jet from a dark sector with Jet-substructures at colliders,” [arXiv:1712.09279 \[hep-ph\]](#).
- [44] H. Beauchesne, E. Bertuzzo, G. Grilli Di Cortona, and Z. Tabrizi, “Collider phenomenology of Hidden Valley mediators of spin 0 or 1/2 with semivisible jets,” *JHEP* **08** (2018) 030, [arXiv:1712.07160 \[hep-ph\]](#).
- [45] G. P. Salam, “Towards Jetography,” *Eur. Phys. J.* **C67** (2010) 637–686, [arXiv:0906.1833 \[hep-ph\]](#).
- [46] A. Abdesselam *et al.*, “Boosted Objects: A Probe of Beyond the Standard Model Physics,” *Eur. Phys. J.* **C71** (2011) 1661, [arXiv:1012.5412 \[hep-ph\]](#).
- [47] A. Altheimer *et al.*, “Jet Substructure at the Tevatron and LHC: New results, new tools, new benchmarks,” *J. Phys.* **G39** (2012) 063001, [arXiv:1201.0008 \[hep-ph\]](#).
- [48] A. Altheimer *et al.*, “Boosted Objects and Jet Substructure at the LHC. Report of BOOST2012, held at IFIC Valencia, 23rd-27th of July 2012,” *Eur. Phys. J.* **C74** (2014) no. 3, 2792, [arXiv:1311.2708 \[hep-ex\]](#).
- [49] J. Shelton, “Jet Substructure,” in *TASI 2012*, pp. 303–340. 2013. [arXiv:1302.0260 \[hep-ph\]](#).
- [50] D. Adams *et al.*, “Towards an Understanding of the Correlations in Jet Substructure,” *Eur. Phys. J.* **C75** (2015) no. 9, 409, [arXiv:1504.00679 \[hep-ph\]](#).
- [51] M. Cacciari, “Phenomenological and theoretical developments in jet physics at the LHC,” *Int. J. Mod. Phys.* **A30** (2015) no. 31, 1546001, [arXiv:1509.02272 \[hep-ph\]](#).
- [52] A. J. Larkoski, I. Moutl, and B. Nachman, “Jet Substructure at the Large Hadron Collider: A Review of Recent Advances in Theory and Machine Learning,” [arXiv:1709.04464 \[hep-ph\]](#).
- [53] S. Marzani, G. Soyez, and M. Spannowsky, “Looking inside jets: an introduction to jet substructure and boosted-object phenomenology,” [arXiv:1901.10342 \[hep-ph\]](#). [Lect. Notes Phys.958,(2019)].
- [54] *Les Houches 2017: Physics at TeV Colliders Standard Model Working Group Report*. 2018. [arXiv:1803.07977 \[hep-ph\]](#). <http://lss.fnal.gov/archive/2018/conf/fermilab-conf-18-122-cd-t.pdf>.

- [55] A. J. Larkoski, G. P. Salam, and J. Thaler, “Energy Correlation Functions for Jet Substructure,” *JHEP* **06** (2013) 108, [arXiv:1305.0007 \[hep-ph\]](#).
- [56] J. Pumplin, “How to tell quark jets from gluon jets,” *Phys. Rev. D* **44** (1991) 2025–2032.
- [57] I. Moulton, L. Necib, and J. Thaler, “New Angles on Energy Correlation Functions,” *JHEP* **12** (2016) 153, [arXiv:1609.07483 \[hep-ph\]](#).
- [58] C. Frye, A. J. Larkoski, J. Thaler, and K. Zhou, “Casimir Meets Poisson: Improved Quark/Gluon Discrimination with Counting Observables,” *JHEP* **09** (2017) 083, [arXiv:1704.06266 \[hep-ph\]](#).
- [59] A. J. Larkoski and E. M. Metodiev, “A Theory of Quark vs. Gluon Discrimination,” *JHEP* **10** (2019) 014, [arXiv:1906.01639 \[hep-ph\]](#).
- [60] Z. Nagy and D. E. Soper, “What is a parton shower?,” *Phys. Rev.* **D98** (2018) no. 1, 014034, [arXiv:1705.08093 \[hep-ph\]](#).
- [61] Z. Nagy and D. E. Soper, “Parton showers with more exact color evolution,” *Phys. Rev.* **D99** (2019) no. 5, 054009, [arXiv:1902.02105 \[hep-ph\]](#).
- [62] S. Alioli, C. W. Bauer, C. Berggren, F. J. Tackmann, and J. R. Walsh, “Drell-Yan production at NNLL+NNLO matched to parton showers,” *Phys. Rev.* **D92** (2015) no. 9, 094020, [arXiv:1508.01475 \[hep-ph\]](#).
- [63] S. Höche, D. Reichelt, and F. Siegert, “Momentum conservation and unitarity in parton showers and NLL resummation,” *JHEP* **01** (2018) 118, [arXiv:1711.03497 \[hep-ph\]](#).
- [64] J. R. Forshaw, J. Holguin, and S. Plätzer, “Building a consistent parton shower,” [arXiv:2003.06400 \[hep-ph\]](#).
- [65] M. Dasgupta, F. A. Dreyer, K. Hamilton, P. F. Monni, G. P. Salam, and G. Soyez, “Parton showers beyond leading logarithmic accuracy,” [arXiv:2002.11114 \[hep-ph\]](#).
- [66] **ATLAS** Collaboration, G. Aad *et al.*, “Search for new phenomena in events with a photon and missing transverse momentum in pp collisions at $\sqrt{s} = 8$ TeV with the ATLAS detector,” *Phys. Rev. D* **91** (2015) no. 1, 012008, [arXiv:1411.1559 \[hep-ex\]](#). [Erratum: *Phys.Rev.D* 92, 059903 (2015)].
- [67] **ATLAS** Collaboration, G. Aad *et al.*, “Search for new phenomena in final states with an energetic jet and large missing transverse momentum in pp collisions at $\sqrt{s} = 8$ TeV with the ATLAS detector,” *Eur. Phys. J. C* **75** (2015) no. 7, 299, [arXiv:1502.01518 \[hep-ex\]](#). [Erratum: *Eur.Phys.J.C* 75, 408 (2015)].

- [68] **ATLAS** Collaboration, G. Aad *et al.*, “Search for Dark Matter in Events with Missing Transverse Momentum and a Higgs Boson Decaying to Two Photons in pp Collisions at $\sqrt{s} = 8$ TeV with the ATLAS Detector,” *Phys. Rev. Lett.* **115** (2015) no. 13, 131801, [arXiv:1506.01081 \[hep-ex\]](#).
- [69] **ATLAS** Collaboration, G. Aad *et al.*, “Search for dark matter produced in association with a Higgs boson decaying to two bottom quarks in pp collisions at $\sqrt{s} = 8$ TeV with the ATLAS detector,” *Phys. Rev. D* **93** (2016) no. 7, 072007, [arXiv:1510.06218 \[hep-ex\]](#).
- [70] **CMS** Collaboration, V. Khachatryan *et al.*, “Search for dark matter and unparticles produced in association with a Z boson in proton-proton collisions at $\sqrt{s} = 8$ TeV,” *Phys. Rev. D* **93** (2016) no. 5, 052011, [arXiv:1511.09375 \[hep-ex\]](#). [Erratum: *Phys.Rev.D* 97, 099903 (2018)].
- [71] **CMS** Collaboration, V. Khachatryan *et al.*, “Search for dark matter particles in proton-proton collisions at $\sqrt{s} = 8$ TeV using the razor variables,” *JHEP* **12** (2016) 088, [arXiv:1603.08914 \[hep-ex\]](#).
- [72] **ATLAS** Collaboration, M. Aaboud *et al.*, “Search for new phenomena in events with a photon and missing transverse momentum in pp collisions at $\sqrt{s} = 13$ TeV with the ATLAS detector,” *JHEP* **06** (2016) 059, [arXiv:1604.01306 \[hep-ex\]](#).
- [73] **ATLAS** Collaboration, M. Aaboud *et al.*, “Search for dark matter at $\sqrt{s} = 13$ TeV in final states containing an energetic photon and large missing transverse momentum with the ATLAS detector,” *Eur. Phys. J. C* **77** (2017) no. 6, 393, [arXiv:1704.03848 \[hep-ex\]](#).
- [74] J. Kalinowski, P. Kozów, S. Pokorski, J. Rosiek, M. Szleper, and S. Tkaczyk, “Same-sign WW scattering at the LHC: can we discover BSM effects before discovering new states?,” *Eur. Phys. J. C* **78** (2018) no. 5, 403, [arXiv:1802.02366 \[hep-ph\]](#).
- [75] P. Kozów, L. Merlo, S. Pokorski, and M. Szleper, “Same-sign WW Scattering in the HEFT: Discoverability vs. EFT Validity,” *JHEP* **07** (2019) 021, [arXiv:1905.03354 \[hep-ph\]](#).
- [76] G. Chaudhary, J. Kalinowski, M. Kaur, P. Kozów, K. Sandeep, M. Szleper, and S. Tkaczyk, “EFT triangles in the same-sign WW scattering process at the HL-LHC and HE-LHC,” *Eur. Phys. J. C* **80** (2020) no. 3, 181, [arXiv:1906.10769 \[hep-ph\]](#).
- [77] J. Lang, S. Liebler, H. Schäfer-Siebert, and D. Zeppenfeld, “Effective field theory versus UV-complete model: vector boson scattering as a case study,” *Eur. Phys. J. C* **81** (2021) no. 7, 659, [arXiv:2103.16517 \[hep-ph\]](#).

- [78] B. Andersson, G. Gustafson, G. Ingelman, and T. Sjöstrand, “Parton Fragmentation and String Dynamics,” *Phys. Rept.* **97** (1983) 31–145.
- [79] A. Hook, E. Izaguirre, M. Lisanti, and J. G. Wacker, “High Multiplicity Searches at the LHC Using Jet Masses,” *Phys. Rev.* **D85** (2012) 055029, [arXiv:1202.0558 \[hep-ph\]](#).
- [80] T. Cohen, E. Izaguirre, M. Lisanti, and H. K. Lou, “Jet Substructure by Accident,” *JHEP* **03** (2013) 161, [arXiv:1212.1456 \[hep-ph\]](#).
- [81] P. Gras, S. Höche, D. Kar, A. Larkoski, L. Lönnblad, S. Plätzer, A. Siódmok, P. Skands, G. Soyez, and J. Thaler, “Systematics of quark/gluon tagging,” *JHEP* **07** (2017) 091, [arXiv:1704.03878 \[hep-ph\]](#).
- [82] H. P. Nilles and K. Streng, “Quark - Gluon Separation in Three Jet Events,” *Phys. Rev. D* **23** (1981) 1944.
- [83] L. M. Jones, “Tests for Determining the Parton Ancestor of a Hadron Jet,” *Phys. Rev. D* **39** (1989) 2550.
- [84] Z. Fodor, “How to See the Differences Between Quark and Gluon Jets,” *Phys. Rev. D* **41** (1990) 1726.
- [85] L. Jones, “TOWARDS A SYSTEMATIC JET CLASSIFICATION,” *Phys. Rev. D* **42** (1990) 811–814.
- [86] L. Lonnblad, C. Peterson, and T. Rognvaldsson, “Using neural networks to identify jets,” *Nucl. Phys. B* **349** (1991) 675–702.
- [87] J. Gallicchio and M. D. Schwartz, “Quark and Gluon Tagging at the LHC,” *Phys. Rev. Lett.* **107** (2011) 172001, [arXiv:1106.3076 \[hep-ph\]](#).
- [88] J. Gallicchio and M. D. Schwartz, “Quark and Gluon Jet Substructure,” *JHEP* **04** (2013) 090, [arXiv:1211.7038 \[hep-ph\]](#).
- [89] D. Krohn, M. D. Schwartz, T. Lin, and W. J. Waalewijn, “Jet Charge at the LHC,” *Phys. Rev. Lett.* **110** (2013) no. 21, 212001, [arXiv:1209.2421 \[hep-ph\]](#).
- [90] CMS Collaboration, S. Chatrchyan *et al.*, “Search for a Higgs boson in the decay channel H to $ZZ^{(*)}$ to $q \bar{q} \ell^{-} \ell^{+}$ in pp collisions at $\sqrt{s} = 7$ TeV,” *JHEP* **04** (2012) 036, [arXiv:1202.1416 \[hep-ex\]](#).
- [91] A. J. Larkoski, J. Thaler, and W. J. Waalewijn, “Gaining (Mutual) Information about Quark/Gluon Discrimination,” *JHEP* **11** (2014) 129, [arXiv:1408.3122 \[hep-ph\]](#).

- [92] B. Bhattacharjee, S. Mukhopadhyay, M. M. Nojiri, Y. Sakaki, and B. R. Webber, “Associated jet and subjet rates in light-quark and gluon jet discrimination,” *JHEP* **04** (2015) 131, [arXiv:1501.04794 \[hep-ph\]](#).
- [93] D. Ferreira de Lima, P. Petrov, D. Soper, and M. Spannowsky, “Quark-Gluon tagging with Shower Deconstruction: Unearthing dark matter and Higgs couplings,” *Phys. Rev. D* **95** (2017) no. 3, 034001, [arXiv:1607.06031 \[hep-ph\]](#).
- [94] B. Bhattacharjee, S. Mukhopadhyay, M. M. Nojiri, Y. Sakaki, and B. R. Webber, “Quark-gluon discrimination in the search for gluino pair production at the LHC,” *JHEP* **01** (2017) 044, [arXiv:1609.08781 \[hep-ph\]](#).
- [95] P. T. Komiske, E. M. Metodiev, and M. D. Schwartz, “Deep learning in color: towards automated quark/gluon jet discrimination,” *JHEP* **01** (2017) 110, [arXiv:1612.01551 \[hep-ph\]](#).
- [96] J. Davighi and P. Harris, “Fractal based observables to probe jet substructure of quarks and gluons,” *Eur. Phys. J. C* **78** (2018) no. 4, 334, [arXiv:1703.00914 \[hep-ph\]](#).
- [97] E. M. Metodiev and J. Thaler, “Jet Topics: Disentangling Quarks and Gluons at Colliders,” *Phys. Rev. Lett.* **120** (2018) no. 24, 241602, [arXiv:1802.00008 \[hep-ph\]](#).
- [98] **ATLAS** Collaboration, M. Aaboud *et al.*, “Measurement of jet-substructure observables in top quark, W boson and light jet production in proton-proton collisions at $\sqrt{s} = 13$ TeV with the ATLAS detector,” *JHEP* **08** (2019) 033, [arXiv:1903.02942 \[hep-ex\]](#).
- [99] **CMS** Collaboration, A. M. Sirunyan *et al.*, “Measurement of jet substructure observables in $t\bar{t}$ events from proton-proton collisions at $\sqrt{s} = 13$ TeV,” *Phys. Rev. D* **98** (2018) no. 9, 092014, [arXiv:1808.07340 \[hep-ex\]](#).
- [100] **ATLAS** Collaboration, “Discrimination of Light Quark and Gluon Jets in pp collisions at $\sqrt{s} = 8$ TeV with the ATLAS Detector,”.
- [101] C. F. Berger, T. Kucs, and G. F. Sterman, “Event shape / energy flow correlations,” *Phys. Rev.* **D68** (2003) 014012, [arXiv:hep-ph/0303051 \[hep-ph\]](#).
- [102] L. G. Almeida, S. J. Lee, G. Perez, G. F. Sterman, I. Sung, and J. Virzi, “Substructure of high- p_T Jets at the LHC,” *Phys. Rev.* **D79** (2009) 074017, [arXiv:0807.0234 \[hep-ph\]](#).
- [103] A. J. Larkoski, S. Marzani, G. Soyez, and J. Thaler, “Soft Drop,” *JHEP* **05** (2014) 146, [arXiv:1402.2657 \[hep-ph\]](#).

- [104] M. Dasgupta, L. Magnea, and G. P. Salam, “Non-perturbative QCD effects in jets at hadron colliders,” *JHEP* **02** (2008) 055, [arXiv:0712.3014 \[hep-ph\]](#).
- [105] M. Dasgupta, K. Khelifa-Kerfa, S. Marzani, and M. Spannowsky, “On jet mass distributions in Z+jet and dijet processes at the LHC,” *JHEP* **10** (2012) 126, [arXiv:1207.1640 \[hep-ph\]](#).
- [106] A. Banfi, G. P. Salam, and G. Zanderighi, “Principles of general final-state resummation and automated implementation,” *JHEP* **03** (2005) 073, [arXiv:hep-ph/0407286 \[hep-ph\]](#).
- [107] A. Banfi, G. P. Salam, and G. Zanderighi, “Resummed event shapes at hadron - hadron colliders,” *JHEP* **08** (2004) 062, [arXiv:hep-ph/0407287 \[hep-ph\]](#).
- [108] S. Catani, L. Trentadue, G. Turnock, and B. R. Webber, “Resummation of large logarithms in e^+e^- event shape distributions,” *Nucl. Phys.* **B407** (1993) 3–42.
- [109] **ATLAS** Collaboration, G. Aad *et al.*, “Light-quark and gluon jet discrimination in pp collisions at $\sqrt{s} = 7$ TeV with the ATLAS detector,” *Eur. Phys. J.* **C74** (2014) no. 8, 3023, [arXiv:1405.6583 \[hep-ex\]](#).
- [110] S. Marzani, L. Schunk, and G. Soyez, “A study of jet mass distributions with grooming,” *JHEP* **07** (2017) 132, [arXiv:1704.02210 \[hep-ph\]](#).
- [111] S. Catani, B. R. Webber, and G. Marchesini, “QCD coherent branching and semi-inclusive processes at large x ,” *Nucl. Phys.* **B349** (1991) 635–654.
- [112] **Particle Data Group** Collaboration, M. Tanabashi *et al.*, “Review of Particle Physics,” *Phys. Rev.* **D98** (2018) no. 3, 030001.
- [113] T. Sjöstrand, S. Ask, J. R. Christiansen, R. Corke, N. Desai, P. Ilten, S. Mrenna, S. Prestel, C. O. Rasmussen, and P. Z. Skands, “An Introduction to PYTHIA 8.2,” *Comput. Phys. Commun.* **191** (2015) 159–177, [arXiv:1410.3012 \[hep-ph\]](#).
- [114] M. Cacciari, G. P. Salam, and G. Soyez, “The anti- k_t jet clustering algorithm,” *JHEP* **04** (2008) 063, [arXiv:0802.1189 \[hep-ph\]](#).
- [115] M. Cacciari, G. P. Salam, and G. Soyez, “FastJet User Manual,” *Eur. Phys. J.* **C72** (2012) 1896, [arXiv:1111.6097 \[hep-ph\]](#).
- [116] L. G. Almeida, S. D. Ellis, C. Lee, G. Sterman, I. Sung, and J. R. Walsh, “Comparing and counting logs in direct and effective methods of QCD resummation,” *JHEP* **04** (2014) 174, [arXiv:1401.4460 \[hep-ph\]](#).
- [117] F. Tackmann, “Theory Uncertainties from Nuisance Parameters.” <https://indico.physics.lbl.gov/indico/event/694/contributions/3344/>. SCET 2019.

- [118] C. Frye, A. J. Larkoski, M. D. Schwartz, and K. Yan, “Factorization for groomed jet substructure beyond the next-to-leading logarithm,” *JHEP* **07** (2016) 064, [arXiv:1603.09338 \[hep-ph\]](#).
- [119] T. T. Jouttenus, I. W. Stewart, F. J. Tackmann, and W. J. Waalewijn, “Jet mass spectra in Higgs boson plus one jet at next-to-next-to-leading logarithmic order,” *Phys. Rev.* **D88** (2013) no. 5, 054031, [arXiv:1302.0846 \[hep-ph\]](#).
- [120] D. Bertolini, M. P. Solon, and J. R. Walsh, “Integrated and Differential Accuracy in Resummed Cross Sections,” *Phys. Rev.* **D95** (2017) no. 5, 054024, [arXiv:1701.07919 \[hep-ph\]](#).
- [121] J. Bellm *et al.*, “Herwig 7.0/Herwig++ 3.0 release note,” *Eur. Phys. J.* **C76** (2016) no. 4, 196, [arXiv:1512.01178 \[hep-ph\]](#).
- [122] **ATLAS** Collaboration, M. Aaboud *et al.*, “Search for new phenomena in dijet events using 37 fb⁻¹ of *pp* collision data collected at $\sqrt{s} = 13$ TeV with the ATLAS detector,” *Phys. Rev.* **D96** (2017) no. 5, 052004, [arXiv:1703.09127 \[hep-ex\]](#).
- [123] **CMS** Collaboration, A. M. Sirunyan *et al.*, “Search for new physics in dijet angular distributions using proton-proton collisions at $\sqrt{s} = 13$ TeV and constraints on dark matter and other models,” *Eur. Phys. J.* **C78** (2018) no. 9, 789, [arXiv:1803.08030 \[hep-ex\]](#).
- [124] L. Basso, A. Belyaev, S. Moretti, and C. H. Shepherd-Themistocleous, “Phenomenology of the minimal $B - L$ extension of the Standard model: Z' and neutrinos,” *Phys. Rev.* **D80** (2009) 055030, [arXiv:0812.4313 \[hep-ph\]](#).
- [125] F. F. Deppisch, W. Liu, and M. Mitra, “Long-lived Heavy Neutrinos from Higgs Decays,” *JHEP* **08** (2018) 181, [arXiv:1804.04075 \[hep-ph\]](#).
- [126] A. Alloul, N. D. Christensen, C. Degrande, C. Duhr, and B. Fuks, “FEYNRULES 2.0 - A complete toolbox for tree-level phenomenology,” *Comput. Phys. Commun.* **185** (2014) 2250–2300, [arXiv:1310.1921 \[hep-ph\]](#).
- [127] J. Alwall, R. Frederix, S. Frixione, V. Hirschi, F. Maltoni, O. Mattelaer, H. S. Shao, T. Stelzer, P. Torrielli, and M. Zaro, “The automated computation of tree-level and next-to-leading order differential cross sections, and their matching to parton shower simulations,” *JHEP* **07** (2014) 079, [arXiv:1405.0301 \[hep-ph\]](#).
- [128] J. Currie, A. Gehrmann-De Ridder, T. Gehrmann, E. W. N. Glover, A. Huss, and J. Pires, “Precise predictions for dijet production at the LHC,” *Phys. Rev. Lett.* **119** (2017) no. 15, 152001, [arXiv:1705.10271 \[hep-ph\]](#).
- [129] K. G. Wilson, “Renormalization group and critical phenomena. 1. Renormalization group and the Kadanoff scaling picture,” *Phys. Rev. B* **4** (1971) 3174–3183.

- [130] K. G. Wilson, “Renormalization group and critical phenomena. 2. Phase space cell analysis of critical behavior,” *Phys. Rev. B* **4** (1971) 3184–3205.
- [131] K. G. Wilson and J. B. Kogut, “The Renormalization group and the epsilon expansion,” *Phys. Rept.* **12** (1974) 75–199.
- [132] S. Weinberg, “Effective Gauge Theories,” *Phys. Lett. B* **91** (1980) 51–55.
- [133] J. Goodman, M. Ibe, A. Rajaraman, W. Shepherd, T. M. P. Tait, and H.-B. Yu, “Constraints on Dark Matter from Colliders,” *Phys. Rev. D* **82** (2010) 116010, [arXiv:1008.1783 \[hep-ph\]](#).
- [134] P. J. Fox, R. Harnik, J. Kopp, and Y. Tsai, “Missing Energy Signatures of Dark Matter at the LHC,” *Phys. Rev. D* **85** (2012) 056011, [arXiv:1109.4398 \[hep-ph\]](#).
- [135] P. J. Fox, R. Harnik, R. Primulando, and C.-T. Yu, “Taking a Razor to Dark Matter Parameter Space at the LHC,” *Phys. Rev. D* **86** (2012) 015010, [arXiv:1203.1662 \[hep-ph\]](#).
- [136] U. Haisch, F. Kahlhoefer, and J. Unwin, “The impact of heavy-quark loops on LHC dark matter searches,” *JHEP* **07** (2013) 125, [arXiv:1208.4605 \[hep-ph\]](#).
- [137] P. J. Fox and C. Williams, “Next-to-Leading Order Predictions for Dark Matter Production at Hadron Colliders,” *Phys. Rev. D* **87** (2013) no. 5, 054030, [arXiv:1211.6390 \[hep-ph\]](#).
- [138] M. Papucci, A. Vichi, and K. M. Zurek, “Monojet versus the rest of the world I: t-channel models,” *JHEP* **11** (2014) 024, [arXiv:1402.2285 \[hep-ph\]](#).
- [139] M. Endo and Y. Yamamoto, “Unitarity Bounds on Dark Matter Effective Interactions at LHC,” *JHEP* **06** (2014) 126, [arXiv:1403.6610 \[hep-ph\]](#).
- [140] M. Garny, A. Ibarra, and S. Vogl, “Signatures of Majorana dark matter with t-channel mediators,” *Int. J. Mod. Phys. D* **24** (2015) no. 07, 1530019, [arXiv:1503.01500 \[hep-ph\]](#).
- [141] N. Bell, G. Busoni, A. Kobakhidze, D. M. Long, and M. A. Schmidt, “Unitarisation of EFT Amplitudes for Dark Matter Searches at the LHC,” *JHEP* **08** (2016) 125, [arXiv:1606.02722 \[hep-ph\]](#).
- [142] S. Bruggisser, F. Riva, and A. Urbano, “The Last Gasp of Dark Matter Effective Theory,” *JHEP* **11** (2016) 069, [arXiv:1607.02475 \[hep-ph\]](#).
- [143] A. Belyaev, L. Panizzi, A. Pukhov, and M. Thomas, “Dark Matter characterization at the LHC in the Effective Field Theory approach,” *JHEP* **04** (2017) 110, [arXiv:1610.07545 \[hep-ph\]](#).

- [144] F. Bishara, J. Brod, B. Grinstein, and J. Zupan, “Chiral Effective Theory of Dark Matter Direct Detection,” *JCAP* **02** (2017) 009, [arXiv:1611.00368 \[hep-ph\]](#).
- [145] S. Banerjee, D. Barducci, G. Bélanger, B. Fuks, A. Goudelis, and B. Zaldivar, “Cornering pseudoscalar-mediated dark matter with the LHC and cosmology,” *JHEP* **07** (2017) 080, [arXiv:1705.02327 \[hep-ph\]](#).
- [146] E. Bertuzzo, C. J. Caniu Barros, and G. Grilli di Cortona, “MeV Dark Matter: Model Independent Bounds,” *JHEP* **09** (2017) 116, [arXiv:1707.00725 \[hep-ph\]](#).
- [147] S. Belwal, M. Drees, and J. S. Kim, “Analysis of the Bounds on Dark Matter Models from Monojet Searches at the LHC,” *Phys. Rev. D* **98** (2018) no. 5, 055017, [arXiv:1709.08545 \[hep-ph\]](#).
- [148] A. Belyaev, E. Bertuzzo, C. Caniu Barros, O. Eboli, G. Grilli Di Cortona, F. Iocco, and A. Pukhov, “Interplay of the LHC and non-LHC Dark Matter searches in the Effective Field Theory approach,” *Phys. Rev. D* **99** (2019) no. 1, 015006, [arXiv:1807.03817 \[hep-ph\]](#).
- [149] F. Bishara, J. Brod, B. Grinstein, and J. Zupan, “Renormalization Group Effects in Dark Matter Interactions,” *JHEP* **03** (2020) 089, [arXiv:1809.03506 \[hep-ph\]](#).
- [150] S. Trojanowski, P. Brax, and C. van de Bruck, “Dark matter relic density from conformally or disformally coupled light scalars,” *Phys. Rev. D* **102** (2020) no. 2, 023035, [arXiv:2006.01149 \[hep-ph\]](#).
- [151] F. Fortuna, P. Roig, and J. Wudka, “Effective field theory analysis of dark matter-standard model interactions with spin one mediators,” *JHEP* **02** (2021) 223, [arXiv:2008.10609 \[hep-ph\]](#).
- [152] **GAMBIT** Collaboration, P. Athron *et al.*, “Thermal WIMPs and the Scale of New Physics: Global Fits of Dirac Dark Matter Effective Field Theories,” [arXiv:2106.02056 \[hep-ph\]](#).
- [153] J.-C. Yang, Y.-C. Guo, C.-X. Yue, and Q. Fu, “Constraints on anomalous quartic gauge couplings via $Z\gamma jj$ production at the LHC,” [arXiv:2107.01123 \[hep-ph\]](#).
- [154] B. Barman, S. Bhattacharya, S. Girmohanta, and S. Jahedi, “Catch ’em all: Effective Leptophilic WIMPs at the e^+e^- Collider,” [arXiv:2109.10936 \[hep-ph\]](#).
- [155] G. J. Gounaris, J. Layssac, J. E. Paschalis, and F. M. Renard, “Unitarity constraints for new physics induced by dim-6 operators,” *Z. Phys. C* **66** (1995) 619–632, [arXiv:hep-ph/9409260](#).

- [156] J. A. Aguilar-Saavedra, “Effective four-fermion operators in top physics: A Roadmap,” *Nucl. Phys. B* **843** (2011) 638–672, [arXiv:1008.3562 \[hep-ph\]](#).
[Erratum: Nucl.Phys.B 851, 443–444 (2011)].
- [157] R. Contino, C. Grojean, D. Pappadopulo, R. Rattazzi, and A. Thamm, “Strong Higgs Interactions at a Linear Collider,” *JHEP* **02** (2014) 006, [arXiv:1309.7038 \[hep-ph\]](#).
- [158] T. Corbett, O. J. P. Éboli, and M. C. Gonzalez-Garcia, “Unitarity Constraints on Dimension-Six Operators,” *Phys. Rev. D* **91** (2015) no. 3, 035014, [arXiv:1411.5026 \[hep-ph\]](#).
- [159] A. Pomarol, “Higgs Physics,” in *2014 European School of High-Energy Physics*. 12, 2014. [arXiv:1412.4410 \[hep-ph\]](#).
- [160] A. Azatov, R. Contino, G. Panico, and M. Son, “Effective field theory analysis of double Higgs boson production via gluon fusion,” *Phys. Rev. D* **92** (2015) no. 3, 035001, [arXiv:1502.00539 \[hep-ph\]](#).
- [161] A. Falkowski, “Effective field theory approach to LHC Higgs data,” *Pramana* **87** (2016) no. 3, 39, [arXiv:1505.00046 \[hep-ph\]](#).
- [162] J. Brehmer, A. Freitas, D. Lopez-Val, and T. Plehn, “Pushing Higgs Effective Theory to its Limits,” *Phys. Rev. D* **93** (2016) no. 7, 075014, [arXiv:1510.03443 \[hep-ph\]](#).
- [163] **LHC Higgs Cross Section Working Group** Collaboration, D. de Florian *et al.*, “Handbook of LHC Higgs Cross Sections: 4. Deciphering the Nature of the Higgs Sector,” [arXiv:1610.07922 \[hep-ph\]](#).
- [164] L. Di Luzio, J. F. Kamenik, and M. Nardecchia, “Implications of perturbative unitarity for scalar di-boson resonance searches at LHC,” *Eur. Phys. J. C* **77** (2017) no. 1, 30, [arXiv:1604.05746 \[hep-ph\]](#).
- [165] R. Contino, A. Falkowski, F. Goertz, C. Grojean, and F. Riva, “On the Validity of the Effective Field Theory Approach to SM Precision Tests,” *JHEP* **07** (2016) 144, [arXiv:1604.06444 \[hep-ph\]](#).
- [166] A. Falkowski, M. Gonzalez-Alonso, A. Greljo, D. Marzocca, and M. Son, “Anomalous Triple Gauge Couplings in the Effective Field Theory Approach at the LHC,” *JHEP* **02** (2017) 115, [arXiv:1609.06312 \[hep-ph\]](#).
- [167] D. A. Faroughy, A. Greljo, and J. F. Kamenik, “Confronting lepton flavor universality violation in B decays with high- p_T tau lepton searches at LHC,” *Phys. Lett. B* **764** (2017) 126–134, [arXiv:1609.07138 \[hep-ph\]](#).

- [168] M. Farina, G. Panico, D. Pappadopulo, J. T. Ruderman, R. Torre, and A. Wulzer, “Energy helps accuracy: electroweak precision tests at hadron colliders,” *Phys. Lett. B* **772** (2017) 210–215, [arXiv:1609.08157 \[hep-ph\]](#).
- [169] ATLAS Collaboration, M. Aaboud *et al.*, “Search for new phenomena in dijet events using 37 fb⁻¹ of *pp* collision data collected at $\sqrt{s}=13$ TeV with the ATLAS detector,” *Phys. Rev. D* **96** (2017) no. 5, 052004, [arXiv:1703.09127 \[hep-ex\]](#).
- [170] A. Greljo and D. Marzocca, “High- p_T dilepton tails and flavor physics,” *Eur. Phys. J. C* **77** (2017) no. 8, 548, [arXiv:1704.09015 \[hep-ph\]](#).
- [171] T. Corbett, O. J. P. Éboli, and M. C. Gonzalez-Garcia, “Unitarity Constraints on Dimension-six Operators II: Including Fermionic Operators,” *Phys. Rev. D* **96** (2017) no. 3, 035006, [arXiv:1705.09294 \[hep-ph\]](#).
- [172] S. Alioli, M. Farina, D. Pappadopulo, and J. T. Ruderman, “Precision Probes of QCD at High Energies,” *JHEP* **07** (2017) 097, [arXiv:1706.03068 \[hep-ph\]](#).
- [173] A. Azatov, J. Elias-Miro, Y. Reyimuaji, and E. Venturini, “Novel measurements of anomalous triple gauge couplings for the LHC,” *JHEP* **10** (2017) 027, [arXiv:1707.08060 \[hep-ph\]](#).
- [174] G. Panico, F. Riva, and A. Wulzer, “Diboson interference resurrection,” *Phys. Lett. B* **776** (2018) 473–480, [arXiv:1708.07823 \[hep-ph\]](#).
- [175] R. Franceschini, G. Panico, A. Pomarol, F. Riva, and A. Wulzer, “Electroweak Precision Tests in High-Energy Diboson Processes,” *JHEP* **02** (2018) 111, [arXiv:1712.01310 \[hep-ph\]](#).
- [176] M. Jin and Y. Gao, “Z-pole test of effective dark matter diboson interactions at the CEPC,” *Eur. Phys. J. C* **78** (2018) no. 8, 622, [arXiv:1712.02140 \[hep-ph\]](#).
- [177] S. Alioli, M. Farina, D. Pappadopulo, and J. T. Ruderman, “Catching a New Force by the Tail,” *Phys. Rev. Lett.* **120** (2018) no. 10, 101801, [arXiv:1712.02347 \[hep-ph\]](#).
- [178] C. F. Anders *et al.*, “Vector boson scattering: Recent experimental and theory developments,” *Rev. Phys.* **3** (2018) 44–63, [arXiv:1801.04203 \[hep-ph\]](#).
- [179] D. Barducci *et al.*, “Interpreting top-quark LHC measurements in the standard-model effective field theory,” [arXiv:1802.07237 \[hep-ph\]](#).
- [180] J. Ellis, C. W. Murphy, V. Sanz, and T. You, “Updated Global SMEFT Fit to Higgs, Diboson and Electroweak Data,” *JHEP* **06** (2018) 146, [arXiv:1803.03252 \[hep-ph\]](#).

- [181] **CMS** Collaboration, A. M. Sirunyan *et al.*, “Search for new physics in dijet angular distributions using proton–proton collisions at $\sqrt{s} = 13$ TeV and constraints on dark matter and other models,” *Eur. Phys. J. C* **78** (2018) no. 9, 789, [arXiv:1803.08030 \[hep-ex\]](#).
- [182] S. Banerjee, C. Englert, R. S. Gupta, and M. Spannowsky, “Probing Electroweak Precision Physics via boosted Higgs-strahlung at the LHC,” *Phys. Rev. D* **98** (2018) no. 9, 095012, [arXiv:1807.01796 \[hep-ph\]](#).
- [183] C. Hays, A. Martin, V. Sanz, and J. Setford, “On the impact of dimension-eight SMEFT operators on Higgs measurements,” *JHEP* **02** (2019) 123, [arXiv:1808.00442 \[hep-ph\]](#).
- [184] R. Gomez-Ambrosio, “Studies of Dimension-Six EFT effects in Vector Boson Scattering,” *Eur. Phys. J. C* **79** (2019) no. 5, 389, [arXiv:1809.04189 \[hep-ph\]](#).
- [185] M. Chala, J. Santiago, and M. Spannowsky, “Constraining four-fermion operators using rare top decays,” *JHEP* **04** (2019) 014, [arXiv:1809.09624 \[hep-ph\]](#).
- [186] C. Grojean, M. Montull, and M. Riemann, “Diboson at the LHC vs LEP,” *JHEP* **03** (2019) 020, [arXiv:1810.05149 \[hep-ph\]](#).
- [187] M. Farina, C. Mondino, D. Pappadopulo, and J. T. Ruderman, “New Physics from High Energy Tops,” *JHEP* **01** (2019) 231, [arXiv:1811.04084 \[hep-ph\]](#).
- [188] S. Dawson, P. P. Giardino, and A. Ismail, “Standard model EFT and the Drell-Yan process at high energy,” *Phys. Rev. D* **99** (2019) no. 3, 035044, [arXiv:1811.12260 \[hep-ph\]](#).
- [189] **CMS** Collaboration, A. M. Sirunyan *et al.*, “Measurements of the $pp \rightarrow WZ$ inclusive and differential production cross section and constraints on charged anomalous triple gauge couplings at $\sqrt{s} = 13$ TeV,” *JHEP* **04** (2019) 122, [arXiv:1901.03428 \[hep-ex\]](#).
- [190] A. Azatov, D. Barducci, and E. Venturini, “Precision diboson measurements at hadron colliders,” *JHEP* **04** (2019) 075, [arXiv:1901.04821 \[hep-ph\]](#).
- [191] M. Cepeda *et al.*, “Report from Working Group 2: Higgs Physics at the HL-LHC and HE-LHC,” *CERN Yellow Rep. Monogr.* **7** (2019) 221–584, [arXiv:1902.00134 \[hep-ph\]](#).
- [192] S. Chang and M. A. Luty, “The Higgs Trilinear Coupling and the Scale of New Physics,” *JHEP* **03** (2020) 140, [arXiv:1902.05556 \[hep-ph\]](#).
- [193] J. de Blas *et al.*, “Higgs Boson Studies at Future Particle Colliders,” *JHEP* **01** (2020) 139, [arXiv:1905.03764 \[hep-ph\]](#).

- [194] J. Baglio, S. Dawson, and S. Homiller, “QCD corrections in Standard Model EFT fits to WZ and WW production,” *Phys. Rev. D* **100** (2019) no. 11, 113010, [arXiv:1909.11576 \[hep-ph\]](#).
- [195] R. Torre, L. Ricci, and A. Wulzer, “On the W&Y interpretation of high-energy Drell-Yan measurements,” *JHEP* **02** (2021) 144, [arXiv:2008.12978 \[hep-ph\]](#).
- [196] CMS Collaboration, A. M. Sirunyan *et al.*, “Measurements of $pp \rightarrow ZZ$ production cross sections and constraints on anomalous triple gauge couplings at $\sqrt{s} = 13$ TeV,” *Eur. Phys. J. C* **81** (2021) no. 3, 200, [arXiv:2009.01186 \[hep-ex\]](#).
- [197] F. Abu-Ajamieh, S. Chang, M. Chen, and M. A. Luty, “Higgs coupling measurements and the scale of new physics,” *JHEP* **21** (2020) 056, [arXiv:2009.11293 \[hep-ph\]](#).
- [198] CMS Collaboration, A. M. Sirunyan *et al.*, “Search for new physics in top quark production with additional leptons in proton-proton collisions at $\sqrt{s} = 13$ TeV using effective field theory,” *JHEP* **03** (2021) 095, [arXiv:2012.04120 \[hep-ex\]](#).
- [199] J. J. Ethier, R. Gomez-Ambrosio, G. Magni, and J. Rojo, “SMEFT analysis of vector boson scattering and diboson data from the LHC Run II,” *Eur. Phys. J. C* **81** (2021) no. 6, 560, [arXiv:2101.03180 \[hep-ph\]](#).
- [200] CMS Collaboration, A. M. Sirunyan *et al.*, “Measurement of the $W\gamma$ Production Cross Section in Proton-Proton Collisions at $\sqrt{s}=13$ TeV and Constraints on Effective Field Theory Coefficients,” *Phys. Rev. Lett.* **126** (2021) no. 25, 252002, [arXiv:2102.02283 \[hep-ex\]](#).
- [201] ATLAS Collaboration, G. Aad *et al.*, “Measurements of $W^+W^- + \geq 1$ jet production cross-sections in pp collisions at $\sqrt{s} = 13$ TeV with the ATLAS detector,” *JHEP* **06** (2021) 003, [arXiv:2103.10319 \[hep-ex\]](#).
- [202] G. Panico, L. Ricci, and A. Wulzer, “High-energy EFT probes with fully differential Drell-Yan measurements,” *JHEP* **07** (2021) 086, [arXiv:2103.10532 \[hep-ph\]](#).
- [203] J.-C. Yang, J.-H. Chen, and Y.-C. Guo, “Extract the energy scale of anomalous $\gamma\gamma \rightarrow W^+W^-$ scattering in the vector boson scattering process using artificial neural networks,” [arXiv:2107.13624 \[hep-ph\]](#).
- [204] CMS Collaboration, A. Tumasyan *et al.*, “Probing effective field theory operators in the associated production of top quarks with a Z boson in multilepton final states at $\sqrt{s} = 13$ TeV,” [arXiv:2107.13896 \[hep-ex\]](#).
- [205] R. Bellan *et al.*, “A sensitivity study of VBS and diboson WW to dimension-6 EFT operators at the LHC,” [arXiv:2108.03199 \[hep-ph\]](#).

- [206] I. M. Shoemaker and L. Vecchi, “Unitarity and Monojet Bounds on Models for DAMA, CoGeNT, and CRESST-II,” *Phys. Rev. D* **86** (2012) 015023, [arXiv:1112.5457 \[hep-ph\]](#).
- [207] G. Busoni, A. De Simone, E. Morgante, and A. Riotto, “On the Validity of the Effective Field Theory for Dark Matter Searches at the LHC,” *Phys. Lett. B* **728** (2014) 412–421, [arXiv:1307.2253 \[hep-ph\]](#).
- [208] O. Buchmuller, M. J. Dolan, and C. McCabe, “Beyond Effective Field Theory for Dark Matter Searches at the LHC,” *JHEP* **01** (2014) 025, [arXiv:1308.6799 \[hep-ph\]](#).
- [209] G. Busoni, A. De Simone, J. Gramling, E. Morgante, and A. Riotto, “On the Validity of the Effective Field Theory for Dark Matter Searches at the LHC, Part II: Complete Analysis for the s -channel,” *JCAP* **06** (2014) 060, [arXiv:1402.1275 \[hep-ph\]](#).
- [210] G. Busoni, A. De Simone, T. Jacques, E. Morgante, and A. Riotto, “On the Validity of the Effective Field Theory for Dark Matter Searches at the LHC Part III: Analysis for the t -channel,” *JCAP* **09** (2014) 022, [arXiv:1405.3101 \[hep-ph\]](#).
- [211] A. Biekötter, A. Knochel, M. Krämer, D. Liu, and F. Riva, “Vices and virtues of Higgs effective field theories at large energy,” *Phys. Rev. D* **91** (2015) 055029, [arXiv:1406.7320 \[hep-ph\]](#).
- [212] C. Englert and M. Spannowsky, “Effective Theories and Measurements at Colliders,” *Phys. Lett. B* **740** (2015) 8–15, [arXiv:1408.5147 \[hep-ph\]](#).
- [213] D. Racco, A. Wulzer, and F. Zwirner, “Robust collider limits on heavy-mediator Dark Matter,” *JHEP* **05** (2015) 009, [arXiv:1502.04701 \[hep-ph\]](#).
- [214] M. Gorbahn, J. M. No, and V. Sanz, “Benchmarks for Higgs Effective Theory: Extended Higgs Sectors,” *JHEP* **10** (2015) 036, [arXiv:1502.07352 \[hep-ph\]](#).
- [215] M. Bauer, A. Butter, N. Desai, J. Gonzalez-Fraile, and T. Plehn, “Validity of dark matter effective theory,” *Phys. Rev. D* **95** (2017) no. 7, 075036, [arXiv:1611.09908 \[hep-ph\]](#).
- [216] F. Pobbe, A. Wulzer, and M. Zanetti, “Setting limits on Effective Field Theories: the case of Dark Matter,” *JHEP* **08** (2017) 074, [arXiv:1704.00736 \[hep-ph\]](#).
- [217] C. Garcia-Garcia, M. Herrero, and R. A. Morales, “Unitarization effects in EFT predictions of WZ scattering at the LHC,” *Phys. Rev. D* **100** (2019) no. 9, 096003, [arXiv:1907.06668 \[hep-ph\]](#).

- [218] E. E. Boos, V. E. Bunichev, L. V. Dudko, M. A. Perfilov, and G. A. Vorotnikov, “Eligibility of EFT Approach to Search for tqg FCNC Phenomenon,” *Phys. Atom. Nucl.* **83** (2020) no. 6, 984–988, [arXiv:2004.14498 \[hep-ph\]](#).
- [219] O. Buchmueller, M. J. Dolan, S. A. Malik, and C. McCabe, “Characterising dark matter searches at colliders and direct detection experiments: Vector mediators,” *JHEP* **01** (2015) 037, [arXiv:1407.8257 \[hep-ph\]](#).
- [220] J. Abdallah *et al.*, “Simplified Models for Dark Matter and Missing Energy Searches at the LHC,” [arXiv:1409.2893 \[hep-ph\]](#).
- [221] S. A. Malik *et al.*, “Interplay and Characterization of Dark Matter Searches at Colliders and in Direct Detection Experiments,” *Phys. Dark Univ.* **9-10** (2015) 51–58, [arXiv:1409.4075 \[hep-ex\]](#).
- [222] P. Harris, V. V. Khoze, M. Spannowsky, and C. Williams, “Constraining Dark Sectors at Colliders: Beyond the Effective Theory Approach,” *Phys. Rev. D* **91** (2015) 055009, [arXiv:1411.0535 \[hep-ph\]](#).
- [223] R. Primulando, E. Salvioni, and Y. Tsai, “The Dark Penguin Shines Light at Colliders,” *JHEP* **07** (2015) 031, [arXiv:1503.04204 \[hep-ph\]](#).
- [224] M. Chala, F. Kahlhoefer, M. McCullough, G. Nardini, and K. Schmidt-Hoberg, “Constraining Dark Sectors with Monojets and Dijets,” *JHEP* **07** (2015) 089, [arXiv:1503.05916 \[hep-ph\]](#).
- [225] A. Gupta, R. Primulando, and P. Saraswat, “A New Probe of Dark Sector Dynamics at the LHC,” *JHEP* **09** (2015) 079, [arXiv:1504.01385 \[hep-ph\]](#).
- [226] A. Arbey, M. Battaglia, and F. Mahmoudi, “Monojet Searches for MSSM Simplified Models,” *Phys. Rev. D* **94** (2016) no. 5, 055015, [arXiv:1506.02148 \[hep-ph\]](#).
- [227] J. Abdallah *et al.*, “Simplified Models for Dark Matter Searches at the LHC,” *Phys. Dark Univ.* **9-10** (2015) 8–23, [arXiv:1506.03116 \[hep-ph\]](#).
- [228] A. Alves, A. Berlin, S. Profumo, and F. S. Queiroz, “Dirac-fermionic dark matter in $U(1)_X$ models,” *JHEP* **10** (2015) 076, [arXiv:1506.06767 \[hep-ph\]](#).
- [229] J. Kumar, D. Marfatia, and D. Yaylali, “Vector dark matter at the LHC,” *Phys. Rev. D* **92** (2015) no. 9, 095027, [arXiv:1508.04466 \[hep-ph\]](#).
- [230] A. Choudhury, K. Kowalska, L. Roszkowski, E. M. Sessolo, and A. J. Williams, “Less-simplified models of dark matter for direct detection and the LHC,” *JHEP* **04** (2016) 182, [arXiv:1509.05771 \[hep-ph\]](#).

- [231] F. Kahlhoefer, K. Schmidt-Hoberg, T. Schwetz, and S. Vogl, “Implications of unitarity and gauge invariance for simplified dark matter models,” *JHEP* **02** (2016) 016, [arXiv:1510.02110 \[hep-ph\]](#).
- [232] M. J. Baker *et al.*, “The Coannihilation Codex,” *JHEP* **12** (2015) 120, [arXiv:1510.03434 \[hep-ph\]](#).
- [233] A. De Simone and T. Jacques, “Simplified models vs. effective field theory approaches in dark matter searches,” *Eur. Phys. J. C* **76** (2016) no. 7, 367, [arXiv:1603.08002 \[hep-ph\]](#).
- [234] A. Boveia *et al.*, “Recommendations on presenting LHC searches for missing transverse energy signals using simplified s -channel models of dark matter,” *Phys. Dark Univ.* **27** (2020) 100365, [arXiv:1603.04156 \[hep-ex\]](#).
- [235] S. Matsumoto, S. Mukhopadhyay, and Y.-L. S. Tsai, “Effective Theory of WIMP Dark Matter supplemented by Simplified Models: Singlet-like Majorana fermion case,” *Phys. Rev. D* **94** (2016) no. 6, 065034, [arXiv:1604.02230 \[hep-ph\]](#).
- [236] **ATLAS** Collaboration, M. Aaboud *et al.*, “Search for new phenomena in final states with an energetic jet and large missing transverse momentum in pp collisions at $\sqrt{s} = 13$ TeV using the ATLAS detector,” *Phys. Rev. D* **94** (2016) no. 3, 032005, [arXiv:1604.07773 \[hep-ex\]](#).
- [237] C. Englert, M. McCullough, and M. Spannowsky, “S-Channel Dark Matter Simplified Models and Unitarity,” *Phys. Dark Univ.* **14** (2016) 48–56, [arXiv:1604.07975 \[hep-ph\]](#).
- [238] T. Jacques, A. Katz, E. Morgante, D. Racco, M. Rameez, and A. Riotto, “Complementarity of DM searches in a consistent simplified model: the case of Z ?,” *JHEP* **10** (2016) 071, [arXiv:1605.06513 \[hep-ph\]](#). [Erratum: *JHEP* 01, 127 (2019)].
- [239] S. Bruggisser, F. Riva, and A. Urbano, “Strongly Interacting Light Dark Matter,” *SciPost Phys.* **3** (2017) no. 3, 017, [arXiv:1607.02474 \[hep-ph\]](#).
- [240] **CMS** Collaboration, V. Khachatryan *et al.*, “Search for dark matter in proton-proton collisions at 8 TeV with missing transverse momentum and vector boson tagged jets,” *JHEP* **12** (2016) 083, [arXiv:1607.05764 \[hep-ex\]](#). [Erratum: *JHEP* 08, 035 (2017)].
- [241] S. P. Liew, M. Papucci, A. Vichi, and K. M. Zurek, “Mono-X Versus Direct Searches: Simplified Models for Dark Matter at the LHC,” *JHEP* **06** (2017) 082, [arXiv:1612.00219 \[hep-ph\]](#).

- [242] **ATLAS** Collaboration, M. Aaboud *et al.*, “Search for dark matter and other new phenomena in events with an energetic jet and large missing transverse momentum using the ATLAS detector,” *JHEP* **01** (2018) 126, [arXiv:1711.03301 \[hep-ex\]](#).
- [243] **CMS** Collaboration, A. M. Sirunyan *et al.*, “Search for new physics in final states with an energetic jet or a hadronically decaying W or Z boson and transverse momentum imbalance at $\sqrt{s} = 13$ TeV,” *Phys. Rev. D* **97** (2018) no. 9, 092005, [arXiv:1712.02345 \[hep-ex\]](#).
- [244] E. Morgante, “Simplified Dark Matter Models,” *Adv. High Energy Phys.* **2018** (2018) 5012043, [arXiv:1804.01245 \[hep-ph\]](#).
- [245] N. Bernal, C. S. Fong, and A. Tonero, “Sharing but not Caring: Collider Phenomenology,” *JHEP* **08** (2018) 037, [arXiv:1806.00482 \[hep-ph\]](#).
- [246] **LHC Dark Matter Working Group** Collaboration, T. Abe *et al.*, “LHC Dark Matter Working Group: Next-generation spin-0 dark matter models,” *Phys. Dark Univ.* **27** (2020) 100351, [arXiv:1810.09420 \[hep-ex\]](#).
- [247] **ATLAS** Collaboration, M. Aaboud *et al.*, “Constraints on mediator-based dark matter and scalar dark energy models using $\sqrt{s} = 13$ TeV pp collision data collected by the ATLAS detector,” *JHEP* **05** (2019) 142, [arXiv:1903.01400 \[hep-ex\]](#).
- [248] M. Ruhdorfer, E. Salvioni, and A. Weiler, “A Global View of the Off-Shell Higgs Portal,” *SciPost Phys.* **8** (2020) 027, [arXiv:1910.04170 \[hep-ph\]](#).
- [249] L. Darmé, S. A. R. Ellis, and T. You, “Light Dark Sectors through the Fermion Portal,” *JHEP* **07** (2020) 053, [arXiv:2001.01490 \[hep-ph\]](#).
- [250] E. Bertuzzo and M. Taoso, “Probing light dark scalars with future experiments,” *JHEP* **03** (2021) 272, [arXiv:2011.04735 \[hep-ph\]](#).
- [251] M. Becker, D. Döring, S. Karmakar, and H. Päs, “Fermionic Singlet Dark Matter in One-Loop Solutions to the R_K Anomaly: A Systematic Study,” [arXiv:2103.12043 \[hep-ph\]](#).
- [252] L. Darmé, B. Fuks, and F. Maltoni, “Top-philic heavy resonances in four-top final states and their EFT interpretation,” [arXiv:2104.09512 \[hep-ph\]](#).
- [253] D. Abercrombie *et al.*, “Dark Matter benchmark models for early LHC Run-2 Searches: Report of the ATLAS/CMS Dark Matter Forum,” *Phys. Dark Univ.* **27** (2020) 100371, [arXiv:1507.00966 \[hep-ex\]](#).
- [254] **ATLAS** Collaboration, M. Aaboud *et al.*, “Measurement of $W^\pm W^\pm$ vector-boson scattering and limits on anomalous quartic gauge couplings with the ATLAS detector,” *Phys. Rev. D* **96** (2017) no. 1, 012007, [arXiv:1611.02428 \[hep-ex\]](#).

- [255] CMS Collaboration, A. M. Sirunyan *et al.*, “Measurements of production cross sections of WZ and same-sign WW boson pairs in association with two jets in proton-proton collisions at $\sqrt{s} = 13$ TeV,” *Phys. Lett. B* **809** (2020) 135710, [arXiv:2005.01173 \[hep-ex\]](#).
- [256] G. F. Giudice, C. Grojean, A. Pomarol, and R. Rattazzi, “The Strongly-Interacting Light Higgs,” *JHEP* **06** (2007) 045, [arXiv:hep-ph/0703164](#).
- [257] I. Banta, T. Cohen, N. Craig, X. Lu, and D. Sutherland, “Non-Decoupling New Particles,” [arXiv:2110.02967 \[hep-ph\]](#).
- [258] M. D. Schwartz, *Quantum Field Theory and the Standard Model*. Cambridge University Press, 3, 2014.
- [259] E. Eichten, I. Hinchliffe, K. D. Lane, and C. Quigg, “Super Collider Physics,” *Rev. Mod. Phys.* **56** (1984) 579–707. [Addendum: *Rev. Mod. Phys.* 58, 1065–1073 (1986)].
- [260] H.-L. Lai, M. Guzzi, J. Huston, Z. Li, P. M. Nadolsky, J. Pumplin, and C. P. Yuan, “New parton distributions for collider physics,” *Phys. Rev. D* **82** (2010) 074024, [arXiv:1007.2241 \[hep-ph\]](#).
- [261] M. Farina, Y. Nakai, and D. Shih, “Searching for New Physics with Deep Autoencoders,” [arXiv:1808.08992 \[hep-ph\]](#).
- [262] T. Heimel, G. Kasieczka, T. Plehn, and J. M. Thompson, “QCD or What?,” *SciPost Phys.* **6** (2019) no. 3, 030, [arXiv:1808.08979 \[hep-ph\]](#).
- [263] J. H. Collins, K. Howe, and B. Nachman, “Extending the search for new resonances with machine learning,” *Phys. Rev. D* **99** (2019) no. 1, 014038, [arXiv:1902.02634 \[hep-ph\]](#).
- [264] R. T. D’Agnolo, G. Grosso, M. Pierini, A. Wulzer, and M. Zanetti, “Learning Multivariate New Physics,” [arXiv:1912.12155 \[hep-ph\]](#).
- [265] L. Bradshaw, R. K. Mishra, A. Mitridate, and B. Ostdiek, “Mass Agnostic Jet Taggers,” *SciPost Phys.* **8** (2020) no. 1, 011, [arXiv:1908.08959 \[hep-ph\]](#).
- [266] B. Nachman and D. Shih, “Anomaly Detection with Density Estimation,” [arXiv:2001.04990 \[hep-ph\]](#).
- [267] A. Andreassen, B. Nachman, and D. Shih, “Simulation Assisted Likelihood-free Anomaly Detection,” [arXiv:2001.05001 \[hep-ph\]](#).
- [268] J. Hajer, Y.-Y. Li, T. Liu, and H. Wang, “Novelty Detection Meets Collider Physics,” *Phys. Rev. D* **101** (2020) no. 7, 076015, [arXiv:1807.10261 \[hep-ph\]](#).

- [269] A. Andreassen and B. Nachman, “Neural Networks for Full Phase-space Reweighting and Parameter Tuning,” [arXiv:1907.08209](#) [[hep-ph](#)].
- [270] M. Madigan and J. Moore, “Parton distributions in the SMEFT from high-energy Drell-Yan tails,” in *European Physical Society Conference on High Energy Physics 2021*. 10, 2021. [arXiv:2110.13204](#) [[hep-ph](#)].
- [271] R. Alonso, E. E. Jenkins, and A. V. Manohar, “A Geometric Formulation of Higgs Effective Field Theory: Measuring the Curvature of Scalar Field Space,” *Phys. Lett. B* **754** (2016) 335–342, [arXiv:1511.00724](#) [[hep-ph](#)].
- [272] R. Alonso, E. E. Jenkins, and A. V. Manohar, “Geometry of the Scalar Sector,” *JHEP* **08** (2016) 101, [arXiv:1605.03602](#) [[hep-ph](#)].
- [273] T. Cohen, N. Craig, X. Lu, and D. Sutherland, “Is SMEFT Enough?,” *JHEP* **03** (2021) 237, [arXiv:2008.08597](#) [[hep-ph](#)].
- [274] A. Falkowski and R. Rattazzi, “Which EFT,” *JHEP* **10** (2019) 255, [arXiv:1902.05936](#) [[hep-ph](#)].
- [275] T. Cohen, N. Craig, X. Lu, and D. Sutherland, “Unitarity Violation and the Geometry of Higgs EFTs,” [arXiv:2108.03240](#) [[hep-ph](#)].
- [276] B. Henning, X. Lu, T. Melia, and H. Murayama, “Operator bases, S -matrices, and their partition functions,” *JHEP* **10** (2017) 199, [arXiv:1706.08520](#) [[hep-th](#)].
- [277] A. Helset, A. Martin, and M. Trott, “The Geometric Standard Model Effective Field Theory,” *JHEP* **03** (2020) 163, [arXiv:2001.01453](#) [[hep-ph](#)].
- [278] H. Elvang, “Bootstrap and amplitudes: a hike in the landscape of quantum field theory,” *Rept. Prog. Phys.* **84** (2021) no. 7, 074201, [arXiv:2007.08436](#) [[hep-th](#)].
- [279] Y. L. Dokshitzer, A. Lucenti, G. Marchesini, and G. P. Salam, “On the QCD analysis of jet broadening,” *JHEP* **01** (1998) 011, [arXiv:hep-ph/9801324](#) [[hep-ph](#)].
- [280] G. Luisoni and S. Marzani, “QCD resummation for hadronic final states,” *J. Phys.* **G42** (2015) no. 10, 103101, [arXiv:1505.04084](#) [[hep-ph](#)].